# Nuclear magnetic resonance and rheo-NMR investigations of wormlike micelles, rheology modifiers, and ion-conducting polymers

Kyle Gregory Wilmsmeyer

Dissertation submitted to the faculty of the Chemistry Department and College of Science at Virginia Polytechnic Institute and State University in partial fulfillment of the requirements for the degree of

Doctor of Philosophy
in
Chemistry

Louis A. Madsen (chair)
Harry C. Dorn
Timothy E. Long
Hervé Marand

6 August 2012
Blacksburg, VA

Keywords: nuclear magnetic resonance, NMR, rheology, viscoelasticity, rheo-NMR, wormlike micelle, surfactant, Nafion, self-diffusion

# Nuclear Magnetic Resonance and Rheo-NMR Investigations of Wormlike Micelles, Rheology Modifiers, and Ion-Conducting Polymers

Kyle Gregory Wilmsmeyer

## Abstract

Investigation and characterization of polymeric materials are necessary to obtain in-depth understanding of their behavior and properties, which can fuel further development. To illuminate these molecular properties and their coupling to macroscopic behavior, we have performed nuclear magnetic resonance (NMR) studies on a variety of chemical systems. In addition to versatile "traditional" NMR measurements, we took advantage of specialized techniques, such as "rheo-NMR," $^{2}$H NMR, and NMR self-diffusion experiments to analyze alignment, orientational order, elaborate rheological behavior, and ion transport in polymer films and complex fluids.

We employed self-diffusion and quadrupolar deuterium NMR methods to water-swollen channels in Nafion ionomer films commonly used in fuel cells and actuators. We also correlated water uptake and anisotropic diffusion with differing degrees and types of alignment in Nafion films based on membrane processing methods. Further, we made quantitative measurements of bulk channel alignment in Nafion membranes and determined anisotropic properties such as the biaxiality parameter using these methods. Additionally, our studies made the first direct comparison of directional transport (diffusion) with quantitative orientational order measurements for ionomer membranes. These results lend insight to the importance of water

content in ionomer device performance, and showed that increased control over the direction and extent of orientational order of the hydrophilic channels could lead to improved materials design.

We used the same techniques, with the addition of "rheo-NMR" and solution rheology measurements, to study the complex rheological behavior of cetyltrimethylammonium bromide wormlike micelle solutions, which behave as nematic liquid crystals at sufficiently high concentration. Amphiphilic solutions of this type are used in myriad applications, from fracturing fluids in oil fields to personal care products. We investigated the phase behavior and dynamics of shear and magnetic field alignment, and made the first observations of a novel bistable shear-activated phase in these solutions. Our first reports of the complex Leslie-Ericksen viscoelastic parameters in wormlike micelles and measurements of diffusion anisotropy show the potential for increased control and understanding of materials used in tissue engineering, oil extraction, personal care products, and advanced lubricants.

## Acknowledgements

First and foremost, I wish to thank my advisor, Dr. Lou Madsen, for his constant support and understanding, and for teaching and challenging me throughout the past six years. His willingness to accept a student who knew very little about NMR as his first graduate student and development of the very productive research group he has built and maintained are a permanent inspiration to me, both personally and professionally, as I move onward in my life and career.

Thanks are also due to my committee members, Dr. Harry Dorn, Dr. Tim Long, Dr. Herve Marand, and Dr. Sungsool Wi, for their continued guidance, support, and constructive feedback throughout my graduate school education. I especially wish to thank Dr. Francis Webster, Dr. Cindy Burkhardt, and Dr. Joseph Wirgau of the Radford University Department of Chemistry for their support and inspiration during my undergraduate years, and for allowing me the opportunity to teach a course there while I was in graduate school - they are one of the primary reasons why I aim to teach at a primarily undergraduate institution someday.

Additional thanks go to Dr. Jing Li, Dr. Xiaolin Zhang, Dr. Richao Zhang, Dr. Mark Lingwood, and Dr. Francis Tuluri, for mentoring me and the other students in the group during their time with us. To my fellow group members, Jianbo Hou, Zhiyang Zhang, Kacey McCreary, Jim Wahmhoff, Bryce Kidd, Cocoa Huang, Ying Wang, and Rachele Piemonte, thanks for the camaraderie, discussion, and entertainment during our time together in the lab. Fellow graduate students Dr. Josh Layfield, Dr. Will Alexander, Dr. Samantha Higgins, Dr. Steve June, Tim Fuhrer, and Ken Knott, thanks for the guidance and the laughs for the past six years!

I also thank my friends and family back home for their constant support, encouragement, and interest in listening when I discuss my research. Special thanks go to my mother, Gwen Dickerson, without whose example, love, and encouragement I would probably never have done this, and would not be the person I am today. I love you and miss you, mom.

Finally, I thank my wife, Amanda, for her constant love and support as we have traveled through all the ups and downs of graduate school together and as we look forward to whatever is next.

KGW, August 2012; Blacksburg, VA

# Table of Contents

# List of Figures

# List of Tables

# Attribution

Several colleagues, lab mates, and my advisor have aided me in the development of the research performed and presented in this dissertation, as well as the preparation of published manuscripts which appear as portions of this work.

My research advisor, Dr. Louis A. Madsen, has provided guidance and support for all work presented in this document, and has also provided editorial oversight for published manuscripts and all chapters of this document.

Specifically, the ionomer research collected and presented in Chapters 2 and 3 was begun by me and continued work on the experiments was performed by Dr. Jing Li. Most of the manuscripts were written by Dr. Li and Dr. Madsen, with input on figures, data, and text from this author.

The rheo-NMR experiments on wormlike micelles work presented in Chapters 4 and 5 were performed by me, with assistance from Dr. Richao Zhang. Dr. Xiaolin Zhang provided assistance with the fitting program discussed in those chapters, but the fits were calculated by me using data collected by me. Both manuscripts were prepared by me, with oversight from Dr. Madsen.

# Chapter 1

# Introduction and Review of Literature

## 1.1 Thesis Statement

The goal of the research presented in this document was to investigate the effects of orientational order and complex dynamics on the behavior and transport of ionomer membranes, cylindrical micelles, and rheology modifiers, using specialized NMR techniques to elucidate morphology, molecular interactions, and subtle molecular scale behavior in these materials.

## 1.2 Motivation

Detailed investigation and characterization of novel polymeric materials and complex fluids are necessary to fully understand their behavior and properties, and to use that knowledge to enable further applications and guide future synthetic strategies. Macroscopic properties such as tensile strength and viscosity are inherently important, but studies of nanoscale properties such as orientational order are ever-increasing and becoming more powerful in aiding materials design.

Orientational order is an important characteristic found in myriad systems, though the influence of molecular scale behavior on macroscopic properties is less commonly studied. Rheology, a primary method for investigating the deformation and flow of samples under stress, is especially useful in polymer science and engineering, as it provides measurements and descriptions of properties such as modulus and viscosity, and can aid in finding potential uses for polymers. Use of nuclear magnetic resonance (NMR) spectroscopy to correlate molecular-scale behaviors with macroscopic properties from rheological measurements, known as "rheo-NMR," enables a better understanding of complex structure at the molecular level. Traditional methods of examining rheological parameters focus on the measurement of properties at the macroscopic

level. While macroscopic information is important, correlations with molecular scale properties promise to provide critical details for the enhancement and development of polymer systems and applications.

We have sought to apply rheo-NMR and other specialized NMR techniques to investigate orientational order effects in ionic polymer membranes and wormlike micelles. The remainder of this chapter will present a review of the relevant literature and extended introduction to rheo-NMR and orientational order, as well as the various materials and experiments used.

### 1.3 Nuclear Magnetic Resonance

The theory of spin and magnetism of nuclei was first proposed in 1927 by Austrian physicist Wolfgang Pauli, and magnetic resonance was first measured in molecular beams by Isidor Rabi in 1938,[1] for which he was awarded the 1944 Nobel Prize in physics. NMR was experimentally observed in condensed phases by Felix Bloch and Edward Purcell in 1946, for which they shared the 1952 Nobel Prize in physics.[2,3] Since that time, NMR has evolved into an immense field, encompassing both spectroscopy and medical imaging, and leading to additional Nobel prizes for NMR scientists, including Richard Ernst in 1991, Kurt Wüthrich in 2002, and Paul Lauterbur and Peter Mansfield in 2003.

NMR has several advantages over other analytical methods; namely, it is non-destructive, highly sensitive (some instruments can accurately analyze nanogram samples in microliter volumes), versatile enough to examine many different nuclei and interactions, and provides detailed structural information of the sample.[3] In addition, NMR boasts the ability to obtain dynamic and multi-dimensional sample information, has well-developed theory understood via the spin Hamiltonian, does not require samples to be optically transparent, and can be effectively

used to probe liquid, solid, and even gaseous samples. There has been significant use of NMR in the characterization of chemical samples, biomolecules,[4] and polymer films and solutions.[5]

### 1.3.1 NMR Review

All nuclei possess an inherent quantum property known as spin, measured by the spin quantum number $I$, and arising from the numbers of protons and neutrons present in the nucleus. The $^{1}H$ nucleus, for example, consists solely of one spin = ½ proton, and thus has total nuclear spin $I$ = ½. Continuing with this example, the $^{2}H$ nucleus, having one proton and one neutron, each with spin = ½, has total nuclear spin $I$ = 1. This is the ground nuclear shell state for the quadrupolar $^{2}H$ nucleus, and is a result of the lower-energy parallel spin alignment of the proton and neutron. Quadrupolar nuclei (spins $I$ > ½) exhibit unique behaviors in the NMR experiment, which we exploit and discuss in further detail below. Taking one more step, to the $^{3}H$ nucleus, which consists of one proton and two neutrons, we again find $I$ = ½. This is due to the Pauli Exclusion Principle, which requires that the spins of the two neutrons be aligned anti-parallel to one another, summing to 0, and leaving only the dipolar proton spin $I$ = ½ contributing to the total nuclear spin. $I$ is used in the determination of spin active nuclei, and nuclei have $2I + 1$ different azimuthal nuclear spin states,[6] $m_s$, which range from $-I$ to $+I$ in integer steps (note that this $m_s$ should not be confused with the electron $m_s$). In this manner, $I$ can be calculated for every isotope of every element, and thus the periodic table of NMR active nuclei is well known.

The spin quantum number is related to the nuclear magnetic moment ($\mu$) by:

$$\mu = \gamma I = \gamma m_s \hbar \tag{1.1}$$

where $\gamma$ is the gyromagnetic ratio and $\hbar$ is the reduced Planck constant. This spin magnetic moment allows for the observation of NMR (fig. 1.1), providing information about the local magnetic field observed by nuclei, based on the magnetic spin of the active nuclei and the

arrangement and alignment of molecules. NMR signal is provided by the absorption and emission of radio frequency (RF) energy when the nucleus of an atom is excited from its lowest energy spin state to the next higher one (or in the case of nuclei with spin greater than ½, between any two adjacent energy states).[3] The energy difference between the two states in an $I = ½$ system is directly proportional to the strength of the applied magnetic field, $\mathbf{B_0}$. When a sample is placed in a strong magnetic field (provided by the NMR superconducting magnet), the spin states of NMR active nuclei "split" and exhibit different energies, as shown in fig. 1.2. This potential energy difference of a continuous angular distribution of magnetic moments under the influence of an external magnetic field is known as the Zeeman energy and is given by:[6]

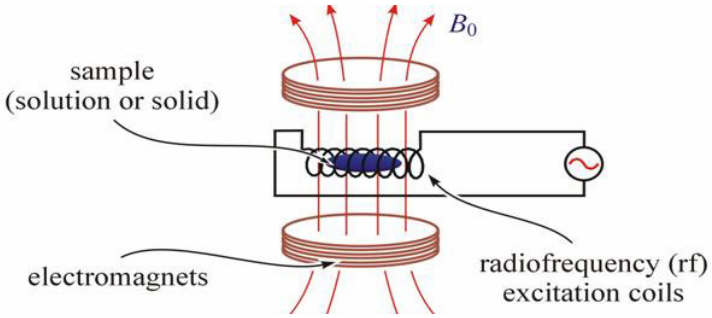


**Figure 1.1. Illustration of essential NMR instrumentation.**

$$\Delta E = \gamma \hbar B_0 \tag{1.2}$$

When no external magnetic field is present, these states all have identical energy (degeneracy).[3]

The energy difference created allows the sample to absorb RF radiation, which is periodically pulsed into the system via a coil surrounding the sample. The RF pulse rotates the magnetic moment of the nuclei from their precession about $\mathbf{B_0}$ into the x-y plane, and they subsequently relax and precess around the axis of the magnetic field, emitting an RF signal known as a free induction decay (FID) with

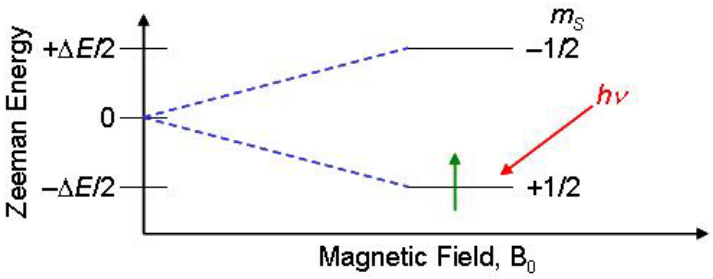


**Figure 1.2. Energy levels of NMR active nuclei** split when placed in a magnetic field, where $\Delta E = \hbar\omega_0$.

a frequency quantified by the difference in energy between the excited and ground states. This frequency is known as the Larmor frequency ($\omega_0$),

$$\omega_0 = -\gamma B_0 \tag{1.3}$$

and is detected by a radio receiver coil and transmitted to a computer for processing.[2,6] The transmitted data are then converted by Fourier transform into a frequency-domain signal, which is read and interpreted by the researcher.

### 1.3.2 Specialized NMR Techniques and Use in Polymer Chemistry

The first NMR experiment involving a polymer system was reported in 1947, and involved the study of the differences in the proton spectra of natural rubber both at room temperature and near the glass transition temperature.[5,7] With constant advancements in the field, it has now become possible to study polymers and other complex molecules using not only one dimensional, but also 2-D and 3-D NMR spectroscopy techniques.[8] Although solid-state instrumentation and experimentation is becoming more widely available and provides high information content, it does commonly suffer from the drawback of taking significantly longer to acquire data than solution NMR, as well as inconvenient sample loading and more complex experimental protocols. For this reason, solution NMR is typically used for polymers in order to determine stereochemistry, and to detect branches and defects.[5]

Additionally, information regarding the diffusion and motion of water molecules absorbed into a polymer membrane can be obtained via NMR.[9,10] NMR can also provide details on polymer morphology, leading, for example, to determination of the degree of orientational order or crystallinity present in that particular polymer sample.[11-13]

### 1.3.2.1 $^2$H NMR Spectroscopy

Deuterium is an $I = 1$ quadrupole nucleus, and thus exhibits an interaction between the electric quadrupole moment of the nucleus and the electric field gradient of the electron cloud due to the molecular bond in which it resides.[14,15] This interaction contributes to the Hamiltonian in the form:[16]

$$\mathcal{H}_Q = \frac{3e\nabla E Q_D}{4I(2I-1)} P_2(\cos\phi)(3I_z^2 - I^2) \tag{1.4}$$

where $\hbar E$ is the electric field gradient, $Q_D$ is the quadrupole moment of the deuterium nucleus,[8] $e$ is the electron charge, and $P_2(\cos\ \phi) = (3\cos^2\phi - 1)/2$ is the second Legendre polynomial, with $\phi$ the angle of the X-D bond relative to the direction of $\mathbf{B_0}$, where X is C, O, N, or another atom bound to deuterium, as shown in fig. 1.3. This interaction is usually substantially smaller than the Zeeman interaction, and is thus observed as a perturbation of the spin energy levels, as shown in fig. 1.4. Isotropic tumbling, as in a simple liquid, causes deuterated molecules to experience all $\phi$ during the NMR timescale, averaging this quadrupolar Hamiltonian to zero[16] and resulting in a single peak in the spectrum. However, if a deuteron label (or dilute deuterated probe molecule) is present in an anisotropic sample, the motional averaging of the deuterated molecules tumbling within the anisotropic constraints will be

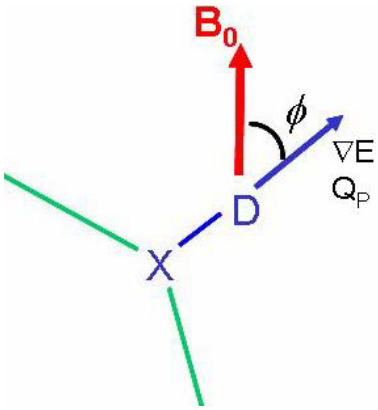


**Figure 1.3. Illustration of X-D bond orientation** with respect to $\mathbf{B_0}$ and resulting angle, $\phi$.

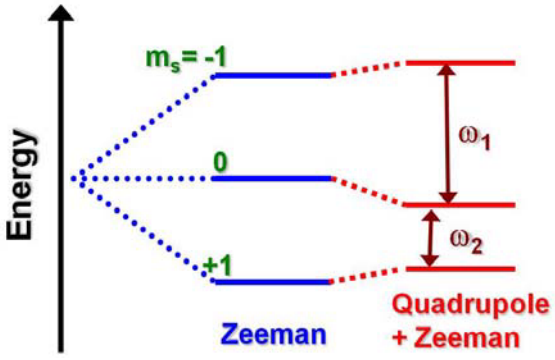


**Figure 1.4. Energy level diagram** depicting splittings due to Zeeman *and* quadrupole interactions in quadrupolar nuclei, such as $^2$H.

incomplete, causing the peak to split into a doublet.[14,15,17]

The observed splitting, $\Delta\nu_Q$, arising from the probe molecule is proportional to the orientational order parameter, *S*, and is given by the relationship:[18]

$$\Delta\nu_Q = Q_P S P_2(\cos\phi) \tag{1.5}$$

where $Q_P$ is the average quadrupole tensor component along the director axis. This splitting arises from the quadrupolar and Zeeman interactions, leading to inequivalent energy differences (see $\omega_1$ and $\omega_2$ in fig. 1.4). This inequivalence causes the deuterium peak to split into two, therefore a simpler way to express eqn. 1.5 would be:

$$\Delta\nu_Q = \omega_1 - \omega_2 \propto S \tag{1.6}$$

$^2$H NMR spectroscopy of labeled or doped molecules is a robust and well-established technique for probing orientational order in liquid crystals,[14,19,20] polymers,[8-10] cylindrical micelles,[21-25] and numerous other systems that exhibit molecular alignment.

#### 1.3.2.2 Pulsed-Field-Gradient Diffusion Experiments

Pulsed-field-gradient (PFG) NMR, first developed by Stejskal and Tanner[26] in 1965, has become a widely-used technique for studying the self-diffusion of molecules, and forms the structure on which magnetic resonance imaging (MRI) is built. We use this method in chapters 3 and 5 to measure translational motion of water molecules in ionic polymers and wormlike micelles, respectively.

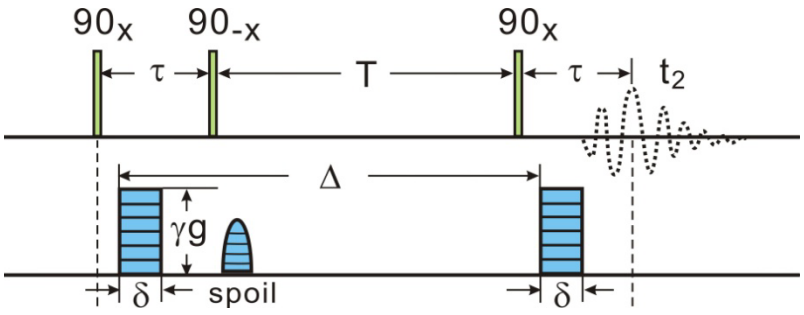


**Figure 1.5. PGSTE NMR pulse sequence.**

The pulsed-gradient stimulated-echo (PGSTE) NMR experiment (fig. 1.5) depends on signal attenuation caused by application of a pulsed-magnetic-field gradient immediately after application of a 90º RF pulse. This magnetic field gradient is a local variation of magnetic field strength across the sample, perturbing the Larmor frequencies of individual molecules slightly, effectively "encoding" their position in the sample. The molecules are then allowed to self-diffuse (Brownian motion) over a time Δ, before being refocused with additional RF pulses and "decoded" via application of a second gradient pulse. Signal attenuation caused by diffusion in this experiment is described by:[26]

$$A = A_0 e^{-D\gamma^2 g^2 \delta^2 (\Delta - \delta/3)} \tag{1.7}$$

where $A$ is the spin-echo signal intensity, $A_0$ is the signal intensity with zero gradient strength ($g$), $\delta$ is the duration of the gradient pulse, and $D$ is the self-diffusion coefficient of the nucleus under investigation. $D$ is obtained by varying $g$ and fitting the resulting varied signal amplitudes of the stimulated echo decays to eqn. 1.7. $A_0$ and $\gamma$ are constant for a given system and nucleus, respectively, and we experimentally set values for $g$, $\delta$, and Δ; so $D$ is easily calculated.

## 1.4 Rheology, Viscoelasticity, and Nematodynamics

Rheology, a branch of continuum mechanics, is the study of the deformation and flow of a substance under the influence of stress.[27] The term rheology originated in the 1920s, and since then the science has developed into a large field composed of chemists, physicists, materials scientists, engineers, and mathematicians, who investigate a broad scope of properties and materials.[27-29] The stress vs strain rate curve of a Newtonian material is linear and passes through the origin, and the material has one viscosity and one elastic constant. Viscosity of a Newtonian material under shear is given by the following relationship:

$$\eta = \frac{\tau}{\left(d\gamma_s/dt\right)} \tag{1.8}$$

where $\eta$ is the shear viscosity, $\tau$ is the shear stress, and $\gamma_s$ is the shear strain. A non-Newtonian fluid, by contrast, has a bulk viscosity which is dependent on shear rate or shear history, and is composed of five independent viscosity parameters and three elastic constants. The non-Newtonian wormlike micelle solutions we study in chapters 4 and 5 exhibit nematic liquid crystalline behavior, so we turn to the wealth of literature describing viscoelasticity theory for liquid crystals.

Nematodynamics, the continuum dynamics theory for liquid crystal mesophases, was developed nearly eighty years ago by Oseen,[30] Zocher,[31] Frank,[32] Ericksen,[33,34] Leslie,[35] and Maier and Saupe,[36] upon the realization that the coupling between orientation and flow of nematic materials exhibits complex, non-Newtonian viscoelastic behavior. In the nematic phase, molecules orient about a director **ñ**, and this director can be controlled by interaction of the nematic with external forces such as electric, magnetic, or flow fields.[37] The Frank elastic constants $K_1$, $K_2$, and $K_3$ are associated with bulk deformation and gradients in the director field, and refer to the splay, twist, and bend distortions, respectively, of a nematic liquid crystal (see fig. 1.6). Experimentally, $K_3$ is typically the largest, $K_2$ is usually small, and all three must be positive for the nematic conformation to maintain minimum free energy.[38] A

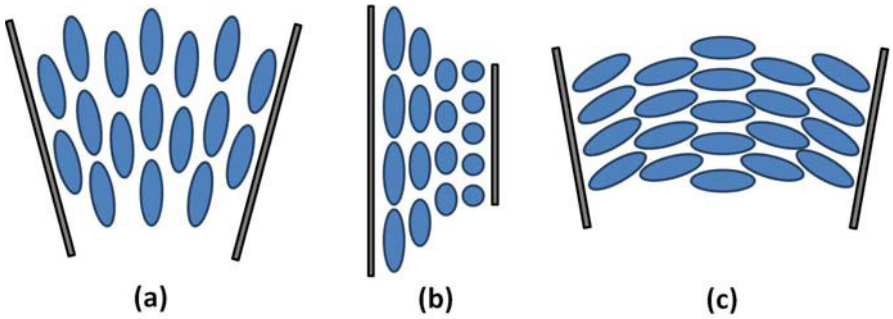


**Figure 1.6. Illustration of (a) splay, (b) twist, and (c) bend distortions** of a nematic liquid crystal sample. The elastic constants associated with these deformations are the Frank constants $K_1$, $K_2$, and $K_3$, respectively.

linear, incompressible isotropic fluid has a single viscosity, obtainable directly from solution rheology experiments, but incompressible anisotropic fluids under shear have five independent viscosities ($\alpha_i$), commonly known as the Leslie viscosities.[35,37]

Three of the Leslie viscosities ($\alpha_2$, $\alpha_3$, $\alpha_4$) determine the direction and rate of free rotation of **ñ** in a shear field. $\alpha_2$, corresponding to the torque on a rod aligned with the velocity gradient, is experimentally always negative. $\alpha_3$, the torque on a rod oriented with the flow field, can be either positive or negative; if it is positive, a free rod can tumble through the shear field without reaching steady-state orientation.[37] If $\alpha_2\alpha_3 > 0$, the director aligns along the flow direction, while if $\alpha_2\alpha_3 < 0$, the director rotates freely, and tumbling occurs.[39,40] $\alpha_4$ is a rotational coefficient, which can indicate viscous drag.

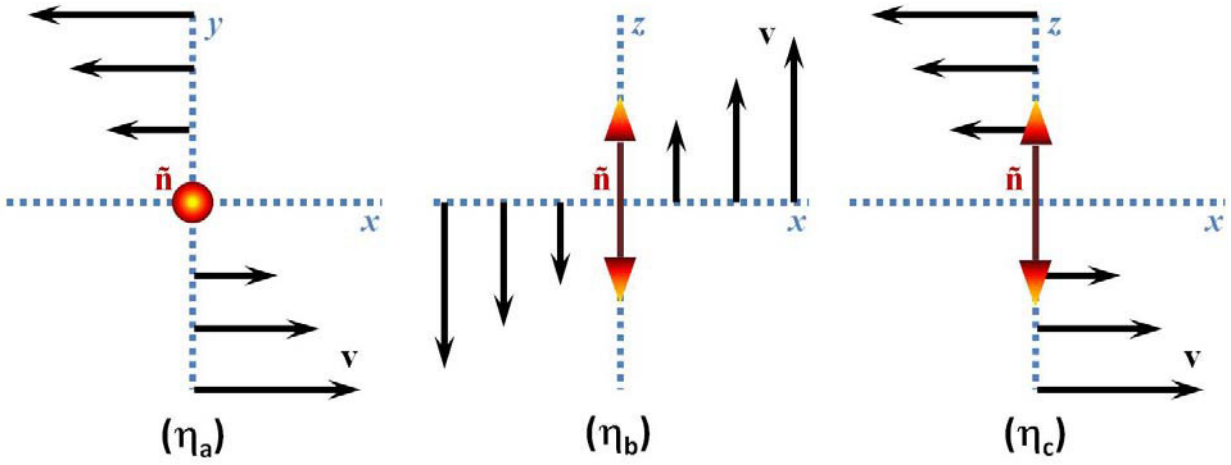


**Figure 1.7. Illustration of measurement of the Miesowicz viscosities under shear flow.**

Parodi subsequently derived the relationships between the $\alpha_i$'s[41] based on an Onsager relation:[37,38,42]

$$\alpha_6 = \alpha_2 + \alpha_3 + \alpha_5 \tag{1.9}$$

$$\xi_1 = \alpha_3 - \alpha_2 \tag{1.10}$$

$$\xi_2 = \alpha_2 + \alpha_3 = \alpha_6 - \alpha_5 \tag{1.11}$$

Thus, the effective bulk viscosity measured for an incompressible nematic is always some combination of the $\alpha_i$'s. Because the viscous properties of the nematic are dependent on the director orientation, the three Miesowicz shear viscosities[43,44] ($\eta_a$, $\eta_b$, $\eta_c$) can be measured by holding the director fixed in three orthogonal directions relative to the shear direction, as illustrated in fig. 1.7. This is frequently done in the presence of an external magnetic field (fig. 1.8), which fixes the director. The relationships between the Leslie viscosities and the Miesowicz viscosities under simple shear in a magnetic field have also been determined:[38]

$$\eta_a = \frac{1}{2}\alpha_4 \tag{1.12}$$

$$\eta_b = \frac{1}{2}(\alpha_3 + \alpha_4 + \alpha_6) \tag{1.13}$$

$$\eta_c = \frac{1}{2}(-\alpha_2 + \alpha_4 + \alpha_5) \tag{1.14}$$

Our experiments in chapters 4 and 5 provide the first measurements of these complex viscoelastic parameters in a wormlike micelle system.[23]

Traditional solution rheology measurements such as bulk viscosity, modulus, stress, and strain, and the relationships between them are commonly acquired parameters in materials and polymer science. However, the data obtained are average values inherently geared toward the examination of materials on a macroscopic scale.[27] A stress vs strain measurement, for instance, may provide important information for the manufacturer of plastic bags, but what does that measurement actually mean

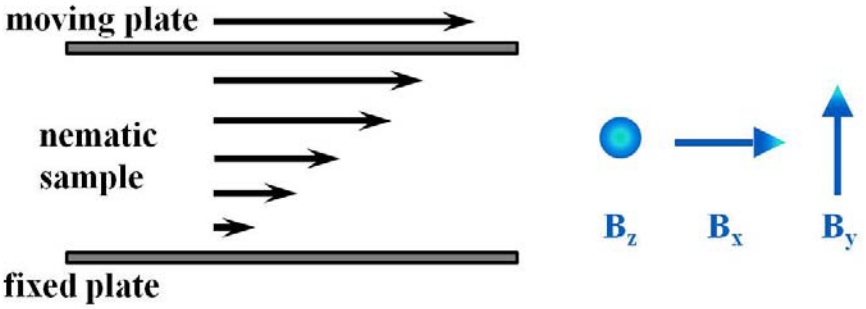


**Figure 1.8. The Miesowicz experiment.**

at the *molecular* level? It may be useful for the manufacturer of the polymer to understand how the material behaves on a molecular level as stress is applied, so that they may design a polymer better suited to resist the resulting strain. Our work bridges the gap between macroscopic and molecular scale measurements of viscosity and order, utilizing a combination of NMR and rheology known as *rheo-NMR*.

### 1.5 Rheo-NMR

The coupling of rheological measurements with the *in situ*, non-destructive techniques of NMR spectroscopy is a relatively recent development, and to date, only a handful of groups[45] worldwide are utilizing this powerful technique.

#### 1.5.1 History and Development of Rheo-NMR

Rheology as a science faces two central difficulties: 1) to provide detailed flow field information, and 2) to enhance observations and theory to yield details of molecular arrangement and dynamics.[46] In recent years, developments in the field have led to the use of several "hyphenated" experimental techniques such as the combination of rheological shear with neutron scattering (*e.g.* rheo-SANS), birefringence and dichroism, and X-ray and optical diffraction in order to answer the question of molecular arrangement.[45,46] Rheo-NMR is a relatively recent and promising[45] analytical technique which has arisen in pursuit of detailed molecular understanding.

NMR spectroscopy is the most recent tool used for rheological purposes, having first been coupled with "quasi-" rheological measurements in 1986 by Martins *et al.*, which were performed by physically rotating a sample cell within the NMR coil and following the dynamics of director realignment with $\mathbf{B_0}$ in a liquid crystal polymer.[47,48] The first "true" rheo-NMR experiments utilizing variable and controlled shear of a polymer fluid were performed by Samulski *et al.* in 1990.[49] NMR spectroscopy is particularly well suited to the investigation of

materials at the atomic level,[3] providing a convenient bridge between microscopic and macroscopic behavior. Additionally, this technique is non-invasive, and has an advantage over optical measurements in that it does not require samples to be optically transparent.[3,45,46] Rheo-NMR spectroscopy and velocity imaging studies[46,50-52] greatly assist in alleviating the difficulties in understanding molecular behaviors faced by rheology, such as mapping the theoretically challenging shear banding dynamics associated with some polymer systems.[16,45] Finally, this technique is well suited for use in combination with traditional solution rheology measurements, allowing for spectroscopic observation of molecular order and organization, and can be correlated with existing linear and non-linear viscoelasticity theories, as discussed later in this chapter.

### 1.5.2 Use and Importance of Rheo-NMR

Because polymer processing depends on rheological properties (*e.g.* forces imparted due to extrusion), polymers in the melt state have received significant attention from rheo-NMR researchers,[45,52] and rheological measurements can also provide indication of molecular weight or microstructure.[29,53] Shear viscosity is an important property for processing, is dependent on shear rate, and must therefore be examined over a broad shear-rate range. Previously, examining this range of shear rates was labor intensive and time consuming, and thus costly for a manufacturer or researcher. However, Uludag and colleagues recently used rheo-NMR to show that observations of rheological properties using a cell designed for use with low-density polyethylene (LDPE) melts in a magnetic resonance imaging (MRI) instrument could lead to the development of an in-line viscosity sensor for polymer processing.[52]

The Uludag *et al.* study accurately reproduced polymer shear viscosity data compiled over nearly three decades of shear rate with just a single experiment.[52] The implications of this

study are enormous in terms of the amount of time that could be saved in characterization of future polymer systems. In addition, with the potential for development of an in-line sensor, processing companies could save time and money by diagnosing production problems earlier and more accurately. Kilfoil and Callaghan used rheo-NMR methods to determine the alignment tensor for poly(dimethylsiloxane) (PDMS) under shear.[51] Their work supports the capability of NMR to study the alignment of polymer chains, as it uses a benzene-$d_6$ probe molecule, and observes the deuterium signal response of the system. Further, their findings are consistent with predictions based on the Doi-Edwards model, and with other research pertaining to PDMS.[51] We have employed similar probe molecule strategies in our work to elucidate structure of polymers[9,10,54] and complex fluids.[23]

Atkin *et al.* have shown that shear can affect both the shape of the deuterium spectrum and the observed splitting, correlating to the order parameter.[55] Badiger *et al*. found that poly(acrylamide) solutions under shear exhibit changes in the observed proton spin-lattice relaxation times $T_1$ based on shear rate.[56] The group of Paul T. Callaghan at Victoria University of Wellington in New Zealand has performed rheo-NMR studies on many different systems, from polymer melts[50,57,58] to liquid crystals[59,60] to wormlike micelles.[24,25,61]

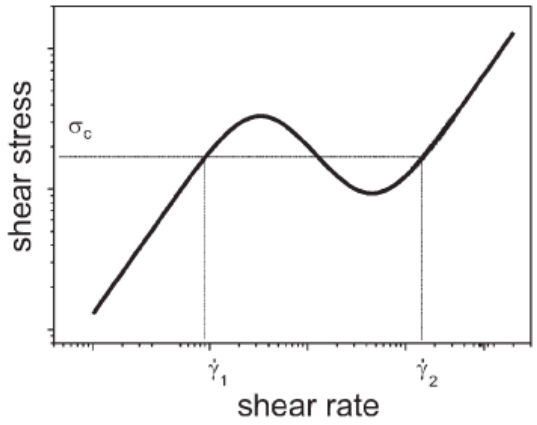


**Figure 1.9. Representation of the nonlinear shear rate/shear stress curve** of a wormlike micelle solution. At low shear rates, the system behaves in Newtonian fashion, while higher shear rates can cause shear thinning. Figure reprinted from reference 25.

Using rheo-NMR, Lopez-Gonzalez *et al.* describe the ability of cylindrical surfactant micelles (discussed in more detail later in this chapter) to act as a "living polymer," due to their ability to dissociate from one another and then reform.[25] Because of this, they exhibit a non-monotonic shear rate/stress curve, behaving as a Newtonian fluid at low shear rates and showing a stress plateau that can persist over several decades of shear rate. An increase in stress at higher shear rates is assumed, but challenging to measure.[25] An example of this common non-Newtonian behavior is shown in fig. 1.9. The stress plateau is associated with two phases in coexistence, often depicted as shear banding and discussed in further detail in the following paragraph. It is believed that the non-monotonic shear rate/shear stress behavior is due to dissociation and recombination, and governed by two time parameters: the breaking time, $\tau_{break}$, and the reptation time, $\tau_{rep}$.[27] The ability to quickly and accurately examine these parameters in a system could aid in the characterization process of the behavior of polymers, as current methodology has difficulty obtaining data at higher shear rates. Using the rheo-NMR method, a micelle system composed of 10% w/v cetylpyridinium chloride and sodium salicylate (CPyCl-NaSal) was examined.[25] The plateau modulus, zero shear viscosity, $\tau_{break}$, and $\tau_{rep}$ of the system were measured, and were found to closely match those measured by traditional means and previously reported by Berret *et al.*[62] We employ similar methods to study the complex viscoelastic behavior of wormlike micelles and urethane-based rheology modifier solutions, respectively.

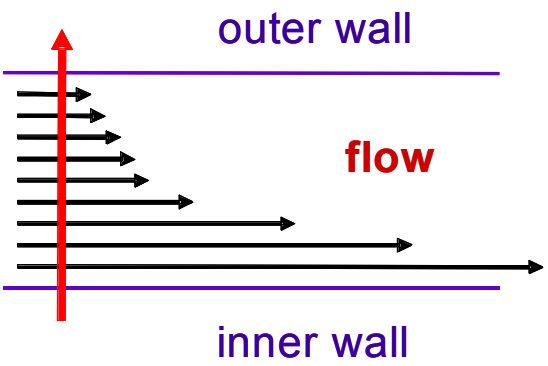


**Figure 1.10. Illustration of shear banding** observed in some samples in rheo-NMR. Sample nearest the inner wall (rotating) exhibits a different flow dependence (velocity gradient) with shear than sample nearest the outer wall (fixed).

Shearing performed in the Lopez-Gonzalez *et al.* study creates distinct shear bands[16,24] in the material, as the material nearest the inner, rotating cylinder moves with a different flow dependence on shear than material near the outer, fixed cylinder. A simple diagram depicting shear banding is shown in fig. 1.10. Rheo-NMR offers the particular advantage of being able to probe the sample at any time during the shear, as well as providing the tools to map and image the shear bands using NMR velocity imaging methods.[46] The results of this study showed that the system exhibits shear banding, and NMR microimaging obtained simultaneously was able to spatially map this banding as well as its dynamics.[25]

Hollingsworth and Johns have extended the scope of rheo-NMR, using the technique to study applications in food science, namely xanthan gum and commercial mayonnaise.[63] Their study used rheo-NMR to determine common rheological parameters of these emulsions, finding them in agreement with traditional rheology measurements. Callaghan and Gil have also applied rheo-NMR to food chemistry, observing spectral changes in gluten under shear using $^{1}H$ spectroscopy.[50]

### 1.5.3 Rheo-NMR Apparatus

Given the unique nature of the techniques involved in rheo-NMR and the relative youth of the field, there are a limited number of complete setups available for purchase. Naturally, each make and model of NMR instrument has different dimensions in terms of the bore diameter and length, spatial restrictions at the top of the instrument, and probe limitations. Therefore, it is necessary to construct a functional rheo-NMR apparatus for each instrument used throughout the course of these studies. Specifically, this requires the development of precisely machined systems for use on the Varian Unity 400 MHz, Bruker Avance III 400 MHz wide bore, and Bruker Avance III 600 MHz instruments on which our experiments are performed. Our primary

design for each instrument is compatible with several different sizes of sample cells, depending on probe and coil restrictions, and is based on designs inspired by those of Callaghan *et al.*[16,45,57]

The central component of the rheo-NMR apparatus is the Couette cell (fig. 1.11), which is used to apply shear stress, and replaces the sample tube present in standard NMR experiments. Couette geometry is used to investigate laminar flow of a fluid between parallel plates,[27] one of which is moving while the other is held fixed. In the context of viscous samples in the NMR instrument, we form a Couette cell using concentric cylinders (typically standard-sized NMR tubes cut to appropriate length with carefully made spacers between them) of varying diameter, which approximates infinite parallel plates while still confining the sample within the RF coil of the NMR instrument. Sample material is held in the gap created between the outer diameter of the inner cylinder and the inner diameter of the outer cylinder. The inner cylinder rotates with a constant angular velocity, applying a constant shear stress to the sample. Shear rate ($\dot{\gamma}$) in this cell is determined by:[24]

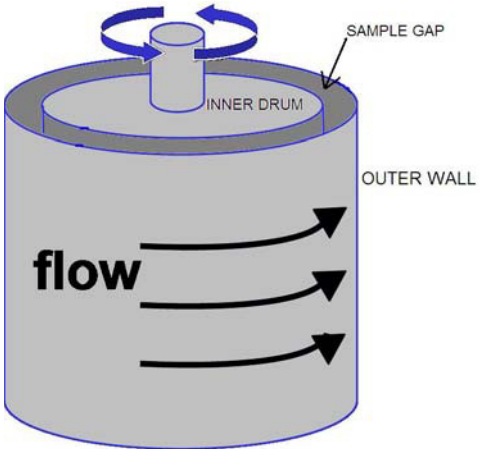


**Figure 1.11. Illustration of Couette sample cell used in rheo-NMR.** The outer wall is held fixed, while the inner drum rotates, shearing the sample held in the gap between the two cylinders.

$$\dot{\gamma} = \nu_1 \left[\frac{D_1\pi}{0.5(D_2 - D_1)}\right] \tag{1.15}$$

where $\nu_1$ is the rotation frequency of the inner cylinder, $D_1$ is the outer diameter of the inner cylinder, and $D_2$ is the inner diameter of the outer cylinder. $D_2$ - $D_1$ is simply the gap width of the cell, thus the term [$D_1\pi$/0.5($D_2$ - $D_1$)] is a constant for a given sample cell. The term $\nu_1$ is varied by utilizing a computer interface which controls the rest of the rheo-NMR apparatus

(detailed below). Douglass *et al*. showed that the practical shear rate is limited to ~ 200 $s^{-1}$ for some sample arrangements, due to sample cell vibration which causes signal disturbances at high $\nu_1$.[24] However, we have had success at shear rates over 500 $s^{-1}$ with smaller sample gap cells.

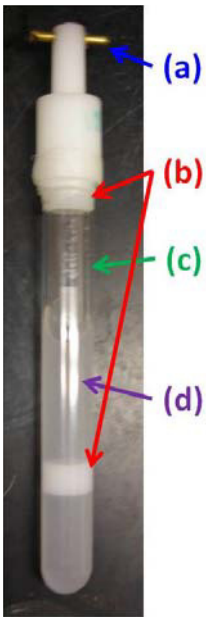


**Figure 1.12. Photo of Couette cell,** showing (a) brass crossbar, (b) Teflon spacers, (c) concentric glass NMR tubes, and (d) sample residing in sample gap.

The outer cylinder of the Couette cell (fig. 1.12) is held fixed to the NMR probe via a rubber washer or Teflon disc. These parts are machined to a diameter slightly smaller than the top of the NMR probe to ensure that the cell fits tightly and does not slip. Similarly, a hole slightly smaller than the outer diameter of the Couette cell is machined through the part in order to prevent translational or rotational motion of the outer cylinder of the cell. The inner cylinder of the Couette cell is topped with a brass crossbar which joins up with a four-fluted aluminum "claw" (fig. 1.13) designed to accept the crossbar without applying any downward force on the fragile glass Couette cells. The "claw" is attached to a brass driveshaft surrounded by a plastic guard, which runs through the bore of the NMR instrument. The driveshaft is secured with Teflon bushings inside, and the plastic guard has three recesses which hold rubber o-rings, preventing wobbling motion (and spectral anomalies due to mechanical vibration) inside

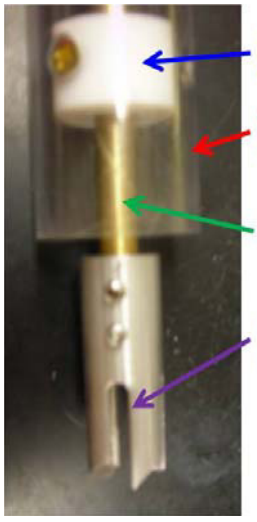


**Figure 1.13. Photo of "claw" and driveshaft,** showing (a) Teflon bushing, (b) plastic guard, (c) brass driveshaft, and (d) fluted aluminum "claw."

the bore during operation. An aluminum eyelet (fig. 1.14) is affixed to the top of the driveshaft, and is connected to an aluminum yoke (fig. 1.15). This yoke is joined to a small stepper motor which rests on a custom PVC mount (fig. 1.16) at the top of the NMR instrument. The stepper motor is in turn wired to a controller and computer software, which precisely controls revolution speed and thus, the resulting shear rate on the sample. We have designed and built complete, working rheo-NMR setups for all three spectrometers previously mentioned in this section.

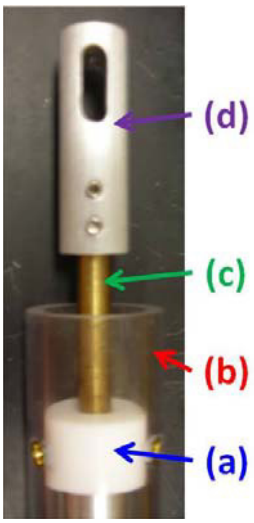


**Figure 1.14. Photo of eyelet and driveshaft,** showing (a) Teflon bushing, (b) plastic guard, (c) brass driveshaft, and (d) aluminum eyelet.

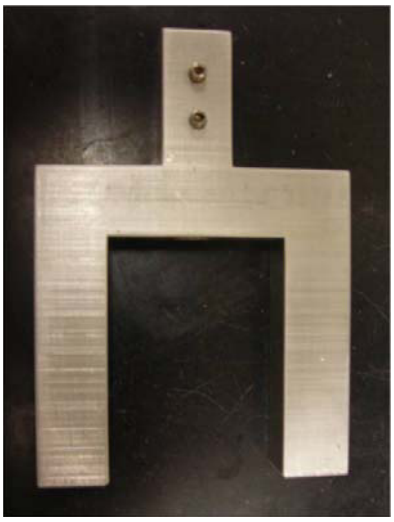

**Figure 1.15 (left). Photo of aluminum yoke** designed to couple the eyelet at the top of the brass driveshaft to the stepper motor drive.

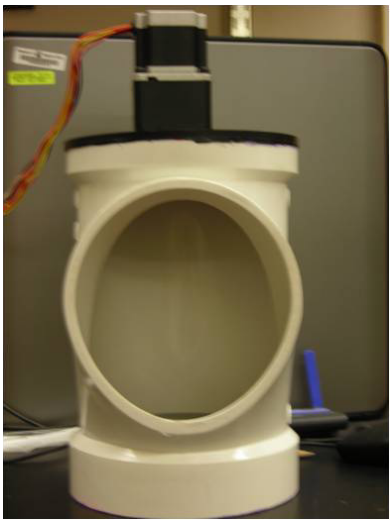

**Figure 1.16 (right). Photo of PVC motor mount** with stepper motor attached at top.

## 1.6 Orientational Order

Orientational order is synonymous with molecular alignment, and can be either short-range or long-range (macroscopic). It is present and probably most tangible in molecular solids. It is easy to accept this feature when imagining the crystalline structure of naphthalene or some other solid, but perhaps less so when envisioning liquid systems. However, orientational order is a critical feature in the synthesis, characterization, behavior, study, and use of liquid crystalline

materials and phases,[64] as well as in wormlike micelle solutions,[65] and is present throughout the cells and tissues of all living organisms. The presence of orientational order and development of methods for imparting and measuring it in polymer-based systems is a central theme of our research, and will be covered throughout this dissertation.

### 1.6.1 Orientational Order in Polymeric Materials

An important characteristic of polymer membranes used in fuel cell development is the amount of orientational order present in the ion-conducting channels of the polymer.[9,10,54,66] This order in ionic polymers, potentially crucial for improving the efficiency of fuel cells, can be probed in either the solid or solution state using various NMR techniques. Our work in chapters 2 and 3 of this dissertation details $^2$H and PFG methods for examining the order present in Nafion films. Orientational order can also be present in solutions of amphiphilic surfactant molecules, such as those that form wormlike micelles.[23] While molecules and supramolecular structures in these solutions freely move and can often be on average isotropic, application of shear via rheo-NMR can produce average molecular alignment in the solution.

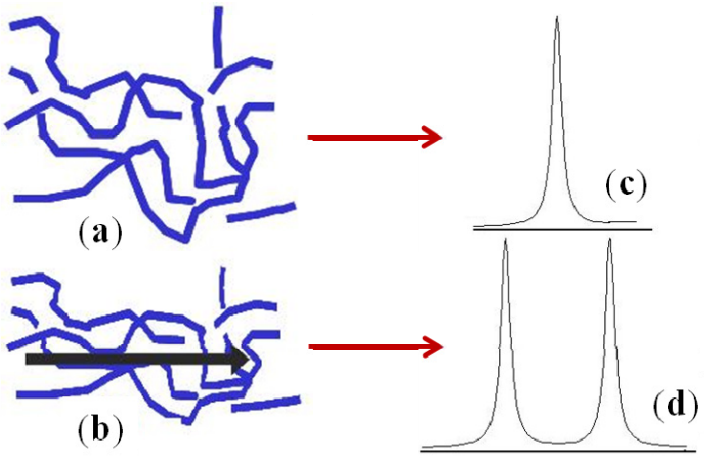


**Figure 1.17.** Illustration of isotropic material (**a**), anisotropic material (**b**) aligned in a flow field (black arrow), $^2$H NMR singlet spectrum (**c**), and $^2$H NMR doublet due to quadrupole splitting (**d**).

Figure 1.17 shows an illustration of a micellar network doped with $D_2O$ probe molecules in the isotropic and anisotropic states, and the result in their $^2$H spectra as discussed previously in this chapter. Anisotropic polymer or micelle

systems may exhibit different properties than their isotropic counterparts, potentially useful features for rheology modification[67] or NMR structure determination applications.[68] That is, an isotropic polymer sample will frequently have different optical, swelling, and diffusion properties than one with some bulk anisotropy. To study orientational order, the sample can be examined using rheo-NMR, facilitating the study of induced strain in the sample and observation of the molecular-scale effects of that strain *in situ*.

### 1.6.2 Orientational Order Observations

Quantification of the amount of order present in a liquid or liquid crystalline sample is necessarily measured as an average value over an entire sample, and is achieved by defining both a director **ñ** and a measure of the degree of order present (the orientational order parameter *S*, also commonly referred to as the Hermann's orientation function). *S* can be defined by the following relationship:[64]

$$S = \frac{\sum_j^N \left(\frac{3}{2}\cos^2\theta_j - \frac{1}{2}\right)}{N} \tag{1.16}$$

where $\theta_j$ is the angle of a particular molecule or polymer segment "*j*" relative to the director and *N* is the number of terms or segments in the summation. Thus, the average of all molecules or segments relative to the director provides the order parameter, and if all $\theta_j$ are 0°, then S = 1 (*i.e.* if all segments are aligned parallel to the director, the orientational order is maximized). The nuclear quadrupole interaction in our $^2$H NMR experiments lends itself well to use of eqn. 1.5 as a method of probing *S*, especially given our ability to control $\phi$ using rheo-NMR.

## 1.7 Perfluorosulfonate Ionomers

Chapters 2 and 3 of this document will explain our experiments on Nafion perfluorosulfonate ion-conducting polymers (ionomers), detailing the importance of processing, channel alignment, morphology, and water content of these polymer films.

### 1.7.1 History, Structure, and Morphology of Nafion

Since its discovery in the 1960s, Nafion has been extensively studied. It is produced by DuPont by copolymerization of tetrafluoroethylene with perfluorinated vinyl ether comonomer,[69]

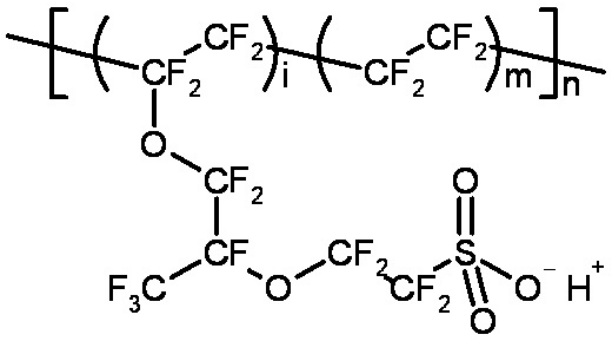

**Figure 1.18. Chemical structure of Nafion.**

and the company markets multiple variations of the ionomer, denoting each with a three or four digit suffix. The suffix is an indication of the equivalent weight (*EW*) and thickness of the film after casting. The first two digits in the suffix refer to the *EW*, while the last one or two digits refer to the thickness in thousandths of an inch (mil). Thus, Nafion 1135 has *EW* 1100 and thickness 0.0035 in. Nafion membranes with 2xx suffixes are so-called "second generation" Nafion and do not carry exactly the same designation (Nafion 212, for example, is second generation, 1100 *EW*, and 0.002 in. thickness). The structure of Nafion is shown in fig. 1.18. The *EW* can be defined as the grams of dry Nafion per mole of sulfonic acid groups, and can be determined by titration or FT-IR spectroscopy.[69] *EW* is related to the variable *m* (number of repeating tetrafluoroethylene groups) in fig. 1.18 by the following equation:

$$EW = 100m + 446 \tag{1.17}$$

*m* therefore, represents 6 – 7 repeating $C_2F_4$ units per sulfonic acid side chain in 1100 *EW* Nafion. *EW* is also related to the ion exchange capacity (*IEC*) of the ionomer by:[69]

$$IEC = \frac{1000}{EW} \tag{1.18}$$

Gierke and colleagues,[70] using wide-angle and small-angle X-ray scattering (WAXS and SAXS) suggest that Nafion forms a network of ionic clusters. They propose that approximately

10 Å channels link clusters of sulfonate-ended perfluoroalkyl ether groups measuring approximately 40 Å in diameter, organized as inverse micelles.[69,70] These water-filled clusters and channels of sulfonate groups are the presumed carrier for $H^+$ ions in the membrane. An alternative but related proposal for the morphology of Nafion has arisen from Schmidt-Rohr and Chen, in which the functional sulfonic acid groups organize into ~ 2 nm diameter hydrophilic water channels, where ion transport occurs.[71] Both models utilize the PTFE backbone of the polymer as the stabilizing hydrophobic lattice. Inconsistent crystalline structure and solubility give rise to the difficulty in determining the precise morphology of Nafion, and while the debate continues in the literature, it is beyond the scope of this dissertation.

### 1.7.2 Polymer Electrolyte Membrane (PEM) Fuel Cells

PEM fuel cells are just one of several types of fuel cells currently being researched heavily in both academia and industry. As an energy conversion medium, fuel cells have the potential to alleviate some portion of the current dependency on non-renewable resources such as coal and crude oil, though a method for cheap and clean $H_2$ or MeOH production would still be required for wide application of fuel cells. At the basic level, a PEM fuel cell consists of a membrane electrode assembly (MEA), catalyst layers, cathode/anode backings, and current collectors.[72] The MEA is located at the center of the fuel cell, and is composed of an ionomer film such as Nafion or Flemion.[72-75] The other layers are structured around the MEA, which is responsible for ferrying $H^+$ from the anode to the cathode.

In an operating fuel cell, $H_2$ gas flows in, contacting the catalyst layer and breaking into two hydrogen ions and two electrons. Simultaneously, $O_2$ molecules from air flowing into the system strike the catalyst layer on the opposite side, breaking into oxygen ions. The catalyst layers are typically composed of spherical particles of platinum or a platinum/ruthenium

complex[76] affixed to a carbon cloth matrix.[72] Protons are transported across the ionomer membrane due to a gradient in chemical potential, while electrons are sent through the current collector due to the difference in electric potential, where they provide power to an external system. The lone byproduct of this fuel cell reaction is water. Depending on the application, cell stack size, and requirements, fuel cells can be designed to provide power from a less than a watt to hundreds of kilowatts.[72] In addition to their potential use as a power source for transportation applications, fuel cells can also be adapted to provide power for homes, generators, and even portable devices such as laptops or cellular phones.

The efficient operation of the fuel cell depends in large part on the type of polymer film chosen for use in the MEA. Our group believes that orientational order (on various length scales) provides a key link to the effectiveness of the polymer film, as the orientation of the hydrophilic channels in the film appear to greatly influence proton transport.[10,54,66,77] It can be envisioned that an ionomer wherein the ion-conducting channels are aligned through the plane of the film would provide protons a less tortuous path across the membrane, resulting in increased cell efficiency. A number of absorption, conductivity, diffusion, and transport studies, as well as typical characterization and rheology experiments have been performed on Nafion[10,54,78,79] and alternative ionomer films.[77,80,81] Detailed knowledge of nanoscale chemical and morphological properties will allow for these ionomers to be tuned to maximum efficiency.[69]

### 1.8 Wormlike Micelles

Wormlike micelles (WLMs; *a.k.a.* cylindrical, rodlike, or threadlike micelles) were first introduced in 1983 by Dow as viscoelastic surfactants for use as viscosity modifiers in personal care products and liquid dish detergents.[82] Chapters 4 and 5 of this work will detail our investigations employing rheo-NMR, PFG NMR, and solution rheology to study the effects of

orientational order on magnetic alignment of WLMs and elucidate the Leslie-Ericksen viscoelastic parameters for the first time in a WLM.[23] Despite nearly thirty years of investigation and use in commercial products, micellar dynamics and their complex viscoelastic behavior in the presence of shear and magnetic fields remain an area of soft materials that is not well understood. Our work aims to form a deeper understanding of these behaviors and aid in the development of additional micellar materials and applications of WLMs.

### 1.8.1 Structure and Behavior of WLMs

Molecular amphiphiles, containing both hydrophobic and hydrophilic functionalities, can self-assemble in solution into small supramolecular structures, at their critical micelle concentration (*CMC*) due overwhelmingly to the hydrophobic effect (unfavorable contact of the hydrophobic functionality with the polar solvent).[83] These structures are commonly referred to as micelles, and can take the form of spheres, lamellae, vesicles, or cylinders.[83,84] The specific size and shape is dependent on molecular geometry, charge, the relative sizes of hydrophobic and hydrophilic groups, temperature, and concentration.[83,85-87] Shape predictions can be made based on the critical packing parameter, *CP*,[88] though it should be noted that surfactant packing is also dependent on thermodynamics and intra- and inter-micellar interactions.[86-88]

$$CP = \frac{V}{l_c a_s} \tag{1.19}$$

where $V$ is the volume of the hydrophobic "tail" with maximum effective length $l_c$, and $a_s$ is the hydrophilic "head" area per molecule at the surfactant-solvent interface. If $CP \leq \frac{1}{3}$, spheres are expected; for $\frac{1}{3} \leq CP \leq \frac{1}{2}$, cylinders will form; and for $CP \geq \frac{1}{2}$, lamellae are predicted.[86] Living epitaxial (incremental, longitudinal) growth[89,90] of WLMs is a result of the system attempting to minimize free energy by reducing the number of micelle "end caps."

WLM systems exhibit properties similar to polymer solutions, such as nonlinear stress-strain behavior, as the wormlike "chains" can move and entangle with each other just like those

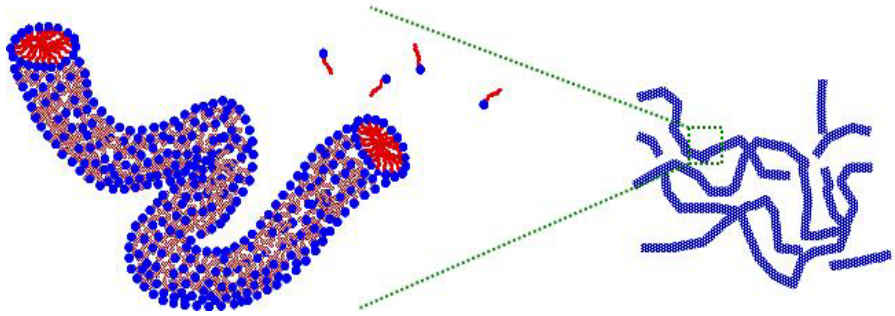

**Figure 1.19. Illustration of wormlike micelle** formation showing ability of wormlike micelles to act as an entangled polymer.

of a polymer.[25,91] These materials are the subject of significant contemporary research, as they have myriad applications: viscosity modifier additives in personal care products,[92] lubricants in district heating and cooling systems,[92] drug delivery agents,[93] electrospun tissue scaffolds,[94] and fracturing fluids in oil fields.[82] Ketner *et al.* have developed a photosensitive switch which undergoes a *cis-trans* isomerization and changes rheological behavior as a response to UV radiation.[95] WLMs have also been made polymerizable,[96] can form viscoelastic gels useful in nanomaterial manufacture,[97] and have been shown to form polymerization templates which result in polymers having high aspect ratio and narrow polydispersity.[98]

Above the critical entanglement concentration $C_e$, WLMs will form a transient, entangled network, similar to a polymer solution (see fig. 1.19). These entangled micelles can align to act as a lyotropic (concentration dependent) nematic (uniaxial long-range order) liquid crystal.[99] A common ionic surfactant which can form into a nematic WLM under appropriate conditions is cetyltrimethylammonium bromide (CTAB, cetyl = hexadecyl) in water. The structure of CTAB is shown in fig. 1.20. Our studies in chapters 4 and 5 examine CTAB in water at concentrations

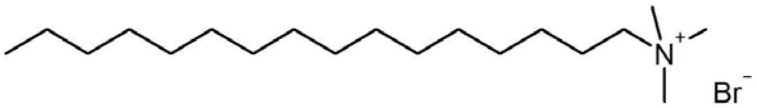


**Figure 1.20. Chemical structure of CTAB.**

of 16 – 26 wt %, above $C_e$ for CTAB (~ 16 wt %). Here, the WLM system forms cylinders of ~ 4 nm diameter[100] and of order 100 nm length[86] (note, however, that the contour length of WLMs is almost certainly a broad distribution and literature results range from tens of nm to several μm). Understanding of the hysteresis and dynamics present in complex fluids such as WLMs provides fundamental information on surfactant alignment and phase behavior, and our work can lead to improvements in the design of micellar materials and advancements in coatings, lubricants, oil extraction, and tissue engineering.

**References**


(1) Rabi, I. I.; Zacharias, J. R.; Millman, S.; Kusch, P. *Phys. Rev.* **1938**, *53*, 318.

(2) Skoog, D. A.; Holler, F. J.; Nieman, T. A. In *Principles of Instrumental Analysis*; 5th ed.; Thomson Learning, Inc.: Toronto, 1998.

(3) Levitt, M. H. *Spin Dynamics: Basics of Nuclear Magnetic Resonance*; Wiley: Chichester, 2001.

(4) Evans, J. N. S. *Biomolecular NMR Spectroscopy*; Oxford University Press: New York, 1995.

(5) Mirau, P. A. *A Practical Guide to Understanding the NMR of Polymers*; John Wiley & Sons: Hoboken, NJ, 2005.

(6) Roberts, J. D. *ABCs of FT-NMR*; University Science Books: Sausalito, CA, 2000.

(7) Alpert, N. L. *Phys. Rev.* **1947**, *72*, 637.

(8) Schmidt-Rohr, K.; Spiess, H. W. *Multidimensional Solid-State NMR and Polymers*; Academic Press: San Diego, 1994.

(9) Li, J.; Wilmsmeyer, K. G.; Madsen, L. A. *Macromolecules* **2008**, *41*, 4555-4557.

(10) Li, J.; Wilmsmeyer, K. G.; Madsen, L. A. *Macromolecules* **2009**, *42*, 255-262.

(11) Madsen, L. A. *Macromolecules* **2006**, *39*, 1483-1487.

(12) Suresh, G.; Pandey, A. K.; Goswami, A. *Journal of Membrane Science* **2006**, *284*, 193-197.

(13) Rankothge, M.; Haryadi; Moran, G.; Hook, J.; Vangorkom, L. *Solid State Ionics* **1994**, *67*, 241-248.

(14) *NMR of Ordered Liquids*; Burnell, E. E.; de Lange, C. E., Eds.; Kluwer: Dordrecht, 2003.

(15) Emsley, J. W.; Lindon, J. C. *NMR Spectroscopy Using Liquid Crystal Solvents*; First ed.; Pergamon Press: New York, 1975.

(16) Fischer, E.; Callaghan, P. T. *Phys. Rev. E* **2001**, *6401*.

(17) Becker, P.; Siebert, H.; Noirez, L.; Schmidt, C. *Macromolecular Symposia* **2005**, *220*, 111-122.

(18) Callaghan, P. T.; Samulski, E. T. *Macromolecules* **2003**, *36*, 724-735.

(19) Veron, A.; Gomes, A. E.; Leal, C. R.; Van der Klink, J.; Martins, A. F. *Molecular Crystals and Liquid Crystals Science and Technology Section a-Molecular Crystals and Liquid Crystals* **1999**, *331*, 2359-2367.

(20) Cheng, C. Y.; Hwang, L. P. *Journal of the Chinese Chemical Society* **2001**, *48*, 953-962.

(21) Angelico, R.; Burgemeister, D.; Ceglie, A.; Olsson, U.; Palazzo, G.; Schmidt, C. *Journal of Physical Chemistry B* **2003**, *107*, 10325-10328.

(22) Clawson, J. S.; Holland, G. P.; Alam, T. M. *Phys. Chem. Chem. Phys.* **2006**, *8*, 2635-2641.

(23) Wilmsmeyer, K. G.; Zhang, X.; Madsen, L. A. *Soft Matter* **2012**, *8*, 57-60.

(24) Douglass, B. S.; Colby, R. H.; Madsen, L. A.; Callaghan, P. T. *Macromolecules* **2008**, *41*, 804-814.

(25) Lopez-Gonzalez, M. R.; Holmes, W. M.; Callaghan, P. T. *Soft Matter* **2006**, *2*, 855-869.

(26) Stejskal, E. O.; Tanner, J. E. *J. Chem. Phys.* **1965**, *42*, 288-292.

(27) Sperling, L. H. *Introduction to Physical Polymer Science*; Fourth ed.; John Wiley & Sons, Inc.: Hoboken, NJ, 2006.

(28) Allcock, H. R.; Lampe, F. W.; Mark, J. E. *Contemporary Polymer Chemistry*; Third ed.; Pearson Education, Inc.: Upper Saddle River, NJ, 2003.

(29) Liu, B.; Shaw, M. T. *Journal of Rheology* **2001**, *45*, 641-657.

(30) Oseen, C. W. *Transactions of the Faraday Society* **1933**, *29*, 883.

(31) Zocher, H. *Transactions of the Faraday Society* **1933**, *29*, 945.

(32) Frank, F. C. *Discussions Faraday Soc.* **1958**, *25*, 19-28.

(33) Ericksen, J. L. *Trans. Soc. Rheol.* **1961**, *5*, 23-34.

(34) Ericksen, J. L. *Arch. Rat. Mech. Anal.* **1962**, *9*, 371-378.

(35) Leslie, F. M. *Arch. Rat. Mech. Anal.* **1968**, *28*, 265-283.

(36) Maier, W.; Saupe, A. *Z. Naturforsch.* **1958**, *13A*, 564.

(37) Larson, R. G. *Constitutive Equations for Polymer Melts and Solutions*; Butterworth Publishers: Stoneham, 1988.

(38) de Gennes, P. G.; Prost, J. *The Physics of Liquid Crystals*; Second ed.; Oxford University Press: New York, 1993.

(39) Lukaschek, M.; Kothe, G.; Schmidt, C.; Gomes, A. E.; Polimeno, A. *J. Chem. Phys.* **2002**, *117*, 4550-4556.

(40) Orian, L.; Feio, G.; Veron, A.; Martins, A. F. *Molecular Crystals and Liquid Crystals* **2003**, *394*, 63-75.

(41) Parodi, O. *J. Phys.-Paris* **1970**, *31*, 581-584.

(42) Onsager, L. *Annals of the New York Academy of Sciences* **1949**, *51*, 627.
(43) Miesowicz, M. *Nature* **1935**, *136*, 261.
(44) Miesowicz, M. *Nature* **1946**, *158*, 27.
(45) Callaghan, P. T. *Rep. Prog. Phys.* **1999**, *62*, 599-670.
(46) Callaghan, P. T. *Current Opinion in Colloid & Interface Science* **2006**, *11*, 13-18.
(47) Martins, A. F.; Esnault, P.; Volino, F. *Phys. Rev. Lett.* **1986**, *57*, 1745-1748.
(48) Esnault, P.; Casquilho, J. P.; Volino, F.; Martins, A. F.; Blumstein, A. *Liquid Crystals* **1990**, *7*, 607-628.
(49) Nakatani, A. I.; Poliks, M. D.; Samulski, E. T. *Macromolecules* **1990**, *23*, 2686-2692.
(50) Callaghan, P. T.; Gil, A. M. *Rheologica Acta* **1999**, *38*, 528-536.
(51) Kilfoil, M. L.; Callaghan, P. T. *Macromolecules* **2000**, *33*, 6828-6833.
(52) Uludag, Y.; McCarthy, M. J.; Barrall, G. A.; Powell, R. L. *Macromolecules* **2001**, *34*, 5520-5524.
(53) Tripathi, A.; Tam, K. C.; McKinley, G. H. *Macromolecules* **2006**, *39*, 1981-1999.
(54) Li, J.; Wilmsmeyer, K. G.; Hou, J. B.; Madsen, L. A. *Soft Matter* **2009**, *5*, 2596-2602.
(55) Atkin, J. M.; Cormier, R. J.; Callaghan, P. T. *Journal of Magnetic Resonance* **2005**, *172*, 91-97.
(56) Badiger, M. V.; Rajamohanan, P. R.; Suryavanshi, P. M.; Ganapathy, S.; Mashelkar, R. A. *Macromolecules* **2002**, *35*, 126-134.
(57) Callaghan, P. T.; Gil, A. M. *Macromolecules* **2000**, *33*, 4116-4124.
(58) Douglass, B. S.; Cormier, R. J.; Callaghan, P. T. *Physical Review E* **2007**, *75*.
(59) Cormier, R. J.; Schmidt, C.; Callaghan, P. T. *Journal of Rheology* **2004**, *48*, 881-894.
(60) Hubbard, P. L.; McGrath, K. M.; Callaghan, P. T. *Langmuir* **2006**, *22*, 3999-4003.
(61) Lopez-Gonzalez, M. R.; Holmes, W. M.; Callaghan, P. T.; Photinos, P. J. *Physical Review Letters* **2004**, *93*.
(62) Berret, J. F.; Roux, D. C.; Porte, G. *Journal De Physique II* **1994**, *4*, 1261-1279.
(63) Hollingsworth, K. G.; Johns, M. L. *Journal of Rheology* **2004**, *48*, 787-803.
(64) Collings, P. J. *Liquid Crystals: Nature's Delicate Phase of Matter*; Second ed.; Princeton University Press: Princeton, NJ, 2002.
(65) Holmes, W. M.; Lopez-Gonzalez, M. R.; Callaghan, P. T. *Europhysics Letters* **2003**, *64*, 274-280.

(66) Li, J.; Park, J. K.; Moore, R. B.; Madsen, L. A. *Nature Materials*, *10*, 507-511.

(67) Reuvers, A. J. *Progress in Organic Coatings* **1999**, *35*, 171-181.

(68) Valentine, K. G.; Pometun, M. S.; Kielec, J. M.; Baigelman, R. E.; Staub, J. K.; Owens, K. L.; Wand, A. J. *Journal of the American Chemical Society* **2006**, *128*, 15930-15931.

(69) Mauritz, K. A.; Moore, R. B. *Chemical Reviews* **2004**, *104*, 4535-4585.

(70) Gierke, T. D.; Munn, G. E.; Wilson, F. C. *Journal of Polymer Science Part B-Polymer Physics* **1981**, *19*, 1687-1704.

(71) Schmidt-Rohr, K.; Chen, Q. *Nature Materials* **2008**, *7*, 75-83.

(72) Barbir, F. *PEM Fuel Cells: Theory and Practice*; Elsevier Academic Press: Boston 2005.

(73) Kerres, J.; Ullrich, A.; Haring, T.; Baldauf, M.; Gebhardt, U.; Preidel, W. *Journal of New Materials for Electrochemical Systems* **2000**, *3*, 229-239.

(74) Sacca, A.; Carbone, A.; Pedicini, R.; Portale, G.; D'Ilario, L.; Longo, A.; Martorana, A.; Passalacqua, E. *Journal of Membrane Science* **2006**, *278*, 105-113.

(75) Tsushima, S.; Teranishi, K.; Hirai, S. *Energy* **2005**, *30*, 235-245.

(76) Tong, Y. Y.; Kim, H. S.; Babu, P. K.; Waszczuk, P.; Wieckowski, A.; Oldfield, E. *Journal of the American Chemical Society* **2002**, *124*, 468-473.

(77) Hou, J.; Li, J.; Madsen, L. A. *Macromolecules* **2010**, *43*, 347-353.

(78) Hietala, S.; Maunu, S. L.; Sundholm, F. *Journal of Polymer Science Part B-Polymer Physics* **2000**, *38*, 3277-3284.

(79) Baglio, V.; Arico, A. S.; Antonucci, V.; Nicotera, I.; Oliviero, C.; Coppola, L.; Antonucci, P. L. *Journal of Power Sources* **2006**, *163*, 52-55.

(80) Wu, H. L.; Ma, C. C. M.; Li, C. H.; Lee, T. M.; Chen, C. Y.; Chiang, C. L.; Wu, C. *Journal of Membrane Science* **2006**, *280*, 501-508.

(81) Roy, A.; Hickner, M. A.; Yu, X.; Li, Y. X.; Glass, T. E.; McGrath, J. E. *Journal of Polymer Science Part B-Polymer Physics* **2006**, *44*, 2226-2239.

(82) Chase, B.; Chmilowski, W.; Marcinew, R.; Mitchell, C.; Dang, Y.; Krauss, K.; Nelson, E.; Lantz, T.; Parham, C.; Plummer, J. *Oilfield Review* **1997**, *9*, 20-33.

(83) Evans, D. F.; Ninham, B. W. *J. Phys. Chem.* **1986**, *90*, 226-234.

(84) Cates, M. E.; Candau, S. J. *J. Phys.: Condens. Matter* **1990**, *2*, 6869-6892.

(85) Bulut, S.; Hamit, J.; Olsson, U.; Kato, T. *European Physical Journal E* **2008**, *27*, 261-273.

(86) Dreiss, C. A. *Soft Matter* **2007**, *3*, 956-970.

(87) Schurtenberger, P.; Cavaco, C.; Tiberg, F.; Regev, O. *Langmuir* **1996**, *12*, 2894-2899.

(88) Israelachvili, J. N. *Intermolecular and Surface Forces*; Academic Press: London, 1992.

(89) Cambridge, G.; Guerin, G.; Manners, I.; Winnik, M. A. *Macromolecular Rapid Communications*, *31*, 934-938.

(90) Qian, J.; Guerin, G.; Lu, Y.; Cambridge, G.; Manners, I.; Winnik, M. A. *Angewandte Chemie-International Edition*, *50*, 1622-1625.

(91) Candau, S. J.; Hirsch, E.; Zana, R. *Journal of Colloid and Interface Science* **1985**, *105*, 521-528.

(92) Yang, J. *Curr. Opin. Colloid & Interface Sci.* **2002**, *7*, 276-281.

(93) Kim, Y.; Dalhaimer, P.; Christian, D. A.; Discher, D. E. *Nanotechnology* **2005**, *16*, S484-S491.

(94) McKee, M. G.; Layman, J. M.; Cashion, M. P.; Long, T. E. *Science* **2006**, *311*, 353-355.

(95) Ketner, A. M.; Kumar, R.; Davies, T. S.; Elder, P. W.; Raghavan, S. R. *Journal of the American Chemical Society* **2007**, *129*, 1553-1559.

(96) Liu, S. Y.; Gonzalez, Y. I.; Danino, D.; Kaler, E. W. *Macromolecules* **2005**, *38*, 2482-2491.

(97) Vasudevan, M.; Buse, E.; Lu, D. L.; Krishna, H.; Kalyanaraman, R.; Shen, A. Q.; Khomami, B.; Sureshkumar, R. *Nature Mater.* **2010**, *9*, 436-441.

(98) Walker, L. M.; Kuntz, D. M. *Curr. Opin. Colloid & Interface Sci.* **2007**, *12*, 101-105.

(99) Kuntz, D. M.; Walker, L. M. *Soft Matter* **2008**, *4*, 286-293.

(100) Coppola, L.; Gianferri, R.; Nicotera, I.; Oliviero, C.; Ranieri, G. A. *Phys. Chem. Chem. Phys.* **2004**, *6*, 2364-2372.

# Chapter 2

## Hydrophilic Channel Alignment Modes in Perfluorosulfonate Ionomers: Implications for Proton Transport

Reprinted with permission from J. Li, K.G. Wilmsmeyer and L.A. Madsen, *Macromolecules* **2008**, *41*, 4555-4557 © 2008, American Chemical Society.

### 2.1 Introduction

What factors influence ionic conductivity in advanced polymer electrolytes? Clearly, chemically or electrically driven transport through ionic polymers depends on numerous phenomena, many of which may not even be known. Ionic polymer features such as crystallinity and ionic aggregate size have been measured using XRD, NMR, and electron microscopy,[1] but this morphological realm requires deeper exploration. If we can more completely assess morphological properties of these electrolytes, we can optimize and tailor them to suit diverse applications in polymer-electrolyte-membrane (PEM) fuel cells, reverse osmosis membranes, and "artificial muscle" polymer actuators.

One phenomenon that has received little attention in terms of membrane design is long-range orientational order. Perfluorosulfonate ionomers such as DuPont's Nafion exhibit a phase separated structure, where protons conduct via ionically coordinated, water-swollen hydrophilic channels.[1] We present detailed orientational order measurements in two leading Nafion membranes using a simple and quantitative method based on deuterium NMR. We demonstrate that this channel alignment is uniform over these films but has drastically different properties for the two membrane types. If we can quantify and manipulate this order, we should be able to optimize anisotropic conductivity in, *e.g.*, fuel cell membranes by maximizing channel alignment across the film plane.

Ionomer-based PEM fuel cells typically operate with 10 - 40 wt % water uptake to maximize proton conductivity.[2] Several models based on powder XRD scattering curves describe this hydrophilic phase as a network of channels and cavities that grow in size with water uptake.[3-5] Protons conduct in the acidified bath of water contained in the ion-lined channels, which provides a low activation energy environment for transport. Our initial question is, what are the alignment modes of these membrane channels?

A powerful method of determining orientational order and its dynamics in polymers lies in the use of deuterium NMR quadrupole couplings. In many cases, doping a simple deuterated probe molecule into an ordered liquid or solid provides easy access to the orientational order parameter $\boldsymbol{S}$ (a.k.a., the Hermann's orientation function) as well as to higher order tensorial orientation properties.[6] This method provides quantitative, although relative, measures of $\boldsymbol{S}$ and other order parameters, and these can be extremely useful in characterizing ordered phase behavior and symmetries. Perfluorosulfonate ionomers present an ideal case for application of this method since they heavily absorb water, which we may replace with $D_2O$. Residual quadrupole splittings $\Delta\nu_Q$ of the water deuterons report on $\boldsymbol{S}$ via[7]

$$\Delta\nu_Q = Q_P \boldsymbol{S} P_2(\cos\theta) \tag{2.1}$$

where $Qp$ is the quadrupole coupling constant ($\sim$ 260 kHz) and $\boldsymbol{S} = \langle P_2(\cos\chi)\rangle$ is the ensemble average over the second Legendre polynomial with $\chi$ the angle between a particular OD bond axis and the alignment axis of the material. $\theta$ defines the angle between the material alignment axis and the spectrometer magnetic field $\mathbf{B_0}$. In the case of nonuniaxial alignment, we may replace $\boldsymbol{S}P_2(\cos\theta)$ in eqn. 2.1 with appropriate tensorial equations to extract various asymmetry parameters. This temporal and spatial ensemble average gives rise to "inherited" order of the deuterated probe solute molecules as they interact with an anisotropic matrix.[6,8] Partial ordering

results from biased rotations, collisions, and librations of these $D_2O$ probe molecules. In Nafion, which consists of interconnected voids and channels, one observes a single deuterium doublet spectrum (splitting) only if there is alignment of these channels macroscopically over the membrane. Orientational distributions of domains larger than the diffusion length of $D_2O$ on the $1/Qp$ time scale ($\sim$ 100 nm and $\sim$ 10 $\mu$s, respectively) manifest as superpositions of deuterium doublets which will broaden and provide additional structure to the observed spectrum. Previous studies using residual $^2$H NMR quadrupolar interactions in perfluorosulfonate ionomers[9] did not include sufficient measurements to define membrane alignment tensor properties and included substantial dead volume in those sample cells. Our sealed and equilibrated low-dead-volume sample cell provides exquisitely reproducible and quantifiable results.

**2.2 Materials and Methods**

50 μm thick Nafion 112 (N112, extruded) and Nafion NRE212 (dispersion-cast) membranes, and 175 μm thick (extruded) Nafion 117 (N117) membrane, all nominally 1100 equivalent weight (*EW*) per sulfonate group, were obtained from E.I. DuPont (Wilmington, DE). Deuterium oxide was obtained from Cambridge Isotope Laboratories, Inc. (Andover, MA) at 99.9% purity. 175 μm and 90 μm thick dispersion-cast membranes were obtained from Gas Hub Inc. (Singapore).

All NMR experiments were performed on a Bruker Avance III WB NMR spectrometer (Bruker-Biospin, Billerica, MA) at a magnetic field of 9.4 T, corresponding to a $^2$H frequency of 61.4 MHz. A single channel detection static solids probe with a 10.7 mm inside diameter horizontal solenoid coil was used.

N112 membranes were cut into 6 × 6 mm pieces with one edge along the extrusion striate. The orientation was confirmed by polarizing microscopy (Meiji Technology MX9430,

Japan). NRE212 was cut into the same size with an arbitrary orientation relative to the film sheet. For both Nafion samples, 10 pieces were stacked in exactly the same orientation to enhance the NMR signal. The stacks of dry membranes were placed in a 40 °C oven for several hours, weighed, then loosely wrapped with Teflon pipe seal tape and soaked in $D_2O$ for at least a week. The maximum $D_2O$ uptakes, expressed in wt %, were measured by the weight gain versus the weight of the dry membranes. The wt % of unsaturated membranes was measured by the membrane stack weight and confirmed with relative NMR spin intensity. Before NMR experiments, the membrane stacks were wrapped with Teflon tape and LDPE plastic wrap and sealed in a Delrin sample cell. The sample cell contains a slit for the membrane stack and a pressure fit piston cap to seal and allow the membrane sample to equilibrate with very low dead volume, and it can be rotated in the NMR coil casing. A goniometer was used to ensure accurate orientation of the sample cell.

NMR experiments are performed with a simple free induction decay (FID) acquisition following a single pulse of 4 μs ($\pi/2$ pulse = 6 μs) and a delay time of 0.5 s for 256 to 1024 scans. The deuterium quadrupole splittings were extracted from the data by fitting each spectrum with two Lorentzian peaks using NutsPro software (Acorn NMR Inc., Livermore, CA). A calibration curve of splitting versus wt % was established for each sample by running consecutive NMR experiments with the sample cell cap removed and allows $D_2O$ to slowly evaporate from the membranes over a period of 2 - 3 days. Peak areas, along with gravimetric calibration data, were used to calculate wt % of actual $D_2O$ in membranes as a function of time. Angle between the membrane sample cell and the static magnetic field was varied in 15 degree steps from 0º to 90º. The error in determining the angle was estimated at ± 1.5°. At room temperature, $T_1$ values are 200 ms for saturated membranes and 40 ms for nearly dry

membranes. Initial experiments performed on 175 μm and 90 μm thick dispersion-cast films obtained from Gas Hub Inc. (Singapore) showed similar behavior to the NRE212 membrane (uniaxial order perpendicular to membrane plane), although with slightly lower degrees of order present. Initial experiments performed on 175 μm thick extruded N117 also shows maximal order along the extrusion direction, but ~ 5X less than in N112.

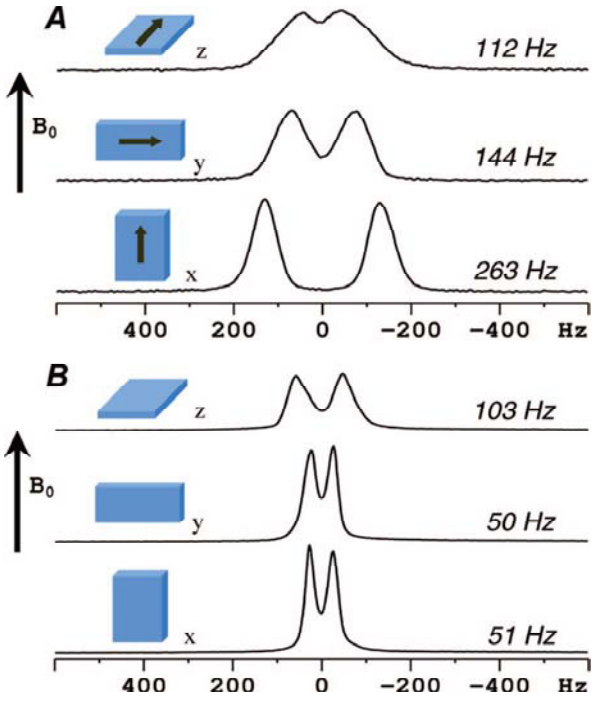


**Figure 2.1. Room temperature $^2$H NMR spectra of two Nafion membranes swollen with 13 wt % D2O.** (A) Extruded Nafion 112. The arrows indicate the extrusion direction. (B) Dispersion-cast Nafion NRE212. The rectangular blocks in blue indicate different membrane directions (*x*, *y*, *z*) with respect to the spectrometer $\mathbf{B_0}$ field, where the membrane *z*-axis is perpendicular to the plane. The splitting values $\Delta\nu_Q$ at right result from nonlinear least-squares fits to each spectrum.

### 2.3 Results and Discussion

Figure 2.1 shows $^2$H NMR spectra as a function of membrane angles with respect to $\mathbf{B_0}$ for DuPont extruded N112 and the latest dispersion-cast NRE212 membranes. Dramatic features of Nafion morphology become apparent due to these data. Both membranes show nearly uniform order, but in perpendicular directions, and with different symmetries. Part A shows that extruded N112 channels align along the extrusion direction, as expected due to extrusion and shear forces, and we further observe that this membrane is biaxially aligned with asymmetry parameter $\eta = 0.12 \pm 0.02$ given by $\eta = |\Delta\nu_Q^y - \Delta\nu_Q^z|/\Delta\nu_Q^x$. The superscripts *x*, *y*, or *z* given on $\Delta\nu_Q$ here denote splittings with the noted membrane axis relative to $\mathbf{B_0}$. Part B shows that, somewhat surprisingly, the dispersion-cast

NRE212 channels uniformly align across the membrane plane and with uniaxial symmetry ($\eta$ = 0). We propose that this alignment arises from casting solvent flow during evaporation and conceivably other annealing processes. Dispersion-cast Nafion from other sources (Gas Hub Inc.) also show uniform uniaxial through-plane alignment. Prominently featured in these nominally chemically equivalent systems, which differ only by processing, we observe a factor of > 2.5 better alignment in the extruded case, indicating that we may substantially improve through-plane order of dispersion-cast films.

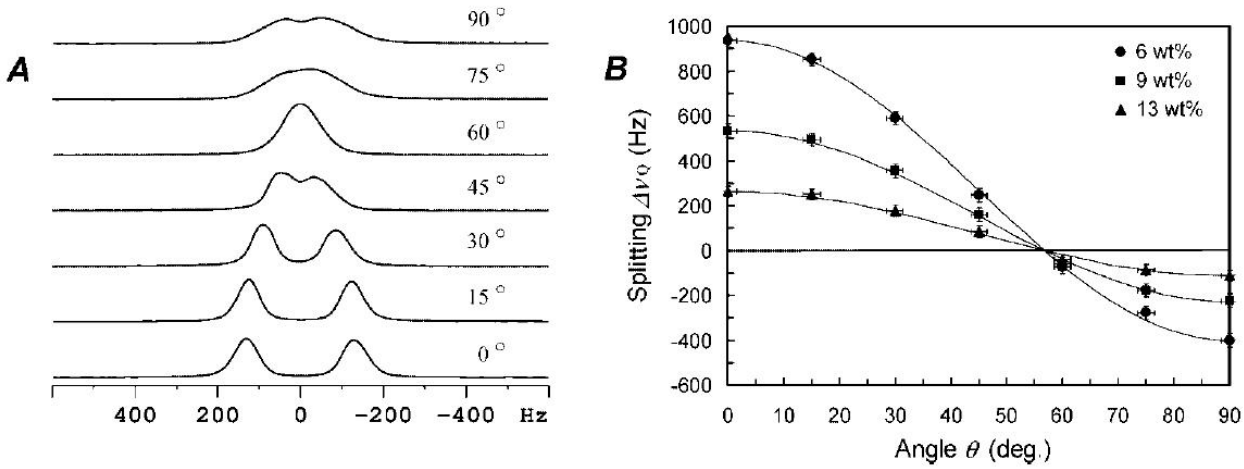


**Figure 2.2.** (A) $^2$H NMR spectra vs rotation angle of N112 with 13 wt % $D_2O$. (B) Plots of quadrupole splitting $\Delta\nu_Q$ vs angle $\theta$ of the extrusion direction relative to the spectrometer field $\mathbf{B_0}$ over a range of $D_2O$ uptake. Solid lines are fitted curves using eqn. 2.2, where $\eta$ = 0.12 provides best fits for all curves and is the only adjustable fit parameter after specifying $\Delta\nu_0$, the spectral splitting at $\theta = 0$. The error estimate for $\eta$ based on all our data fits is ± 0.02.

Figure 2.2A shows NMR spectra as a function of N112 membrane angle $\theta$ with respect to $\mathbf{B_0}$, rotating about the membrane *y*-axis. Because of the membrane biaxiality, $\theta$ follows a dependence given by[6,7,10,11]

$$\Delta\nu_Q = \frac{1}{2}\Delta\nu_0[3\cos^2\theta - 1 + \eta\sin^2\theta] \tag{2.2}$$

which we may use to fit splittings as a function of angle and wt % $D_2O$ uptake, shown in fig. 2.2B. Here we note that the biaxiality of $\eta$ = 0.12 is stable over a large range of hydration level

(at least from 4 to 20 wt % based on further data), indicating that the degree and symmetries of alignment in these channels are stable vs hydration. A similar analysis shows that NRE212 exhibits $\eta = 0$.

Figure 2.3 depicts models for the channel morphologies in these membranes. Parts A and B show two possibilities, consistent with our data, for the extruded N112 channel morphology. Part A depicts biaxial (elliptical) channels aligned uniaxially along the extrusion direction, while part B depicts uniaxial (cylindrical) channels aligned biaxially via larger local bends in-plane vs through-plane. Distinguishing between (A) and (B) requires further structural studies. Part C shows the dispersion-cast NRE212 channel morphology, consisting of cylindrical channels aligned uniaxially across the plane of the film. Note that these models and our observations do not comment on whether Nafion exhibits a cluster-network model[3] or quasi-cylindrical channel model.[4,5]

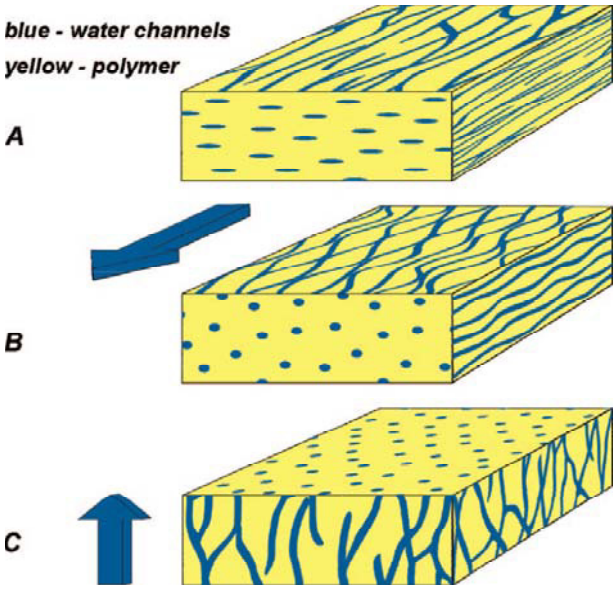


**Figure 2.3. Proposed hydrophilic channel alignment models** for N112 (A, B) and NRE212 membranes (C). (A) Biaxiality caused by ellipsoidal channels aligned along the extrusion direction (block arrow) in the membrane plane. (B) Biaxiality caused by cylindrical channels with directional anisotropy in the membrane plane relative to across the plane (zigzag character in film plane and perpendicular to extrusion direction). (C) Uniaxially aligned cylindrical channels perpendicular to the membrane plane (block arrow). Arrow also indicates solvent evaporation gradient direction.

Various observations of fuel cell operation and membrane behavior could sensibly depend on orientational order effects. Reports of anisotropic conductivity in Nafion,[12,13] while not a settled topic in the literature, should provide correlations with orientation if we carefully

study equivalent samples. High-temperature annealing of extruded films produces increased fuel cell performance,[2,14] which might be explained by randomization of alignment in these films, producing better through-plane conductivity than unannealed N112 films aligned in-plane. Furthermore, aging of membranes in operating fuel cells, which usually requires hours or days of operation before becoming stable,[2] could result from the evolution of flow alignment of the hydrophilic channels. Our method would allow in situ characterization of membrane order, even during cell operation.

### 2.4 Concluding Remarks

To conclude, we quantitatively measure bulk channel alignment in Nafion membranes using $^2$H NMR directly on residually aligned absorbed $D_2O$. This method of using deuterated probe molecules to interrogate order may be conducted on almost any NMR spectrometer and does not require complicated sample mounting or sectioning for film cross sections to interact with, *e.g.*, an X-ray or neutron beam. Furthermore, we note that numerical quantification of order properties such as the biaxiality parameter is straightforward using this method, as opposed to with XRD, polarizing microscopy, or other methods. We present results for two perfluorosulfonate ionomer membranes showing that channels are biaxially oriented ($\eta = 0.12$) in the membrane plane for extruded membranes, whereas channels are uniaxially oriented perpendicular to the plane for dispersion-cast membranes. We propose that control over the direction and extent of orientational order of the hydrophilic channels will allow increased material design freedom and improvements in ionomer device performance, *e.g.*, increased proton conductivity across the membrane plane in fuel cells. Further detailed studies of $^2$H NMR quadrupole splittings vs $D_2O$ uptake and temperature and direct correlations with proton conductivity anisotropy are underway.

**References**


(1) Mauritz, K. A.; Moore, R. B. *Chemical Reviews* 2004, *104*, 4535-4585.

(2) Zhao, T. S.; Kreuer, K. D.; Nguyen, T. V. *Advances in Fuel Cells*; Elsevier: Amsterdam, 2007; Vol. 1.

(3) Gierke, T. D.; Munn, G. E.; Wilson, F. C. *Journal of Polymer Science Part B Polymer Physics* 1981, *19*, 1687-1704.

(4) Rubatat, L.; Gebel, G.; Diat, O. *Macromolecules* 2004, *37*, 7772-7783.

(5) Schmidt-Rohr, K.; Chen, Q. *Nature Materials* 2008, *7*, 75-83.

(6) *NMR of Ordered Liquids*; Burnell, E. E.; de Lange, C. E., Eds.; Kluwer: Dordrecht, 2003.

(7) Callaghan, P. T.; Samulski, E. T. *Macromolecules* 2003, *36*, 724-735.

(8) Deloche, B.; Samulski, E. T. *Macromolecules* 1981, *14*, 575-581.

(9) Rankothge, M.; Haryadi; Moran, G.; Hook, J.; Vangorkom, L. *Solid State Ionics* 1994, *67*, 241-248.

(10) Madsen, L. A.; Dingemans, T. J.; Nakata, M.; Samulski, E. T. *Physical Review Letters* 2004, *92*, 145505.

(11) Severing, K.; Saalwachter, K. *Physical Review Letters* 2004, *92*, 125501.

(12) Cable, K. M.; Maurtiz, K. A.; Moore, R. B. *Chemistry of Materials* 1995, *7*, 1601-1603.

(13) Ma, S.; Siroma, Z.; Tanaka, H. *Journal of the Electrochemical Society* 2006, *153*, A2274-A2281.

(14) Hensley, J. E.; Way, J. D.; Dec, S. F.; Abney, K. D. *Journal of Membrane Science* 2007, *298*, 190-201.

# Chapter 3

## Anisotropic Diffusion and Morphology in Perfluorosulfonate Ionomers Investigated by NMR

Reprinted with permission from J. Li, K.G. Wilmsmeyer and L.A. Madsen, *Macromolecules* **2009**, *42*, 255-262 © 2009, American Chemical Society.

### 3.1 Abstract

Anisotropy in ionomer membranes represents a powerful interaction for modulating properties such as mechanical moduli, thermal expansions, and small molecule transport, all tunable via controlled processing. We observe uniform hydrophilic channel alignment in three perfluorosulfonate ionomer membrane types, quantified by $^2$H NMR spectroscopy of absorbed $D_2O$ molecules. Our measurements show biaxial or uniaxial in-plane alignment for extruded membranes, but uniaxial through-plane alignment for dispersion-cast membranes, and further demonstrate affine swelling with both water uptake and thermal expansion. In order to correlate alignment data with a quantity relevant to proton transport, we measure the anisotropy of water self-diffusion using pulsed-field-gradient NMR along different membrane directions. Extruded membranes with stronger alignment exhibit 18 % faster in-plane diffusion than through-plane diffusion, while diffusion anisotropy is minimal for weakly aligned membranes. These results should lead to a more quantitative understanding of and control over membrane properties via manipulation of molecular order.

### 3.2 Introduction

Perfluorosulfonate ionomers have diverse applications in polymer electrolyte membrane (PEM) fuel cells, reverse-osmosis water desalinization membranes, and "artificial muscle" polymer actuators.[1] In most applications, small polar or ionic mobile solutes such as water, ionic

liquids, lithium or protons transport through the membrane plane via a nanometer-scale hydrophilic phase. Proton conductivity measurements on some of these ionomers have shown substantial directional anisotropy, but with limited quantitative understanding. Ma *et al.*[2] have reported anisotropic conductivity for in-plane relative to through-plane directions in hot pressed Nafion 117 (N117). Cable *et al.*[3] have also demonstrated in-plane conductivity anisotropy in uniaxially oriented N117, and correlated this with SAXS measurements. Our previous brief study[4] showed distinct oriented morphologies in two Nafion membranes processed under different conditions via $^2$H NMR spectroscopy. Thus, transport anisotropy is undoubtedly influenced by the oriented morphology. Ionic polymer features such as crystallinity and ionic aggregate size and dimensionality have been measured using XRD,[5-9] NMR,[4,10-12] and electron microscopy,[13] but links between orientation and transport require deeper and more quantitative investigation.

We aim to quantitatively assess both morphological structure and transport properties of these membranes in order to build models for membrane behaviors and to tailor membranes to suit diverse applications. Here we present a more complete picture of anisotropy by incorporating a third membrane type (extruded Nafion 117) and conducting detailed multiaxis diffusion measurements using pulsed-field-gradient NMR. We observe clear diffusion anistropy in the most oriented membrane (extruded Nafion 112), which clearly correlates with molecular anisotropy ($^2$H NMR) measurements. We further map out the sensitive dependence of $^2$H NMR spectral splittings as a function of water uptake, temperature, and membrane type, where we confirm affine swelling of these membranes under all conditions.

### 3.2.1 Measurements of Hydrophilic Channel Anisotropy

Fuel cell membranes normally operate at 10 - 40 wt % water uptake to maximize proton conductivity. Protons conduct in the acidified bath of water contained in the ion-lined hydrophilic channels, which provides a low activation energy environment for transport. Several models based on XRD scattering curves describe this hydrophilic phase as a network of ion clusters and hydrophilic channels that grow in size with water uptake.[5-9] Induced alignment of membrane polymer chain and ion clusters are studied by XRD[3,8] showing a hierarchical scale of structure. In this work, we investigate the membrane hydrophilic channel alignment order using deuterated probe molecules, specifically $D_2O$ to replace the usual $H_2O$ present in these membranes. This method is widely used in liquid crystal and conventional polymer systems.[14] Doping a simple deuterated probe molecule into an ordered liquid or solid provides easy access to the orientational order parameter $\boldsymbol{S}$ (a.k.a., the Hermann's orientation function), as well as to higher order tensorial orientation properties.[14] This method provides quantitative, although relative, measures of $\boldsymbol{S}$ and other order parameters, and these can be extremely useful in characterizing ordered phase behavior, temperature dependencies, and phase symmetries. It may be conducted on almost any NMR spectrometer, and does not require complicated sample mounting or sectioning for film cross sections to interact with, *e.g.*, an X-ray or neutron beam. Study of perfluorosulfonate ionomers benefits greatly from application of this method since they heavily absorb water, which we replace with $D_2O$. Compared to scattering techniques,[6] which reveal the orientational order of the hydrophobic Nafion amorphous/crystalline backbone and hydrophilic ionic clusters, this $^2H$ NMR method focuses simply on the orientational order of the hydrophilic channels to which the $D_2O$ probe molecules have access. As the probe molecules diffuse in the hydrophilic channels of the membranes, they acquire partial ordering due to biased

rotations, collisions, and librations of these $D_2O$ probe molecules, including collisions with the quasi-cylindrical channel walls. This temporal and spatial ensemble average gives rise to "inherited" orientational order of the deuterated probe solute molecules as they interact with an anisotropic matrix.[14,15] The actual average order of the probe molecules is reduced compared to the order of host channels by a scaling factor. Such a "pseudonematic interaction"[16] is manifested in the quadrupole splitting of the probe molecules. In nanophase-separated ionomers such as Nafion, which consist of interconnected voids, lamellae, or channels, one observes a single deuterium doublet spectrum (splitting) only if there is alignment of these channels macroscopically over the membrane. Orientational distributions of domains larger than the diffusion length of $D_2O$ on the $1/Q_p\boldsymbol{S}$ time scale (~ 1 μm and ~ 1 ms, respectively, see eqn. 3.1) manifest as superpositions of deuterium doublet spectral components, which will thus broaden and provide additional structure to the observed spectrum.

Residual quadrupole splittings $\Delta\nu_Q$ of the water deuterons report on $\boldsymbol{S}$ via[16]

$$\Delta\nu_Q = Q_P S P_2(\cos\theta) = Q_P \rho S_{matrix} P_2(\cos\theta) \tag{3.1}$$

where $Q_p$ is the quadrupole coupling constant (~ 260 kHz), and $\boldsymbol{S} = \langle P_2(\cos\chi)\rangle$ is the ensemble average over the second Legendre polynomial with $\chi$ the angle between a particular OD bond axis and the alignment axis of the material. $\theta$ defines the angle between the material alignment axis and the spectrometer magnetic field $\mathbf{B_0}$. We are generally more interested in the order parameter of the channel network matrix itself, which can be expressed as $\boldsymbol{S} = \rho\boldsymbol{S}_{matrix}$, where $\boldsymbol{S}_{matrix} = \langle P_2(\cos\alpha)\rangle$ is the ensemble average over the second Legendre polynomial with $\alpha$ the angle between a particular channel axis and the alignment axis of the material; $\rho$ is the scaling factor determined by the interaction between the probe molecule and the host matrix. Usually, $\rho$ is fixed for a given probe-matrix system and is relatively insensitive to temperature for liquid

crystal or conventional homogeneous polymer systems.[16,17] Equation 3.1 describes a uniaxial system. In the case of an isotropic system, $\boldsymbol{S}$ would average to zero; hence a single $^2$H peak with no splitting is observed. In the case of nonuniaxial alignment, we may replace $\boldsymbol{S}P_2(\cos\theta)$ in eqn. 3.1 with appropriate tensorial equations to extract various asymmetry parameters.

### 3.2.2 The Role of Water Uptake

Water uptake in ionomer-based membranes, affected by humidity, strongly influences ionomeric fuel cell[18] and mechanical actuator performance.[19,20] Previous studies using residual $^2$H NMR quadrupolar interactions in perfluorosulfonate ionomers[10-12] usually adjust water uptake by controlling relative humidity (RH) and also leave substantial dead volume in the NMR sample cells. While modulating RH is convenient from an engineering and end-use standpoint, the downside is that moisture can still leave the membrane due to evaporation hence actual water uptake is not steady. For critical processes within the membrane, water uptake is the relevant variable influencing transport and chemical properties, while RH only affects surface properties and, variably, the amount of water uptake. Furthermore, the water uptake-humidity relationship is not the same for different membranes. According to our observations, the same membrane that is subjected to different thermal treatments will uptake water differently at a given humidity. We note that the quadrupole splitting, and indeed relevant transport parameters such as the diffusion constant and proton conductivity, strongly depend on the water uptake. An unsteady water uptake level will lead to inconsistent NMR quadrupole splitting as well as water self-diffusion results discussed in the second part of this paper, which makes quantitative analysis difficult. In this work for both the $^2$H NMR and the water self-diffusion studies, we use sealed and equilibrated low-dead-volume sample cells that provide exquisitely reproducible and quantifiable results. In addition, we take advantage of the quantitative nature of NMR

measurements to verify the water uptake through comparison of NMR signal intensity with gravimetric data. In our initial study,[4] we found uniform order in two commercial Nafion membranes using our simple and quantitative $^2$H NMR method. In this paper, we present detailed orientational order measurements and water transport properties (self-diffusion) in three leading Nafion membranes. We demonstrate that this channel alignment is uniform over these films but has drastically different properties for different membrane types. We report the dependencies of $^2$H quadrupole splitting on $D_2O$ uptake and temperature, confirming that thermal swelling of these membranes is rigorously affine. Quantifying this order allows for feedback on anisotropic conductivity in these ionomer membranes.

### 3.2.3 Diffusion Anisotropy in Ionomer Membranes

The transport properties of water and ions in Nafion are commonly measured by pulsed-field-gradient (PFG) NMR self-diffusion experiments.[21,22] Saito *et al.* suggested[17] that protons in the membranes transport by the Grotthuss hopping mechanism[23] and the larger ions ($Li^+$, $Na^+$ etc.) by the vehicle mechanism.[24] Zhang *et al.* studied tortuous self-diffusion behavior of commercial and recast Nafion[25] and observed a dependence of apparent diffusion coefficient over a range of diffusion times, attributing this to the water interaction with the ionic clusters. This measurement provides intrinsic information on the translational motion of water molecules and free or hydrated protons/ions in the membranes. Compared to conductivity measurements, which report both isotropic[2,3,27,28] or anisotropic[2,3] conductivity in Nafion, an as yet unsettled topic in literature, the PFG-NMR self-diffusion measurement is a non-contact technique that eliminates the complication and variation of electrode interfaces and does not require complex mathematical models to convert and compare in-plane vs. through-plane conductivity. For isotropic systems, the diffusion coefficient measured in the PFG direction represents the overall

3-dimensional diffusion behavior. For anisotropic systems, the diffusion coefficient obtained will depend on the relative orientation of the material with respect to the NMR field gradient direction. Fechete *et al.*[26] detected small diffusion anisotropy of toluene in uniaxially compressed natural rubber samples using NMR self-diffusion. Rollet *et al.*[27] used radio tracer and NMR techniques to demonstrate transport anisotropy of ions in sulfonated polyimide ionomer membranes where a faster in-plane over through-plane diffusion was observed. We apply the PFG diffusion method to describe the transport anisotropy in three commercial Nafion types by placing the $H_2O$ swollen membrane at three orthogonal directions with respect to the PFG direction in order to correlate morphological orientation and transport properties. Our diffusion anisotropy results correlate well with our orientational order measurements, providing a link between channel ordering and molecular transport.

## 3.3 Materials and Methods

### 3.3.1 Materials

Nafion 112 and Nafion 117 (extruded) and Nafion NRE212 (dispersion-cast) membranes, all nominally 1100 equivalent weight (EW) per sulfonate group, were obtained from E.I. DuPont (Wilmington, DE) in acid form. The membrane thickness and processing method are listed in Table 3.1. Deuterium oxide was obtained from Cambridge Isotope Laboratories, Inc. (Andover, MA) at 99.9 % purity. Membranes and solvents were used as received.

**Table 3.1. Nafion membrane types investigated.**

| Nafion Type | Membrane Thickness (mm) | Processing Method |
|---|---|---|
| N112 | 50 | Extruded |
| NRE212 | 50 | Dispersion cast |
| N117 | 175 | Extruded |

### 3.3.2 Orientational Order Measurements

All NMR experiments were performed on a Bruker Avance III WB NMR spectrometer (Bruker-Biospin, Billerica, MA) at a magnetic field of 9.4 T, corresponding to a $^{1}H$ frequency of 400 MHz and a $^{2}H$ frequency of 61.4 MHz. A single channel detection static solids probe with a 10.7 mm inside diameter horizontal solenoid coil was used for $^{2}H$ spectroscopy experiments.

Extruded Nafion membranes were cut into 6 × 6 mm pieces with one edge along the extrusion striate. The orientation was confirmed by polarizing microscopy (Meiji Technology MX9430, Japan). Dispersion-cast Nafion membranes were cut into the same size with an orientation relative to the film sheet edges. Ten pieces were stacked in exactly the same orientation to enhance NMR signal. The stacks of dry membranes were placed in a 40 °C oven for 5 h, weighed, then loosely wrapped with Teflon pipe seal tape and soaked in $D_2O$ for at least one week. The maximum $D_2O$ uptakes, expressed in wt %, were measured by the weight gain versus the weight of the dry membranes. The wt % of unsaturated membranes was measured by the partially swollen membrane weight and confirmed with relative NMR signal intensity. Error in this uptake wt % is ± 10 % of the absolute water uptake, *e.g.*, at 20 wt % uptake the error is ± 2 wt %, and at 5 wt % the error is ± 0.5 wt %. The NMR probe was tuned and matched to ensure the shortest 90° pulse time. Before NMR experiments, the membrane stacks were wrapped with Teflon tape and LDPE plastic wrap and sealed in a Delrin sample cell as shown in fig. 3.1, followed by equilibration for 3 h before taking measurements. The sample cell can be rotated in the NMR coil casing, using a goniometer to accurately adjust orientation of the sample cell to ± 1.5° accuracy.

$^{2}H$ NMR experiments utilized a simple free induction decay (FID) acquisition following a single pulse of 4 μs ($\pi/2$ pulse = 6 μs) and a repetition time of 0.7 s for 256 or 1024 scans. The

deuterium quadrupole splittings were extracted from the data by fitting each spectrum with two Lorentzian peaks using NutsPro software (Acorn NMR Inc., Livermore, CA). A calibration curve of splitting versus wt % was established for each sample by running consecutive NMR experiments with the sample cell cap partially removed, allowing $D_2O$ to slowly evaporate from the membranes over a period of 2 - 3 days. Peak areas, along with gravimetric calibration data, were used to calculate wt % of actual $D_2O$ in membranes as a function of time. Angle between the membrane sample cell and the static magnetic field was varied in 15° steps from 0° to 90°. At room temperature, $T_1$ values are 200 ms for saturated membranes and 40 ms for nearly dry membranes.

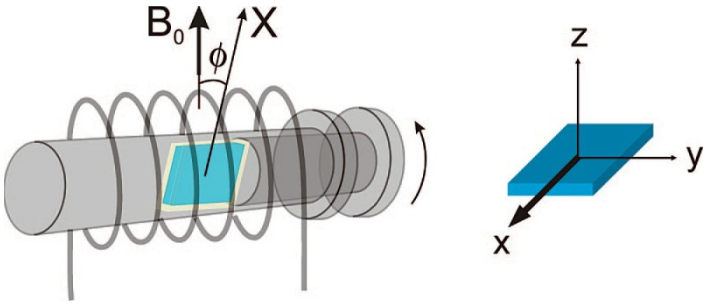


**Figure 3.1. Schematic diagram of the sample cell and definition of membrane directions.** The sample cell contains a slit for the membrane stack (blue block) and a pressure fit piston cap to seal the container and allow the sample to equilibrate with very low dead volume (< 20 %). The three axes in the rectangular blue block indicate three membrane principal directions, where the membrane **z**-axis is perpendicular to the plane. For the extruded membranes, **x** is the extrusion direction as indicated by the thicker arrow. For the dispersion cast membrane, **x** is an arbitary in-plane direction. **y** is in the membrane plane perpendicular to **x**. The entire cylindrical cell is rotated inside the solenoid rf coil, and thus the angle $\phi$ between membrane in-plane direction **x** axis and the magnetic field can be varied.

### 3.3.3 Diffusion Coefficient Measurements

Self-diffusion coefficients of water ($^1H_2O$) in membranes were measured using the 400 MHz Bruker Avance III WB NMR equipped with a single axis diffusion probe having a maximum gradient of 2982 G/cm. Pulsed-gradient stimulated echo (PGSTE) experiments were performed at 25 °C. Temperature was calibrated using 100 % ethylene glycol standard to an

accuracy of 0.2 °C. The gradient constant was calibrated by measuring the diffusion coefficient of 1 % $H_2O/D_2O$ doped with 0.1 mg/mL $GdCl_3$ to a literature value of 1.872 x $10^{-9}$ $m^2/s$ at 25 °C.

The free diffusion NMR signal attenuation is described by the following equation:[28]

$$I = I_0 e^{-D\gamma^2 g^2 \delta^2 (\Delta - \delta/3)} = I_0 e^{-Db} \tag{3.2}$$

where $I$ is the spin-echo signal intensity, $I_0$ is the signal intensity at zero gradient, $\gamma$ is the gyromagnetic ratio of the probe nucleus (rad $s^{-1}$ $T^{-1}$), $\delta$ (s) is the duration of the field gradient pulse with magnitude $g$ (T $m^{-1}$), $D$ is the self-diffusion coefficient of water in the membranes, and $\Delta$ is the duration between the leading edges of the two gradient pulses. $b$ is commonly known as the Stejskal-Tanner parameter[31] in clinical literature and also sometimes has the label $Q$. The signal intensity $I$ is measured as a function of $g$ to deduce the diffusion coefficient of water in the membranes. For each experiment, a range of $\Delta$ values were used to evaluate the diffusion coefficients. In order to measure diffusion anisotropy, membrane samples were trimmed the same way as for the $^2H$ NMR experiment, soaked in $H_2O$ for more than 48 h, and water uptake measured by gravimetry after blotting the membrane to remove free water. For in-plane diffusion, the sample stacks were loaded into a sample cell similar to fig. 3.1, that is made of Teflon and can fit vertically into an 8 mm double resonance saddle-shape RF coil. For through-plane diffusion, another Teflon cell comprised of a cylindrical cavity (6.5 mm i.d., 8 mm o.d.) and a piston cap was used. In the latter cell, the same sample can be placed in the center of the 8 mm RF coil with spectrometer magnetic field $\mathbf{B_0}$ direction normal to the membrane surface. An equilibration time of 3 h in the sealed sample cell was allowed prior to diffusion measurements, based on a measured 1 - 2 h time to reach steady state when measuring $^2H$ spectra and diffusion constants. In terms of reproducibility among different experiments, allowing for uptake errors and using careful calibrations with known standards, we estimate an absolute

accuracy of $D = \pm 3$ %. However, within a certain group of diffusion anisotropy experiments (as in for one membrane at different angles as in figs. 3.7 and 3.8) we estimate a tighter accuracy of $D = \pm 2$ %.

### 3.4 Results and Discussion

#### 3.4.1 Orientational Order, Affine Swelling, and Morphological Models

Figure 3.2A shows NMR spectra as a function of N112 membrane angle $\phi$ with respect to $\mathbf{B_0}$, rotating about the membrane **y**-axis. Here, the membrane **x**-axis corresponds to the principal alignment direction, or "director," as it is the direction where maximum splitting occurred, so $\phi$ becomes $\theta$ in eqns. 3.1 and 3.3 for N112. Because of the membrane biaxiality, and in an extension of eqn. 3.1, the quadrupole splitting follows a dependence given by[14,16,29,30]

$$\Delta\nu_Q = \frac{1}{2}\Delta\nu_0[3\cos^2\theta - 1 + \eta\sin^2\theta] \tag{3.3}$$

which we may use to fit splittings as a function of angle and wt % $D_2O$ uptake, shown in fig. 3.2B. Here we note that the biaxiality parameter $\eta = 0.12 \pm 0.02$ is stable over hydration levels of 6 - 13 wt %, indicating that the degree and symmetries of alignment in these channels are stable vs. hydration level. Further experiments using only the three **x**, **y**, and **z** directions of sample orientation[4] showed that this $\eta = 0.12$ is stable over at least a hydration level range of 4 - 20 wt %. Similar analyses for Nafion NRE212 are shown in fig. 3.2C, D. In these figures, the angle $\phi$ is defined as the angle between an (arbitrary) in-plane membrane direction **x** and the magnetic field direction $\mathbf{B_0}$. In this case, one can immediately notice from the rotation pattern that the principle alignment direction (director) is perpendicular to the membrane in-plane **x** axis, *i.e.*, in the through-plane **z** axis direction. Therefore, the angle $\theta$ of eqn. 3.3 becomes 90° - $\phi$.

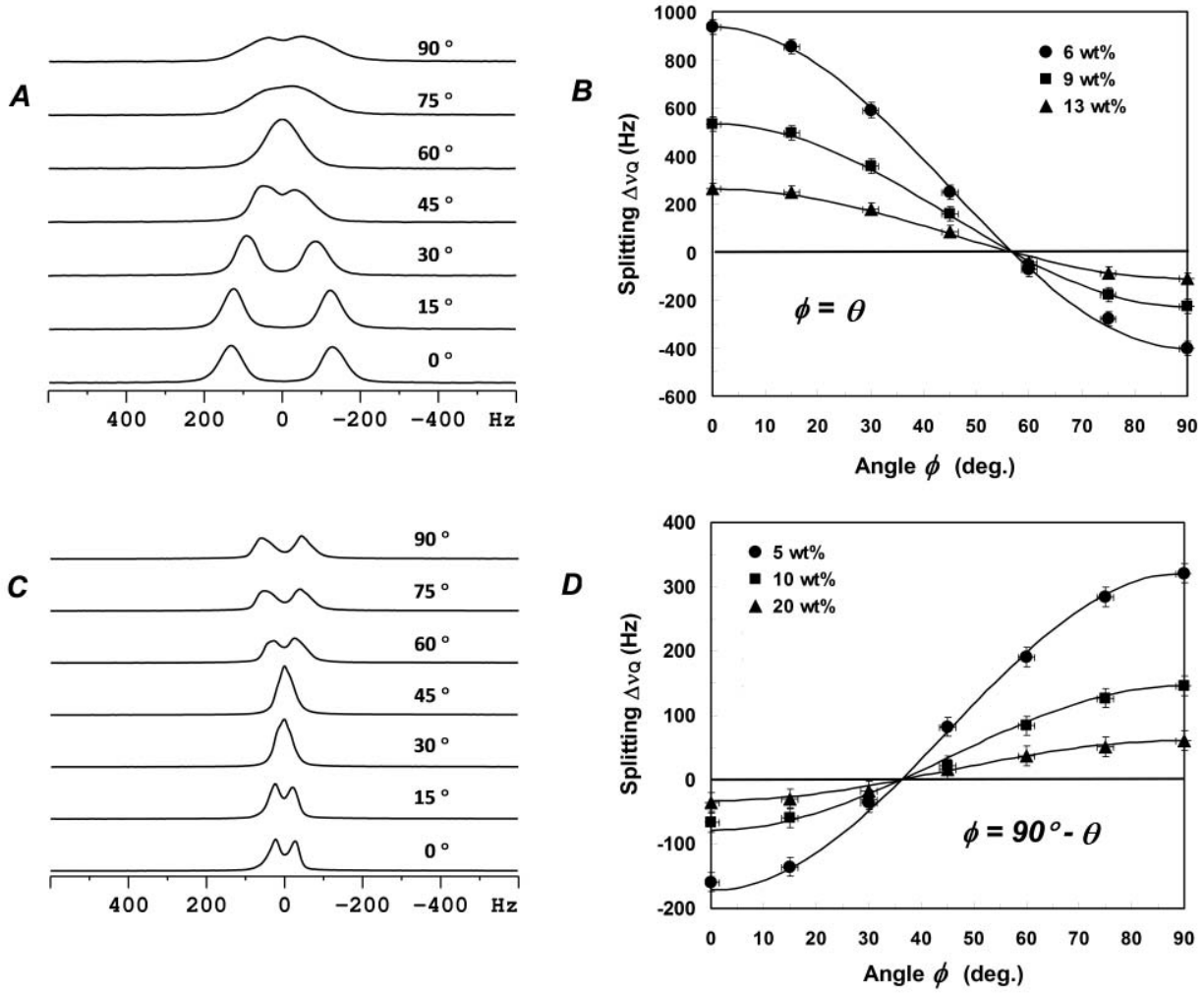


**Figure 3.2.** **$^2$H NMR spectra versus rotation angle** for N112 (A) and NRE212 (C) with 13 wt % $D_2O$. (B) Plots of quadrupole splitting $\Delta\nu_Q$ vs angle $\phi$ of the extrusion direction relative to the spectrometer field $\mathbf{B_0}$ over a range of $D_2O$ uptake in N112. Solid lines are fitted curves using eqn 3.3, where $\theta = \phi$, and $\eta = 0.12 \pm 0.02$ provides best fits for all curves and is the only adjustable fit parameter after specifying $\Delta\nu_0$, the spectral splitting at $\phi = 0$. (D) Plots of quadrupole splitting $\Delta\nu_Q$ vs angle $\phi$ of the **x** (in-plane) direction relative to the spectrometer field $\mathbf{B_0}$ over a range of $D_2O$ uptake in NRE212. Solid lines are fitted curves using eqn 3.3, where $\theta = 90° - \phi$, and $\eta = 0$ provides best fits for all curves and is the only adjustable fit parameter after specifying $\Delta\nu_0$, the spectral splitting at $\phi = 90$. The error estimate for $\eta$ based on all our data fits is ± 0.02.

Figure 3.2D shows that dispersion-cast NRE212 exhibits uniaxial order ($\eta = 0$) over hydration levels of 5 - 20 wt %. Both results in fig. 3.2B, D clearly indicate affine swelling in these two Nafion membranes. We observe in fig. 3.2 that the zero $\Delta\nu_Q$ crossover angle $\theta_{\Delta\nu Q} = 0$ is equal to

the magic angle 54.7º since $\eta = 0$ for NRE212, while $\theta_{\Delta\nu_Q} = 0$ for N112 is 56.4º, larger than the magic angle due to the biaxiality $\eta = 0.12$. This provides an additional indication of biaxiality for N112. Furthermore, by comparing the quadrupole splittings of the two membranes at the same hydration level as shown in fig. 3.2A, C, one finds that the quadrupole splitting and thus the orientational order parameter ***S*** is 2.5 times larger in N112 than in NRE212. Thus, this morphological alignment, in the through-plane direction, shows substantial room for improvement over as-received NRE212, which would be highly desirable for operating fuel cells and other ionomer-based devices that depend on maximizing through-plane conductivity.

On the basis of the methods of our previous work,[4] we examined the $^2$H NMR quadrupole splitting of extruded N117 at three orthogonal angles as shown in fig. 3.3. This provides adequate orientational information for up to second degree order (biaxial) by using $\eta = |\Delta\nu_Q^y - \Delta\nu_Q^z|/\Delta\nu_Q^x$. Figure 3.3 shows that order in N117 is uniaxial ($\eta = 0$) and along the extrusion direction to within experimental errors. The error in $\eta = \pm 0.04$ in this case is due to fitting errors of these spectra. We observe that the quadrupole splitting is dramatically smaller for N117 at 7 wt % (144 Hz) compared to N112 (936 Hz) at a similar uptake (6 wt %) as shown in fig. 3.2A. Both biaxial and uniaxial orders can sensibly arise from

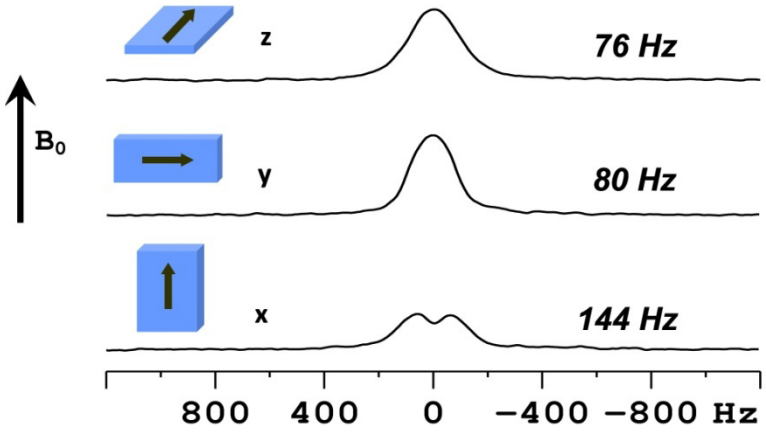


**Figure 3.3. Room temperature $^2$H NMR spectra for N117** at 7 wt % $D_2O$ uptake. The rectangular blocks in blue indicate different membrane directions (**x, y, z**) lying parallel to the spectrometer $\mathbf{B_0}$ field. The arrows indicate the extrusion direction. The quadrupole splitting values $\Delta\nu_Q$ at right result from nonlinear least-squares fits to each spectrum.

the extrusion processes inducing mechanical stress on the membranes. The smaller order in N117 likely results from the substantially smaller shear and extensional forces imparted on the much thicker N117 membrane (175 μm) relative to the N112 membrane (50 μm). We also find that for a given membrane, the quadrupole splitting increases as the membrane $D_2O$ uptake decreases as shown in fig. 3.2. This results from a stronger "pseudonematic interaction"[16] as average channel size is smaller (surface-to-volume ratio is larger) at low uptake, and $D_2O$ molecules will experience more anisotropic interactions with the channel walls than with other $D_2O$ molecules. In other words, the scaling factor $\rho$ in eqn. 3.1 is larger at low $D_2O$ probe molecule uptake. This dependence necessitates fine control of $D_2O$ uptake when conducting these experiments. It also explains the lack of systematic splitting reported in previous studies,[10-12] most likely due to larger dead volume or temperature spreads over the sample cell and thus less control over water uptake.

Figure 3.4 depicts models for the channel morphologies in these membranes. In order to emphasize the alignment quality, these models are simplified descriptions of Nafion morphology, which could consist of interconnected channels, lamella, and clusters in three dimensions.[5] Recent work by Schmidt-Rohr and Chen strongly indicates randomly packed parallel cylindrical hydrophilic channels (diameter ~ 2.4 nm at 20 vol % $H_2O$).[10] Another study by Rollet *et al.* indicates cylindrically symmetric fibrillar bundles with similar ~ 2 nm diameter and a persistence length of ~ 100 nm.[8] Both of these models assert essentially well-defined walls and allow high water permeability. In all cases, the channels are strongly interconnected resulting in water percolation as shown by water self-diffusion results in section 3.4.2 of this chapter. Parts A and B show two possible biaxial morphologies, consistent with our data, for the extruded N112 channel morphology. Part A depicts biaxial (elliptical) channels aligned

uniaxially along the extrusion direction, while B depicts uniaxial (cylindrical) channels aligned biaxially via larger local bends in-plane vs through-plane. Distinguishing between parts A and B requires further structural studies, *e.g.,* microscopy and XRD with suitable modeling,[7,9] or further NMR diffusometry or relaxometry techniques we are exploring. A direct observation with electron microscopy on the nanometer scale features in water-swollen membranes is extremely challenging if not impossible. At present, we are working toward a model to reveal the relationship between probe molecule quadrupole splitting and channel order parameter $\boldsymbol{S}_{\text{matrix}}$ (see eqn. 3.1) by taking into account the shape and area of the channel cross section. Such a model could potentially resolve the difference between morphology A and B, and would provide independent measures of $\rho$ and $\boldsymbol{S}_{\text{matrix}}$. Part C shows the morphology model for extruded N117, in which the hydrophilic channels have cylindrical shape and uniaxially align in the extrusion direction with minimal biaxiality. Part D shows the dispersion-cast NRE212 channel morphology, consisting of cylindrical channels aligned

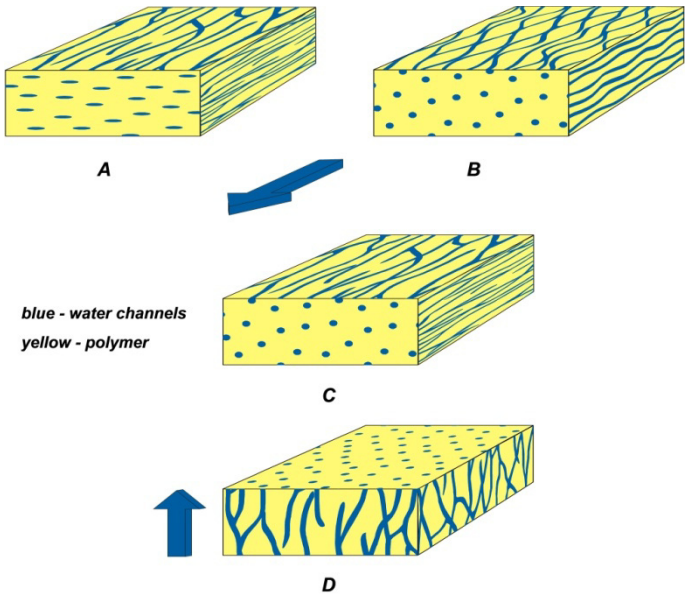


**Figure 3.4. Proposed hydrophilic channel alignment models** for N112 (A and B), N117 (C) and NRE212 membranes (D). A, Biaxiality caused by ellipsoidal channels aligned along the extrusion direction (block arrow) in the membrane plane. B, Biaxiality caused by cylindrical channels with directional anisotropy in the membrane plane relative to across the plane (zigzag character in film plane and perpendicular to extrusion direction). C, Uniaxially aligned cylindrical channels in the membrane plane along the extrusion direction. D, Uniaxially aligned cylindrical channels perpendicular to the membrane plane (block arrow). Arrow also indicates solvent evaporation gradient direction.

uniaxially across the plane of the film. This could include weak ordering (tilting) of bundles[8] through-plane with bundle long axis directions randomized in the plane. This through-plane alignment is likely formed during the casting process by solvent evaporating (flowing) in the direction normal to the membrane plane. The supporting substrate for the dispersion casting process may also induce order in the final membrane formed, as is commonly seen in liquid crystal surface alignment techniques.[31] Note that these models and our observations do not specify whether Nafion exhibits a cluster-network model[5] or quasi-cylindrical channel models,[6,7] but do support cylindrical (biaxial for N112) alignment symmetry.

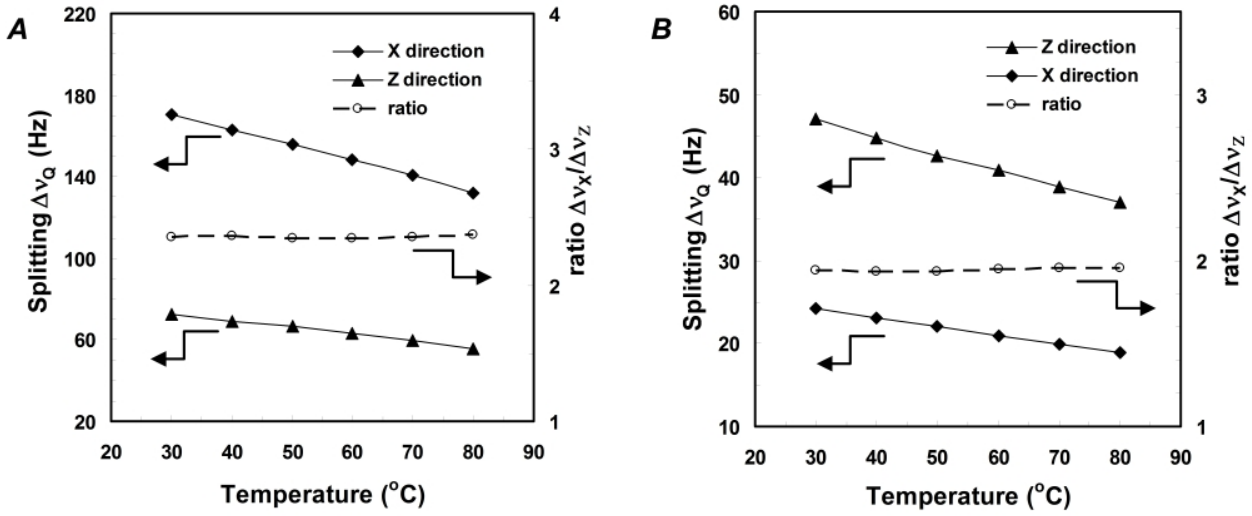


**Figure 3.5. Quadrupole splittings $\Delta\nu_Q$ vs temperature** at 20 wt % $D_2O$ uptake for N112 (A) and NRE212 (B) in two reference directions as defined in Fig. 3.1. Solid symbols represent $\Delta\nu_Q$ measurements, while open circles and dotted lines represent the ratios between splittings at these two directions.

Parts A and B of fig. 3.5 summarize the temperature-dependent $^2H$ quadrupole splitting for N112 and NRE212 at 20 wt % $D_2O$ uptake, respectively. First we notice that the splittings decrease as temperature increases, which can be explained by the thermal expansion of the hydrophilic channels that leads to a weaker "pseudonematic interaction"[16] between the $D_2O$ molecule and the channel walls and hence a smaller ensemble average ***S*** in eqn. 3.1 and smaller

quadrupole splitting. The other obvious observation is that the ratios between the splitting at two reference angles are steady in temperature ranging from 25 to 80 °C, indicating the biaxiality/uniaxiality in respective systems does not change upon heating, *i.e.*, the thermal expansion of the two membranes are affine. We note that in our first experiments using poorly sealed sample cells (a capped 18 cm long 10 mm NMR tube with membrane held up by half cylindrical Teflon spacers), we observed nearly flat but slightly increasing splittings with temperature. In view of our fig. 3.6 results, this was undoubtedly due to water evaporation during heating and subsequent condensation into the membrane upon cooling.

To evaluate and compare alignment in various membranes, we generated curves of quadrupole splitting vs $D_2O$ uptake for the three membranes in fig. 3.6. A comparison between splitting at similar $D_2O$ uptakes reveals the relative degree of alignment. N112 exhibits the highest order among these membranes. In addition, this reproducible relationship enables one to conveniently characterize water uptake using the quadrupole splitting for a given membrane, once the splitting-uptake curve is established. As mentioned above, we are investigating models of quadrupole splitting vs water uptake and channel order, which in this case might allow for extraction of the water channel cross section dependence as a function of water uptake.

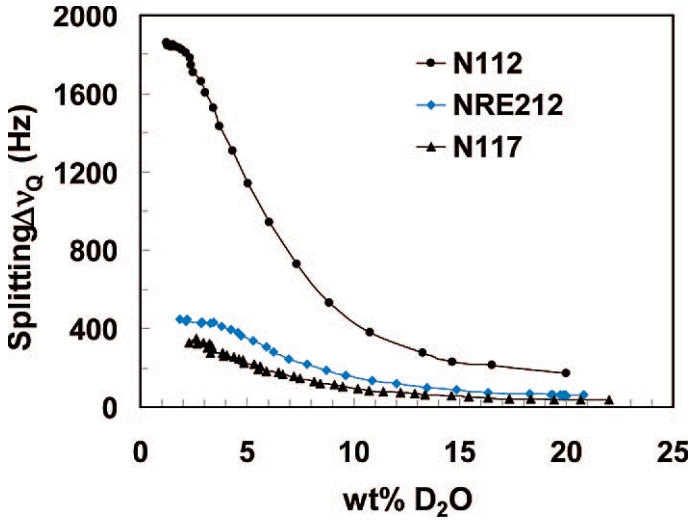


**Figure 3.6. Plots of quadrupole splittings $\Delta\nu_Q$ vs $D_2O$ uptake** for N112 (black circles), NRE212 (blue diamonds), and N117 (black triangles) with their maximum alignment direction (splitting maximum) parallel to the magnetic field $\mathbf{B_0}$. These curves allow for direct comparison of order in different membranes and provide another method of measuring water uptake using $\Delta\nu_Q$.

### 3.4.2 Diffusion Anisotropy

The NMR stimulated echo signal decay $I/I_0$ is a function of $\boldsymbol{b}$ ($= \gamma^2 g^2 \delta^2 (\Delta - \delta/3)$), with dependence shown in fig. 3.7. We obtain self-diffusion coefficients $D$ from the slopes of the fitted lines. It is evident that the slopes and therefore the diffusion coefficients for the same water-swollen N112 are different in through-plane ($D_{zz}$) and in-plane ($D_{xx}$, $D_{yy}$ close in numerical value to $D_{zz}$ not shown) directions. In fig. 3.8 we plot the water self-diffusion coefficients for water-swollen N112, NRE212, and N117 in three orthogonal directions. The gradient is parallel to $\mathbf{B_0}$, thus we can use the same axis definitions **x, y, z** to indicate the diffusion direction with respect to the membrane orientation in the NMR coil. We varied diffusion time Δ from 7 to 50 ms to look for any morphological barriers that may cause tortuous diffusion[25] behavior. In all membranes, directions, temperatures, and water uptakes, the measured $D$ values were stable over that range of diffusion times. A study of diffusion with smaller diffusion times Δ is underway to investigate morphological barriers (*e.g.,* domain structure) on the ~ 1 μm scale. Figure 3.8

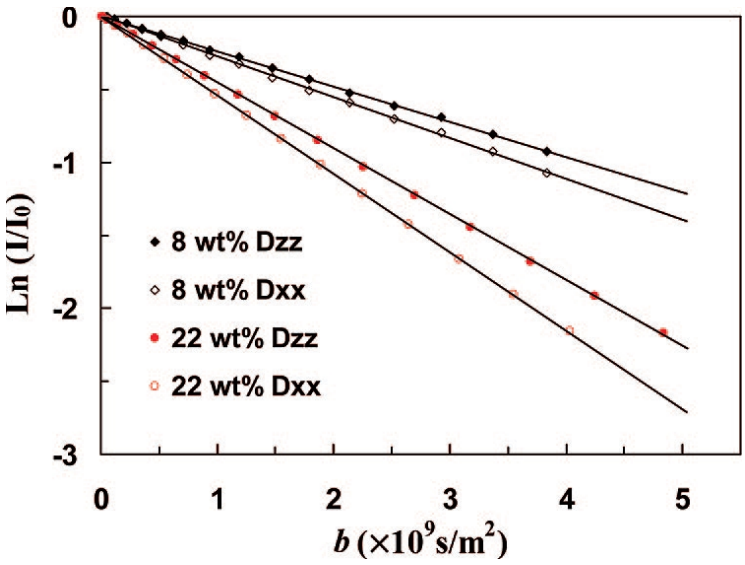


**Figure 3.7. Normalized signal amplitudes ($I/I_0$)** of stimulated echo decays vs Stejskal-Tanner parameter $b$ for N112 with 8 and 22 wt % $H_2O$ for a diffusion time Δ = 20 ms at 25 ºC. Solid symbols indicate signal decay for through-plane diffusion in the **z** direction $D_{zz}$. Open symbols indicate signal decay for in-plane diffusion in the **x** direction $D_{xx}$. Error bars are comparable to the data symbol size. The solid lines are linear least-squares one-component fits with correlation coefficients larger than 0.999.

shows the average values for each case. These values are listed in Table 3.2 for easy comparison with orientational order measurements.

Clearly the self-diffusion of water in N112 at 22 wt % $H_2O$ uptake in the extrusion direction (5.48 x $10^{-10}$ $m^2/s$) is 14 % faster than in the perpendicular in-plane direction (4.81 x $10^{-10}$ $m^2/s$) and 18 % faster than that in the through-plane direction (4.64 x $10^{-10}$ $m^2/s$). This indicates that the energy barrier for water transport is lower in the direction in which the hydrophilic channels are aligned,[2,3,32] and provides a substantial yet qualitative correlation with the above $^2H$ spectroscopic alignment measurements. At a lower water uptake of 8 wt %, the diffusion coefficients are smaller ($D_{xx}$ = 2.88 × $10^{-10}$, $D_{yy}$ = 2.47 × $10^{-10}$, $D_{zz}$ = 2.44 × $10^{-10}$ $m^2/s$), but the ratio of $D_{xx}/D_{zz}$ remains equal to 1.18, indicating the diffusion anisotropy is stable over a range of water uptake for a given membrane. The results for NRE212 and N117 show nearly isotropic diffusion behavior, *i.e.*, diffusion coefficients are equal in all three directions within experimental error. This is probably due to the low degree of ordering in these two membranes. Though the alignment is discernible by $^2H$ NMR splitting, it is not high enough to lead to diffusion anisotropy. The small yet not quite significant differences for N117 and the biaxial

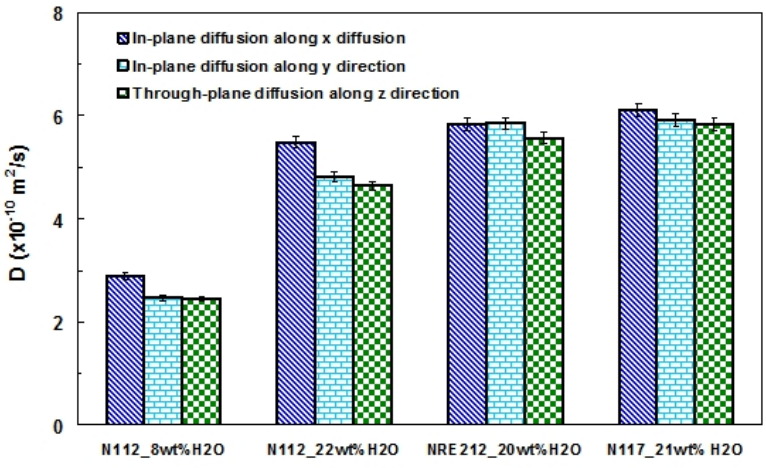


**Figure 3.8. Water self-diffusion coefficients *D*** at 25 °C measured by placing the water-swollen membranes at three angles with respect to the gradient direction. *D* values are averaged over a diffusion time Δ ranging from 7 to 50 ms. Error bars of ± 2 % indicate the accuracy of *D* measurements with respect to anisotropy (within each membrane group).

N112 do follow the spectroscopic order measurements, while in NRE212, the small differences are at odds with the order measurements. We note that *D* in the extrusion direction of N112

**Table 3.2.** **$^2$H NMR quadrupole splittings and diffusion coefficients** in three membrane directions for various Nafion types.

| **$D_2O$/Nafion quadrupole splitting** | **$\Delta\nu_Q^x$ (Hz)** | **$\Delta\nu_Q^y$ (Hz)** | **$\Delta\nu_Q^z$ (Hz)** |
|---|---|---|---|
| N112 at 6 wt % | 936 | -528 | -401 |
| NRE212 at 5 wt % | -159 | -162 | 321 |
| N117 at 7 wt % | 144 | -80 | -76 |
| **$H_2O$/Nafion self-diffusion** | **$D_{xx}$ (x $10^{-10}$ $m^2/s$)** | **$D_{yy}$ (x $10^{-10}$ $m^2/s$)** | **$D_{zz}$ (x $10^{-10}$ $m^2/s$)** |
| N112 at 8 wt % | 2.88 | 2.47 | 2.44 |
| N112 at 22 wt % | 5.48 | 4.81 | 4.64 |
| NRE212 at 20 wt % | 5.83 | 5.86 | 5.58 |
| N117 at 21 wt % | 6.11 | 5.92 | 5.84 |

approximates *D* for any direction in NRE212, while *D*'s in the other two directions are slower than NRE212, giving the impression that diffusion is attenuated in the other two directions by the extrusion process. We believe that instead the overall channel connectivity (see below) of the NRE212 and N117 materials are higher than that for N112, since they are processed and presumably chemically and thermally treated in different ways.

In addition to orientational order, the *connectivity* of the channels will also influence diffusion anisotropy as well as the magnitude of diffusion. For an average hydrophilic channel length, determined to be ~ 100 nm in XRD studies,[7,10] the water transport will certainly depend on how well the channels are interconnected. If an aligned morphology has more dead ends, then it will exhibit slower diffusion for water molecules along that direction. This may partially

cancel out some of the diffusion enhancement effects induced by bulk alignment, which may be the case for NRE212. A morphological model possible for cast membranes such as NRE212 consists of long cylindrical channel bundles that are randomly oriented in-plane but have an average tilt angle toward the through-plane direction. This morphology would show average through-plane order, whereas the diffusion anisotropy will depend on the degree of the tilting. Through-plane diffusion would be faster or slower than that of in-plane due to extend of alignment (bundle tilt). A recent publication by Kidena showed diffusion anisotropy results for water in Nafion NRE-212CS and hydrocarbon ionomer membranes.[35] The author observed negligible diffusion anisotropy for NRE-212CS at room temperature, which is consistent with this study.

Note that we have thus far used the membranes "as is" without any attempt to induce order. We anticipate when the order is enhanced in a particular direction, the diffusion and proton conductivity in that direction should increase as well. We are beginning systematic spectroscopy and diffusion studies of membranes with enhanced alignment via various processes. For most fuel cell applications, high through-plane proton conductivity is desired, and our measurements point toward the need for increasing through-plane alignment and thus conductivity. However, Gruber *et al.* recently developed a lateral fuel cell[33] in which protons transport tangentially in the membrane plane. Such devices would benefit from higher in-plane proton conductivity, which is more easily achieved. Reports show that high temperature annealing of extruded films produces increased fuel cell performance,[18,34] which might be explained due to randomization of alignment in these films, producing better through-plane conductivity than unannealed N112 films aligned in-plane. Furthermore, aging of membranes in operating fuel cells, which usually requires hours or days of operation before becoming stable,[18]

could result from the evolution of flow alignment of the hydrophilic channels. These methods allow characterization of membrane order and diffusion properties of membrane ionomers before, after, or during device operation.

### 3.5 Concluding Remarks

We quantitatively measure bulk channel alignment in Nafion membranes using $^2$H NMR directly on residually aligned absorbed $D_2O$. The numerical quantification of anisotropy properties such as the biaxiality parameter is straightforward using this method. We present results for three perfluorosulfonate ionomer membranes showing that the hydrophilic channels are biaxially oriented ($\eta = 0.12$) for extruded N112 membranes and uniaxially oriented for N117, both in the extrusion direction, whereas channels are uniaxially oriented perpendicular to the plane for dispersion-cast NRE212. These results indicate that water swelling (4 - 20 wt %) and thermal expansion (25 - 80 °C) for these membranes are affine, at least on the ~ 1 μm scale probed here by the $^2$H quadrupole interaction. Water self-diffusion measurements demonstrate anisotropic transport in N112 with an in-plane diffusion coefficient 18 % larger than that of through-plane at two hydration levels, while the anisotropic effect is minimal for N117 and NRE212 due to lower order present in the latter two membranes.

This study represents the first direct comparison of a directional transport property (diffusion) with quantitative orientational order measurements for ionomer membranes. We are expanding these studies to include other membrane chemistries and morphologies in order to obtain a more complete picture of membrane transport and thus optimally design membranes for targeted applications. We propose that control over the direction and extent of orientational order of the hydrophilic channels will allow increased material design freedom and

improvements in ionomer device performance, *e.g.*, increased proton conductivity across the membrane plane in fuel cells.

**References**


(1) Mauritz, K. A.; Moore, R. B. *Chemical Reviews* **2004**, *104*, 4535-4585.

(2) Ma, S.; Siroma, Z.; Tanaka, H. *Journal of the Electrochemical Society* **2006**, *153*, A2274-A2281.

(3) Cable, K. M.; Maurtiz, K. A.; Moore, R. B. *Chemistry of Materials* **1995**, *7*, 1601-1603.

(4) Li, J.; Wilmsmeyer, K. G.; Madsen, L. A. *Macromolecules* **2008**, *41*, 4555-4557.

(5) Gierke, T. D.; Munn, G. E.; Wilson, F. C. *Journal of Polymer Science Part B-Polymer Physics* **1981**, *19*, 1687-1704.

(6) Rubatat, L.; Gebel, G.; Diat, O. *Macromolecules* **2004**, *37*, 7772-7783.

(7) Schmidt-Rohr, K.; Chen, Q. *Nature Materials* **2008**, *7*, 75-83.

(8) Elliott, J. A.; Hanna, S.; Elliott, A. M. S.; Cooley, G. E. *Macromolecules* **2000**, *33*, 4161-4171.

(9) Elliott, J. A.; Paddison, S. J. *Physical Chemistry Chemical Physics* **2007**, *9*, 2602-2618.

(10) Chen, R. S.; Jayakody, J. P.; Greenbaum, S. G.; Pak, Y. S.; Xu, G.; McLin, M. G.; Fontanella, J. J. *Journal of the Electrochemical Society* **1993**, *140*, 889-895.

(11) Rankothge, M.; Haryadi; Moran, G.; Hook, J.; Vangorkom, L. *Solid State Ionics* **1994**, *67*, 241-248.

(12) Xu, G.; Pak, Y. S. *Solid State Ionics* **1992**, *50*, 339-343.

(13) McLean, R. S.; Doyle, M.; Sauer, B. B. *Macromolecules* **2000**, *33*, 6541-6550.

(14) Burnell, E. E.; De Lange, C. A. *NMR of ordered Liquids*; Kluwer:Dordrecht, 2003.

(15) Deloche, B.; Samulski, E. T. *Bulletin of the American Physical Society* **1981**, *26*, 327-328.

(16) Callaghan, P. T.; Samulski, E. T. *Macromolecules* **2003**, *36*, 724-735.

(17) Yu, L. J.; Saupe, A. *Physical Review Letters* **1980**, *45*, 1000-1003.

(18) Zhao, T. S.; Kreuer, K.-D.; Nguyen, T. V. *Advances in fuel cells*; Elsevier, 2007; Vol. 1.

(19) Lee, J. H.; Nam, J. D.; Choi, H.; Jung, K.; Jeon, J. W.; Lee, Y. K.; Kim, K. J.; Tak, Y. *Sensors and Actuators a-Physical* **2005**, *118*, 98-106.

(20) Shoji, E.; Hirayama, D. *Journal of Physical Chemistry B* **2007**, *111*, 11915-11920.

(21) Zawodzinski, T. A.; Neeman, M.; Sillerud, L. O.; Gottesfeld, S. *Journal of Physical Chemistry* **1991**, *95*, 6040-6044.

(22) Saito, M.; Arimura, N.; Hayamizu, K.; Okada, T. *Journal of Physical Chemistry B* **2004**,

*108*, 16064-16070.

(23) Thampan, T.; Malhotra, S.; Tang, H.; Datta, R. *Journal of the Electrochemical Society* **2000**, *147*, 3242-3250.

(24) Paddison, S. J.; Paul, R.; Zawodzinski, T. A. *Journal of the Electrochemical Society* **2000**, *147*, 617-626.

(25) Zhang, J. H.; Giotto, M. V.; Wen, W. Y.; Jones, A. A. *Journal of Membrane Science* **2006**, *269*, 118-125.

(26) Fechete, R.; Demco, D. E.; Blumich, B. *Macromolecules* **2003**, *36*, 7155-7157.

(27) Rollet, A. L.; Diat, O.; Gebel, G. *Journal of Physical Chemistry B* **2004**, *108*, 1130-1136.

(28) Stejskal, E. O.; Tanner, J. E. *Journal of Chemical Physics* **1965**, *42*, 288-292.

(29) Madsen, L. A.; Dingemans, T. J.; Nakata, M.; Samulski, E. T. *Physical Review Letters* **2004**, *92*, 145505.

(30) Severing, K.; Saalwachter, K. *Physical Review Letters* **2004**, *92*, 125501.

(31) Geary, J. M.; Goodby, J. W.; Kmetz, A. R.; Patel, J. S. *Journal of Applied Physics* **1987**, *62*, 4100-4108.

(32) Gardner, C. L.; Anantaraman, A. V. *Journal of Electroanalytical Chemistry* **1998**, *449*, 209-214.

(33) Gruber, K.; Loibl, H.; Schlauf, T.; Pallanits, J.; Gornik, C.; Kronberger, H.; Fafilek, G.; Nauer, G. *Electrochemistry Communications* **2007**, *9*, 1288-1292.

(34) Hensley, J. E.; Way, J. D.; Dec, S. F.; Abney, K. D. *Journal of Membrane Science* **2007**, *298*, 190-201.

# Chapter 4

## Switchable Bistable Ordering and Real-Time Alignment Dynamics in Wormlike Micelles

Reprinted with permission from K.G. Wilmsmeyer, X. Zhang and L.A. Madsen, *Soft Matter* **2012**, *8*, 57-60 © 2012, reproduced by permission of the Royal Society of Chemistry.

### 4.1 Abstract

Using a combination of rheology and magnetic resonance known as "rheo-NMR" we observe, in real time, the shear- and field-dependent dynamics of orientational order in a wormlike micelle (WLM). We construct a dynamical phase diagram, yielding a range where bistable shear-activated phase switching occurs in which WLMs are stably isotropic (> 12 h) before shearing, and yet realign with $\mathbf{B_0}$ after shearing. Furthermore, we extract anisotropic viscoelastic coefficients for the first time in a WLM by precisely fitting nonlinear realignment data. This deepened understanding of complex surfactant fluid dynamics lights a path toward increased materials control in advanced lubricants and coatings, drug delivery, and tissue engineering.

### 4.2 Introduction

Cylindrical, or wormlike, micelles constitute an intermediate phase of soft matter, encompassing properties of liquid crystals, entangled polymers, and molecular amphiphiles, with applications as diverse as personal care products, oil exploration, and lubrication. Amphiphiles can associate into various supramolecular aggregates, including spheres, vesicles, lamellae, and cylinders, based on molecular functionality and the relative sizes of their hydrophobic and hydrophilic functionalities.[1,2] WLMs possess unique viscoelastic, patterning, and encapsulation properties and thus represent pivotal components used in fracturing fluids in oil fields,[3] personal

care product viscosity modifiers,[3] electrospun tissue scaffolds,[4] and drug delivery agents.[5] WLMs can be made polymerizable,[6] and can form effective polymerization templates in which the resulting polymer retains the high aspect ratio of the micellar template and exhibits narrow polydispersity.[7] WLMs have also been shown to form viscoelastic gels[8] which can be adopted as scaffolds for nanomaterial manufacture. After intense experimental and theoretical scrutiny, many fundamental behaviors of WLMs evade understanding, such as: How does ordering couple to viscoelastic behavior? What is the nature of WLM entanglement?

WLM systems exhibit properties similar to polymer solutions, such as nonlinear stress-strain behavior, as the wormlike "chains" entangle with one another in analogy to conventional polymer chains, and these cylinders can additionally align to form a nematic liquid crystalline phase.[1,9,10] Here, we study cetyltrimethylammonium bromide (CTAB) in the range 17 - 23 wt % in $^2H_2O$, where CTAB self-assembles into cylinders of ~ 4 nm diameter.[11]

We employ rheo-NMR[12,13] to provide detailed molecular-scale understanding of these materials under macroscopic shear forces. Rheo-NMR is non-destructive, *in situ*, allows for straightforward theoretical interpretation, and does not require optically transparent samples. Shear-induced behaviors such as shear banding and the shear-dependence of the isotropic-to-nematic transition have been addressed using rheo-NMR,[14,15] small-angle neutron scattering under shear (SANSUS),[16] and theory.[17] Here, we use $^2H$ NMR spectroscopy to observe background solvent $^2H_2O$ molecules, which report on local micellar order. Previous studies involving CTAB WLMs have used $^2H$ NMR to show spontaneous (static) magnetic alignment in the nematic phase.[18] The present study allows observations of a *bistable* shear-induced transition not previously observed in any WLM system. Futhermore, by time-resolving the complex director realignment dynamics (from shear to magnetic alignement), and employing a continuum

Leslie-Ericksen theory formalism,[19,20] we extract the first measurements of Leslie-Ericksen anisotropic viscoelastic parameters for a WLM.

We monitor WLM phase alignment sensitively as a function of shear *in situ*, and construct a dynamical phase diagram of shear and magnetic alignment as a function of composition and temperature T. We find a broad range of composition and T over which the nematic WLMs spontaneously align with the spectrometer magnetic field ($\mathbf{B_0}$), or they can shear align perpendicular to $\mathbf{B_0}$ in our axial Couette cell. At higher T, CTAB solutions exhibit a region of isotropic behavior where they will not align with $\mathbf{B_0}$ or applied shear. Furthermore, we observe a novel intermediate phase that maintains long-term isotropy in a magnetic field until aligned in a perpendicular shear field. When shear is ceased, the phase realigns and stabilizes along the much weaker magnetic field. This intermediate phase region persists in either isotropic (pre-shear) or magnetically-aligned nematic (post-shear) phase for > 12 h, with transition back to the isotropic pre-shear phase accomplished by a simple temperature cycle.

Because deuterium is a spin I = 1 nucleus with a large electric quadrupole moment, its unique properties can be exploited in NMR experiments. The electric quadrupole moment of the nucleus interacts with the electric field gradient of the molecular bond in which it resides to produce a splitting in the $^2$H spectrum.[21] In our system, the deuterons on the $^2H_2O$ probe molecules show a quadrupole splitting $\Delta\nu_Q$ in the spectrum described by[21,22]

$$\Delta\nu_Q = Q_P S P_2(\cos\phi) = Q_P \rho S_{matrix} P_2(\cos\phi) \tag{4.1}$$

where $Q_P$ is the principle quadrupole tensor component along the molecular bond axis (~ 260 kHz), and $S = \langle P_2(\cos\chi)\rangle$ is the orientational order parameter of the $^2H_2O$ probes. $\chi$ is the angle of an O-$^2$H bond axis relative to the alignment axis (director) of the WLM matrix and $\langle P_2(\cos\chi)\rangle = \langle (3\cos^2\chi - 1)/2\rangle$ is the time and spatial average of the second Legendre polynomial. $\phi$ is the

angle between the director of the WLM matrix and $\mathbf{B_0}$. Because we are interested in the order parameter of the WLM matrix $S_{matrix}$, we express $S = \rho S_{matrix}$ as $S_{matrix} = \langle P_2(\cos \alpha) \rangle$ the ensemble average over the second Legendre polynomial where $\alpha$ is the angle between a particular micelle segment and the director of the WLM phase. $\rho$ is a scaling factor determined by interactions between the probe molecule and the WLM matrix, and is generally insensitive to temperature[22,23] for a given probe-matrix system at a given composition.

Isotropic tumbling, as in a simple liquid, causes molecules to experience all angles $\chi$ rapidly compared with the NMR ($Q_P$) timescale, averaging the quadrupolar Hamiltonian (and thus the splitting) to zero.[15] However, if a deuterated probe molecule (here, $^2H_2O$) is present in an aligned WLM system, the motional averaging of the deuterated probe tumbling within the constraints of the micelles will be incomplete, causing the molecule to "inherit" the order of its surroundings, and exhibit a doublet in the spectrum.[21-23] Thus, at a given temperature and composition with monodomain alignment, $\Delta\nu_Q$ reports on the angle and degree of WLM matrix alignment under shear or magnetic fields. We observe only a single doublet in the spectrum during shear and $\mathbf{B_0}$ alignment, indicating uniaxial monodomain alignment.

## 4.3 Materials and Methods

### 4.3.1 WLM Preparation

This study uses the surfactant cetyltrimethylammonium bromide (CTAB, cetyl = hexadecyl, Alfa Aesar) dissolved in $^2H_2O$ (Cambridge Isotope Laboratories, 99.9% $^2H$) and regulated at 45 °C with gentle stirring for 48 h. CTAB concentrations of 18.0, 19.0, 20.0, 21.0, 22.0, and 23.0 wt % (± 0.1 wt %) of total solution (0.67, 0.71, 0.76, 0.81, 0.86, and 0.91 M, respectively) are used for rheo-NMR studies. At least 24 h prior to experiments, samples are poured into a Couette cell, sealed with Parafilm, and allowed to rest at 40 °C. This ensures that

measurements are not biased by shear history upon cell assembly. Solutions are maintained above 25°C to prevent crystallization.

### 4.3.2 Rheo-NMR Spectroscopy

A Varian Unity NMR spectrometer ($\mathbf{B_0}$ = 9.4 T, $\nu_{2H}$ = 61.395 MHz) applies a pulse-acquire sequence with 90° pulse of 25.0 μs. $^2$H spectra are single acquisitions in order to accurately map sample behavior over time with ≤ 1 s time resolution. Typical FWHM linewidths in the $^2$H spectra are ~ 2 Hz (shim limited). The custom rheo-NMR apparatus consists of a Couette cell (concentric cylinders) with rotation axis along $\mathbf{B_0}$, comprised of a 10 mm O.D. NMR tube (9.03 mm I.D.) and a 7.45 mm O.D. NMR tube[24] separated by Delrin® spacers, and CTAB sample is held in the 0.79 mm gap. This cell produces $\dot{\gamma} = 31.4 \pm 0.5\ s^{-1}$ per 1 Hz revolution of the inner cylinder.[24] Shear rate is varied using a computer interface (software: SMC60WIN SD130, v. 2.01; programmable driver: DPY50601, Anaheim Automation), which controls a stepper motor mounted above the NMR magnet. A brass drive shaft rotating on Teflon® bearings couples the stepper motor to the inner cylinder of the Couette cell. Interchangeable stepper motors with varying gear ratios (1:1 motor #23YSG106S-LW8, 1:12.5 motor #23YSG106S-LW8-R12.5, and 1:100 motor #23YSG106S-LW8-R100, Anaheim Automation) allow access to over five decades of shear rate.

## 4.4 Results and Discussion

NMR spectra at equilibrium show that WLMs spontaneously align with $\mathbf{B_0}$ over a wide range of temperatures. This alignment occurs due to the anisotropy of magnetic susceptibility ($\chi_a$) of the cylindrical worms, and is attributed simply to the susceptibility difference between the WLMs and solvent coupled with the shape anisotropy of the cylinders. Field-induced orientational order is quite common in liquid crystalline materials[21] and has been reported in

nematic wormlike micelle systems.[9,18] Alignment with $\mathbf{B_0}$ occurs with two timescales governed by distinct processes, with equilibrium typically reached in a few hours. The alignment dynamics follow Leslie-Ericksen continuum dynamic theory,[19,20] which is the basis for our mathematical treatment below. Further, we see an increase in quadrupolar splitting values with increasing concentration, which is likely due to the $^2H_2O$ probe molecules being increasingly constrained as the WLM volume fraction rises ($\rho$ rises).

In this WLM system, we investigate orientational order dependencies on concentration, shear rate (ranging from $\dot{\gamma}$ = 0.01 to 130 $s^{-1}$), time after initiating shear, and T. Complete alignment under shear rate $\dot{\gamma}$ = 1 $s^{-1}$ occurs significantly faster (~ 10 s) than the spontaneous field alignment at the same T, signifying that even moderate shear forces are orders of magnitude greater than the alignment force of the $\mathbf{B_0}$ field. We can define a "critical shear rate" ($\dot{\gamma}_c$) at which shear and field alignment forces exactly cancel one another and provide a singlet in the spectrum. For example, with 20 wt % CTAB in $^2H_2O$ at 28 ºC, we find $\dot{\gamma}_c \sim 0.06$ $s^{-1}$.

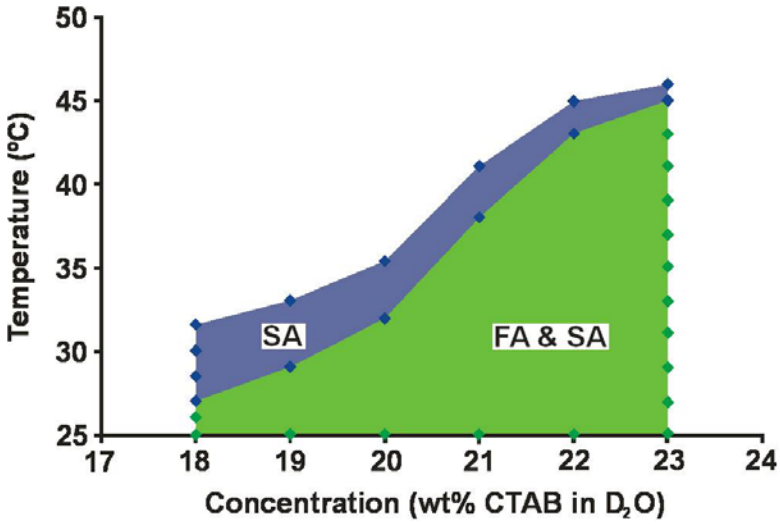


**Figure 4.1. Dynamical phase diagram for CTAB in $^2H_2O$ as a function of temperature and concentration.** Two regions manifest in our rheo-NMR experiments: one where field alignment occurs spontaneously along with readily attainable shear alignment (labeled "FA & SA"), and a higher T region where micelles do not spontaneously field align, but do shear align (labeled "SA").

### 4.4.1 Shear- and Field-Alignment Behavior

Using data from both spontaneous field alignment and shear alignment experiments, we

have constructed the "dynamical" phase diagram shown in fig. 4.1. We observe two distinct regions, which we have labeled as "field alignment" (FA) and "shear alignment" (SA). In the FA region, the WLMs align parallel to $\mathbf{B_0}$. In the SA region, the WLMs can be aligned perpendicular to $\mathbf{B_0}$, notably *over a range of T higher than where they spontaneously field align*.

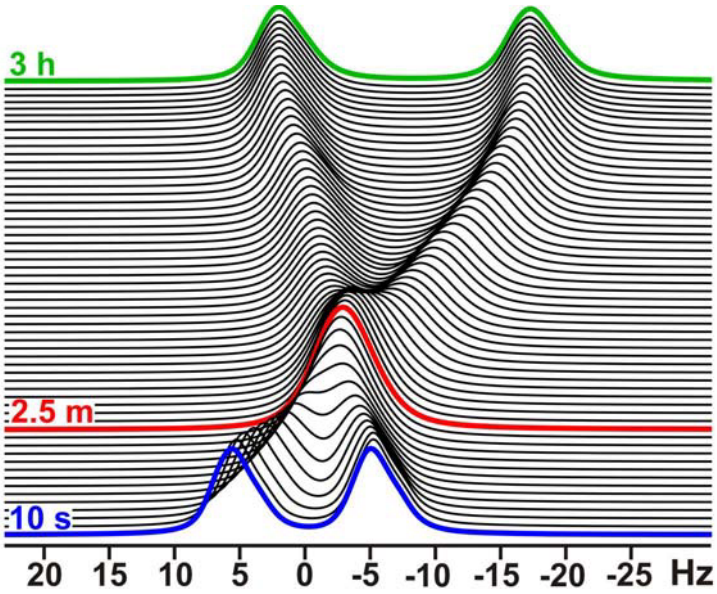


**Figure 4.2. $^2$H NMR spectra showing WLM realignment after shear cessation.** Data shown for 20 wt % CTAB at 31 ºC, covering 3 hours after cessation of shear ($\dot{\gamma}$ = 31.42 s$^{-1}$). In accordance with eqn. 4.1, the initial value of $\Delta\nu_Q$ (first spectrum at $t$ = 10 s) is approximately ½ that of the final value (after 3 h - field aligned), and there is a crossover (single peak) at $t$ = 2.5 min when the director is along the magic angle $\phi$ = 54.7°.

The FA direction is signified by the 2:1 ratio of quadrupole splitting in the FA *vs.* SA states ($-0.5\Delta\nu_Q^{FA} = \Delta\nu_Q^{SA}$), following the $P_2(\cos\phi)$ dependence of eqn. 4.1 (see fig. 4.2). Note that eqn. 4.1 has a zero at $\phi$ = 54.7º (the so-called "magic" angle), which causes the spectrum to again manifest as a singlet. This singlet appears solely because the micellar director rotates through 54.7º, not due to the system transitioning to the isotropic phase. Under static conditions, these two cases are indistinguishable, but we can separate them easily with our dynamical rheo-NMR measurements. Within the FA region, shear alignment can still be achieved; however, in the SA-only region, field alignment will not spontaneously occur without prior stimulus. Previous phase diagrams determined by NMR and birefringence[15,16,18] indicate regions of nematic, isotropic, and hexagonal behavior of the CTAB WLMs, but do not describe dynamic phase behavior induced by shear forces. The upper limit of

the SA region is derived at shear alignment plateau values with $\dot{\gamma} \geq 10\ s^{-1}$.

### 4.4.2 Realignment Dynamics

In addition to the field and shear alignment properties discussed, we find that upon raising T a few degrees above the initial FA range (*e.g.*, to 33 ºC for 20 wt % CTAB), the WLMs will align as expected under shear, but also exhibit intriguing field alignment properties after shear (see fig. 4.1). Specifically, upon cessation of shear, fig. 4.2 shows WLM realignment with $\mathbf{B_0}$, which occurs over the entire FA & SA phase region of fig. 4.1, but surprisingly *even at temperatures greater than the initial pre-shear field alignment range* (in the SA-only region). The spectra in fig. 4.2 also indicate that the transition between SA and FA occurs such that there is no breakup of domains that rotate at different rates. We do not observe broad signals or powder patterns (superpositions) in the NMR spectra on the averaging timescale of this NMR experiment (~ 10 ms), and thus all domains rotate at the same rate during realingnment with minimal variation in angle between domains.

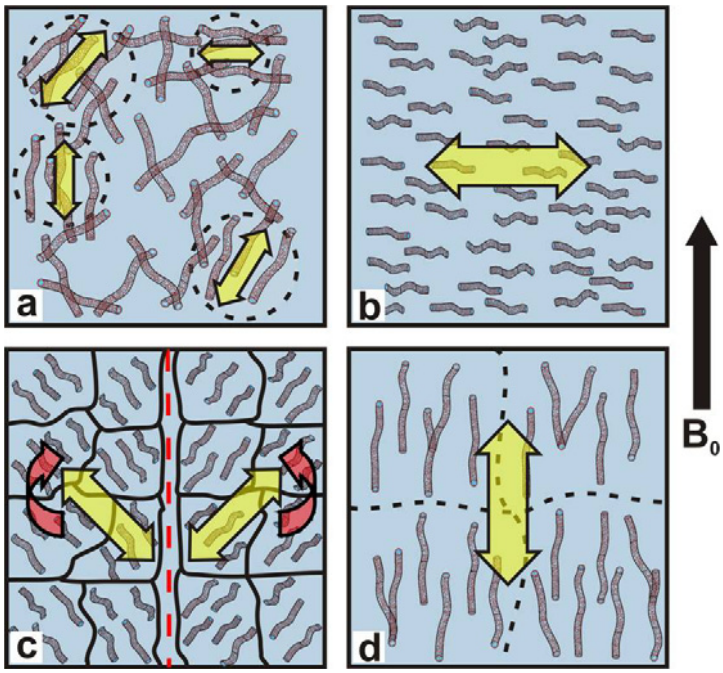


**Figure 4.3. Illustration of WLM realignment motif. a,** isotropic solution of WLMs prior to shear, **b,** WLMs under strong shear flow ($\phi$ = 90º), **c,** backflow and realignment with spectrometer field ($\mathbf{B_0}$) following cessation of shear, **d,** stable alignment with $\mathbf{B_0}$ ($\phi$ = 0º). The arrow on the right indicates the direction of the magnetic field (perpendicular to shear direction), block arrows indicate WLM director alignment, and curved arrows indicate rotation direction in the $\mathbf{B_0}$ field. As an example, the director is at $\phi \approx 54.7º$ in part **c**, where the NMR splitting vanishes.

Figure 4.3 shows a proposed WLM realignment scheme, wherein the highly entangled WLMs are broken apart by the shear forces into aligned domains along the shear direction. After shear cessation, small domains (likely encompassing shorter cylinders) can then rapidly realign with the magnetic field, and finally the small domains grow slowly into a monodomain with greater overall ordering, and likely encompassing longer worms. We note that the isotropic and field-aligned nematic phases have long-term stability (> 12 h) in the spectrometer magnetic field, and hence are bistable and switchable.

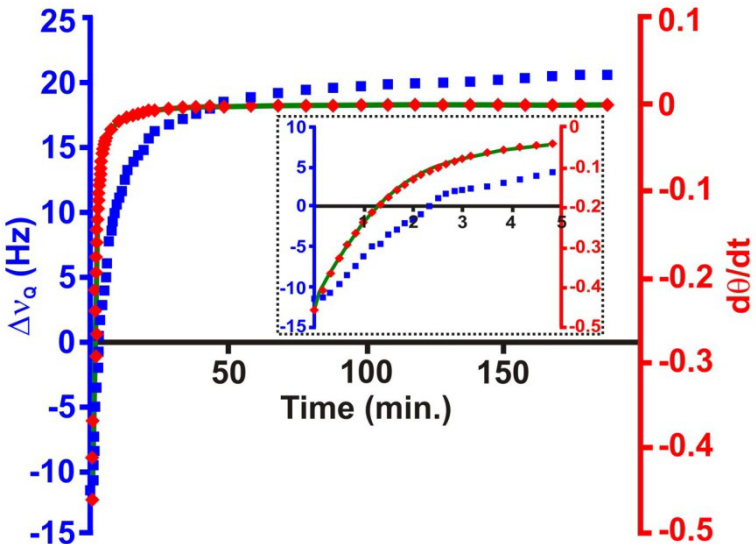


**Figure 4.4. WLM realignment dynamics.** Micellar director realigns with $\mathbf{B_0}$ after (perpendicular) shear alignment ($\dot{\gamma}$ = 31.42 $s^{-1}$). $\Delta\nu_Q$ splittings are shown as squares and calculated $d\theta/dt$ values as diamonds. The solid line is the fit to $d\theta/dt$, yielding viscoelastic parameters. The inset details the first 5 min of realignment. Composition is 20 wt % and T = 31 ºC.

We fit our spectroscopic data based on the treatments of nematic liquid crystalline polymer (LCP) systems outlined by Martins *et al.*[19] and Kothe *et al.*[20] The director dynamics follow that of backflow and realignment observed in similarly realigning LCPs. Because the value of $\chi_a$ has not yet been measured for the CTAB/$^2H_2O$ or any similar WLM system, our fit utilizes a fixed estimate of 1.0 x $10^{-7}$ cgs based on measurements of other lyotropic nematics.[25,26] Fit results using this estimate are excellent (see fig. 4.4), and are quite sensitive to order of magnitude changes in $\chi_a$.

Our fitting program provides values for $k_{33}/k_{11}$,[27] $\gamma_1$, $\alpha_1$, $\alpha_2$, and $\eta_c$. Values for $\eta_b$, $\alpha_3$, and $\gamma_2$ are derived from the Parodi relations[28] and equations relating the Miesowicz viscosities[29] with the Leslie coefficients.[30,31] Table 4.1 shows typical fit results for the CTAB/$^2H_2O$ system. It is important to note that we observe the expected sign in all cases, however our measured parameters are 1 - 2 orders of magnitude larger than those reported on LCPs by Martins.[19]

**Table 4.1. Fit results for 20 wt % CTAB in $^2H_2O$ sample at 31 ºC.** Parameters marked with * are calculated from fit parameters.

| Parameter | Value | Error |
|---|---|---|
| $k_{11}qz^2$ (dyn/cm$^2$) | 600 | ± 1.8 |
| $k_{33}/k_{11}$ | 1.51 | ± 0.007 |
| $\gamma_1$ (P) | 44,800 | ± 2,100 |
| $\alpha_1$ (P) | -60,000 | ± 7,400 |
| $\alpha_2$ (P) | -28,000 | ± 1,700 |
| $\eta_c$ (P) | 7,400 | ± 850 |
| * $\eta_b$ (P) | 3,900 | ± 1,800 |
| * $\alpha_3$ (P) | 16,700 | ± 2,700 |
| * $\gamma_2$ (P) | -11,300 | ± 3,200 |

Because these are the first reported measurements of the viscoelastic parameters for a WLM system, here we make comparisons with other systems that behave as nematic liquid crystals.

### 4.5 Concluding Remarks

We have investigated phase behavior and dynamics of shear and magnetic field alignment in CTAB/$^2H_2O$ WLMs as a function of composition, aligning field strength, and temperature. We observe a novel bistable shear-induced phase in which WLMs will not align along $\mathbf{B_0}$ until after they have been shear aligned. This work, to our knowledge, is the first report of measurements of the anisotropic viscoelastic parameters for a WLM system. We are continuing to study this system by correlating solution rheology measurements to our rheo-NMR experiments. Additionally, we are using pulsed-field-gradient NMR techniques to investigate self-diffusion behavior of the WLMs in both the aligned and unaligned state, and have begun to experiment

with inclusion of molecules which reside either in the core of the micelles or in between the micelles, for potential applications as variable NMR alignment media in biological structure determination. Deep understanding of these systems will promote further design of micellar materials, and allow tailoring of viscoelastic and long-range alignment behavior for applications in tissue engineering, oil extraction, and advanced coatings and lubricants.

**References**


(1) Cates, M. E.; Candau, S. J. *J. Phys.: Condens. Matter* **1990**, *2*, 6869-6892.

(2) Evans, D. F.; Ninham, B. W. *J. Phys. Chem.* **1986**, *90*, 226-234.

(3) Yang, J. *Curr. Opin. Colloid & Interface Sci.* **2002**, *7*, 276-281.

(4) McKee, M. G.; Layman, J. M.; Cashion, M. P.; Long, T. E. *Science* **2006**, *311*, 353-355.

(5) Kim, Y.; Dalhaimer, P.; Christian, D. A.; Discher, D. E. *Nanotechnology* **2005**, *16*, S484-S491.

(6) Liu, S. Y.; Gonzalez, Y. I.; Danino, D.; Kaler, E. W. *Macromolecules* **2005**, *38*, 2482-2491.

(7) Walker, L. M.; Kuntz, D. M. *Curr. Opin. Colloid & Interface Sci.* **2007**, *12*, 101-105.

(8) Vasudevan, M.; Buse, E.; Lu, D. L.; Krishna, H.; Kalyanaraman, R.; Shen, A. Q.; Khomami, B.; Sureshkumar, R. *Nature Mater.* **2010**, *9*, 436-441.

(9) Alam, T. M.; McIntyre, S. K. *Langmuir* **2008**, *24*, 13890-13896.

(10) Lopez-Gonzalez, M. R.; Holmes, W. M.; Callaghan, P. T. *Soft Matter* **2006**, *2*, 855-869.

(11) Coppola, L.; Gianferri, R.; Nicotera, I.; Oliviero, C.; Ranieri, G. A. *Phys. Chem. Chem. Phys.* **2004**, *6*, 2364-2372.

(12) Nakatani, A. I.; Poliks, M. D.; Samulski, E. T. *Macromolecules* **1990**, *23*, 2686-2692.

(13) Callaghan, P. T. *Rep. Prog. Phys.* **1999**, *62*, 599-670.

(14) Angelico, R.; Burgemeister, D.; Ceglie, A.; Olsson, U.; Palazzo, G.; Schmidt, C. *Journal of Physical Chemistry B* **2003**, *107*, 10325-10328.

(15) Fischer, E.; Callaghan, P. T. *Phys. Rev. E* **2001**, *6401*.

(16) Cappelaere, E.; Berret, J. F.; Decruppe, J. P.; Cressely, R.; Lindner, P. *Phys. Rev. E* **1997**, *56*, 1869-1878.

(17) Lu, C. Y. D.; Olmsted, P. D.; Ball, R. C. *Phys. Rev. Lett.* **2000**, *84*, 642-645.

(18) Clawson, J. S.; Holland, G. P.; Alam, T. M. *Phys. Chem. Chem. Phys.* **2006**, *8*, 2635-2641.

(19) Martins, A. F.; Esnault, P.; Volino, F. *Phys. Rev. Lett.* **1986**, *57*, 1745-1748.

(20) Lukaschek, M.; Kothe, G.; Schmidt, C.; Gomes, A. E.; Polimeno, A. *J. Chem. Phys.* **2002**, *117*, 4550-4556.

(21) *NMR of Ordered Liquids*; Burnell, E. E.; de Lange, C. E., Eds.; Kluwer: Dordrecht, 2003.

(22) Li, J.; Wilmsmeyer, K. G.; Madsen, L. A. *Macromolecules* **2009**, *42*, 255-262.

(23) Deloche, B.; Samulski, E. T. *Macromolecules* **1981**, *14*, 575-581.

(24) Douglass, B. S.; Colby, R. H.; Madsen, L. A.; Callaghan, P. T. *Macromolecules* **2008**, *41*, 804-814.

(25) Stefanov, M.; Saupe, A. *Mol. Cryst. Liq. Cryst.* **1984**, *108*, 309-316.

(26) Vijayaraghavan, D.; Suresh, K. A. *Mol. Cryst. Liq. Cryst.* **2005**, *434*, 609-618.

(27) Frank, F. C. *Discussions Faraday Soc.* **1958**, *25*, 19-28.

(28) Parodi, O. *J. Phys.-Paris* **1970**, *31*, 581-584.

(29) Miesowicz, M. *Nature* **1946**, *158*, 27.

(30) Ericksen, J. L. *Trans. Soc. Rheol.* **1961**, *5*, 23-34.

(31) Leslie, F. M. *Arch. Rat. Mech. Anal.* **1968**, *28*, 265-283.

# Chapter 5

## Rheology and Anomalous Diffusion in Cetyltrimethylammonium Bromide Wormlike Micelles

K.G. Wilmsmeyer, R. Zhang, X. Zhang and L.A. Madsen, manuscript in preparation for submission to *Liquid Crystals*.

### 5.1 Abstract

Using solution rheology, rheo-NMR, and pulsed-field-gradient (PFG) NMR, we observe orientational order and dynamics in a wormlike micelle (WLM) system. We measure, for the first time in a WLM, the five independent Leslie viscosities by fitting nonlinear realignment data and comparing with traditional solution rheology measurements. Additionally, we extract self-diffusion coefficients in three orthogonal directions for the WLMs as well as for background solvent molecules. We also observe disparity in the viscoelastic behavior of the WLM system in $H_2O$ vs $D_2O$. Continued study and enhanced understanding of complex fluid dynamics in these surfactant systems can lead to advances in lubricants, coatings, drug delivery, and tissue engineering.

### 5.2 Introduction

Wormlike (*a.k.a.* cylindrical or rodlike) micelles are flexible, elongated structures which can self-assemble via aggregation of molecular amphiphiles at concentrations above the critical micelle concentration *CMC*.[1] Above the critical entanglement concentration $C_e$, they will entangle and form a transient network,[2] analogous to polymer chain entanglement, which exhibits unique viscoelastic properties. Due to shape anisotropy of the worm tubes, WLMs can also align over macroscopic distances, forming a nematic liquid crystalline phase.[3-5] Because of their remarkable viscoelastic, encapsulation, and patterning behavior, WLMs are of significant

interest for applications as varied as personal care product viscosity modifiers,[6] reservoir stimulation in oil fields,[6] drug delivery systems,[7] and electrospun tissue scaffolds.[8] They have been used for drag reduction in district heating and cooling systems,[9] and can form viscoelastic gels[10] useful in manufacture of nanomaterials. WLMs have been made polymerizable,[11] can be coupled to polymers as micellar "hybrids,"[12,13] and have been shown to form effective polymerization templates which give the resulting polymer low polydispersity and high aspect ratio.[14] In this study, we examine cetyltrimethylammonium bromide (CTAB) at concentrations of 16 – 24 wt % (above $C_e$), where CTAB self-assembles into ~ 4 nm diameter WLMs.[15]

### 5.2.1 $^2$H Rheo-NMR Spectroscopy

Here, we utilize a combination of solution rheology and nuclear magnetic resonance techniques known as rheo-NMR, allowing us to observe molecular-scale behavior of molecules under macroscopic shear. This method does not require samples to be optically transparent, is non-destructive, *in situ*, and allows for straightforward theoretical interpretation. Rheo-NMR has been used for three decades[16] to investigate the viscoelastic properties of polymers,[17,18] liquid crystals,[19-21] WLMs,[5,22] and food products.[23]

Shear banding, the shear-dependence of the isotropic-to-nematic transition, and other shear-induced behavior have been studied using small-angle neutron scattering under shear (SANSUS),[24] rheo-NMR,[25,26] and theory.[27] In this work, we use $D_2O$ as a solvent for CTAB WLMs, simultaneously serving as deuterated probe molecules which report on local order in the micelle system. Prior studies by Clawson *et al.*[28] and Rapp *et al.*[29] utilized $^2$H NMR to show spontaneous magnetic alignment of nematic CTAB WLMs. We have also previously employed $^2$H NMR to monitor phase alignment and observe the existence of a novel bistable shear-

activated phase and to extract measurements of the Leslie-Ericksen anisotropic viscoelasticity parameters for the first time in a WLM.[30]

Deuterium, a spin $I = 1$ quadrupole nucleus, interacts with the electric field gradient of the bond in which it resides to produce a doublet (splitting) in the $^2$H NMR spectrum.[31] In this system, the deuterons of the $D_2O$ solvent molecules tumbling within the constraints of the WLM network can "inherit" the order of their surroundings and report on the local micellar order via incomplete motional averaging, exhibiting a splitting in the spectrum.[30-32] This splitting $\Delta\nu_Q$ is proportional to the orientational order parameter $S$ (*a.k.a.* the Hermann's orientation function), and is determined by[30,31]

$$\Delta\nu_Q = Q_P S P_2(\cos\phi) = Q_P \rho S_{matrix} P_2(\cos\phi) \tag{5.1}$$

where $Q_P$ is the quadrupole coupling constant along the molecular bond axis (~ 260 kHz), $\phi$ is the angle between the WLM matrix and the magnetic field $\mathbf{B_0}$, and $S = \langle P_2(\cos\chi)\rangle = \langle(3\cos^2\chi - 1)/2\rangle$ is the ensemble average of the $D_2O$ probe molecules over the second Legendre polynomial with $\chi$ the angle between a particular O-D bond axis and the WLM director. Because we are interested in $S$ for the WLM network, we express $S = \rho S_{matrix}$ as $S_{matrix} = \langle P_2(\cos\alpha)\rangle$ where $\alpha$ is the angle between a particular micelle segment and the WLM director. $\rho$ is a scaling factor determined by interactions of the probe molecules and the host matrix, and is relatively insensitive to temperature for a given system at fixed concentration.[32,33] When the WLM is in the isotropic phase, the $D_2O$ probes will experience all $\chi$, averaging the quadrupolar Hamiltonian (and the splitting) to zero.[26]

### 5.2.2 Self-Diffusion Coefficient Measurements

Transport properties of water and other molecules are commonly measured by PFG NMR self-diffusion experiments,[34-36] and self-diffusion coefficients $D$ for water and the CTAB WLMs

are of interest for drug delivery and viscosity control applications. Compared to dynamic light scattering[37] and infrared[38] techniques used to study diffusion dynamics in the CTAB/water system, PFG NMR has the particular advantage of nuclear specificity. With this method, we obtain intrinsic information on the translational motion of both the CTAB ($^1$H) and $D_2O$ ($^2$H) signals, providing independent measurements of *D* for each. As with our other NMR methods, this measurement is a non-contact technique that allows us to measure diffusion along three orthogonal axes without complex mathematical models or complicated sample mounting. We observe changes in diffusion of $D_2O$ parallel to the WLM matrix director vs perpendicular, and our $^2$H rheo-NMR results correlate well with our diffusion anisotropy findings.

### 5.2.3 CTAB Rheology

A number of rheological studies of CTAB with and without added salts have been undertaken in an effort to explain their structure and complex viscoelastic behavior.[15,39] The behavior of WLMs above $C_e$ not well understood, and competing theories have arisen based on the Cates reptation model[40] and a diffusional model[36,41,42] wherein the sliding of branching points in the interconnected network allows for easier diffusion of the surfactant molecules across the WLM matrix. It is also unclear whether strict chain entanglement or the formation of junction points is occurring above $C_e$, leading to drastically increased viscosity. Continuum Leslie-Ericksen theory has been employed by Martins et al. to describe the dynamics of nematic liquid crystal polymers,[16,43] and calculate all five anisotropic Leslie viscosities.[44,45] We have recently obtained the first measurements of the Leslie viscosities in a WLM,[30] and using our rheo-NMR methods as well as traditional rheology, we aim to shed light on the complex behavior of these WLM systems. Solution rheology studies involving various concentrations of CTAB in $D_2O$[46,47]

and $H_2O$[24,39] without added salts have been previously reported, and here we compare and contrast results in these two solvents for the first time.

## 5.3 Materials and Methods

### 5.3.1 CTAB Solutions

The CTAB surfactant (Alfa Aesar; Ward Hill, MA) used in this study was dissolved in $D_2O$ (99.9% $^2H$; Cambridge Isotope Laboratories; Andover, MA) or DI $H_2O$ and regulated at 45 °C with gentle stirring for 48 h. CTAB concentrations of 18.0 - 24.0 wt % (± 0.1 wt %) of total solution (0.67 - 0.96 M) are used. Prior to solution rheology experiments, samples are sealed in vials and maintained at 40 °C. Samples for rheo-NMR are poured into a Couette cell, sealed with Parafilm, and allowed to rest at 40 °C for at least 24 h prior to experiments. This ensures that measurements are not biased by shear history upon cell assembly. PFG samples are poured into standard 10 mm NMR tubes, capped, and sealed with Parafilm. All solutions are maintained above 25°C at all times to prevent crystallization.

### 5.3.2 Rheo-NMR

Rheo-NMR studies are performed on a Varian Unity NMR spectrometer with a magnetic field of 9.4 T and $^2H$ frequency of 61.4 MHz. A simple pulse-acquire sequence with 90° pulse of 25.0 μs is applied, and $^2H$ spectra are single acquisitions in order to accurately map sample behavior over time with ≤ 1 s time resolution. Typical FWHM linewidths in the $^2H$ spectra are ~ 2 Hz. The rheo-NMR apparatus is custom-built, and consists of a Couette cell (concentric cylinders) with rotation axis along $\mathbf{B_0}$, comprised of two standard NMR tubes (10 mm and 7.5 mm). The outer tube has i.d. = 9.03 mm and the inner tube has o.d. = 7.45 mm. The tubes are separated by Delrin spacers, and CTAB/$D_2O$ sample is held in the 0.79 mm gap. The cell produces $\dot{\gamma} = 31.4 \pm 0.5\ s^{-1}$ per 1 Hz revolution of the inner cylinder.[22] Shear rate is varied via a

computer interface (software: SMC60WIN SD130, v. 2.01; programmable driver: DPY50601; Anaheim Automation; Anaheim, CA), which controls a stepper motor mounted above the NMR magnet. A brass drive shaft rotating on Teflon bearings couples the stepper motor to the inner cylinder of the Couette cell while the outer cylinder of the cell remains fixed to the NMR probe. Interchangeable stepper motors with varying gear ratios (1:1 motor #23YSG106S-LW8; 1:12.5 motor #23YSG106S-LW8-R12.5; and 1:100 motor #23YSG106S-LW8-R100; Anaheim Automation; Anaheim, CA) permit us to access over five decades of shear rate, from 0.01 to 150 $s^{-1}$.

### 5.3.3 PFG NMR

Self-diffusion coefficients *D* were measured using a Bruker Avance III WB NMR spectrometer (Bruker-BioSpin; Billerica, MA) at a magnetic field of 9.4 T, with $^{1}H$ frequency of 400 MHz and $^{2}H$ frequency of 61.4 MHz. This instrument is equipped with a triple axis diffusion probe having a maximum gradient strength of 290 G/cm, capable of measuring *D* in three orthogonal directions without requiring the sample to be reoriented. Pulsed-gradient stimulated echo (PGSTE) experiments were performed at temperatures from 25 - 65 ºC, calibrated to an accuracy of 0.2 ºC using 100% ethylene glycol standard. The gradient constant is calibrated to a literature value of $D$ = 1.872 x $10^{-9}$ $m^2/s$ for 1 % $H_2O/D_2O$ doped with 0.1 mg/mL $GdCl_3$ at 25 ºC.

Free diffusion NMR signal attenuation is described by:[35]

$$I = I_0 e^{-D\gamma^2 g^2 \delta^2 (\Delta - \delta/3)} \tag{5.2}$$

where $I$ is the spin-echo signal intensity, $I_0$ is the signal intensity under zero gradient, $\gamma$ is the gyromagnetic ratio of the probe nucleus, $\delta$ is the duration of the gradient pulse with magnitude $g$, $D$ is the self-diffusion coefficient, and $\Delta$ is the duration between the leading edges of the two

gradient pulses. Signal intensity $I$ is measured as a function of $g$ to obtain $D$ for CTAB and $D_2O$ in the system. We estimate an accuracy of $D = \pm 3$ % in these samples.

### 5.3.4 Solution Rheology

All solution rheology experiments in this study are performed on an AR-G2 rheometer (TA Instruments; New Castle, DE) equipped with a Peltier recessed end concentric cylinder geometry with temperature control. Temperature was varied from 25 - 65 ºC with tolerance ± 0.2 ºC. A steel stator with inner radius 15.00 mm holds ~ 7 mL of sample, and a steel rotor with outer radius 14.00 mm is immersed to a height of 42.00 mm. Shear rate is varied from 0.15 to 150 $s^{-1}$, corresponding to our rheo-NMR experiments. In some circumstances, formation of foam was observed at the end of the experiment, however, all results reported here correspond to experiments wherein formation of foam or air bubbles was not observed. Fresh CTAB solutions were used for each experiment.

## 5.4 Results and Discussion

### 5.4.1 Rheo-NMR and Alignment Dynamics

Equilibrium NMR spectra show that WLMs align spontaneously with the spectrometer magnetic field $\mathbf{B_0}$ over a wide range of temperatures and concentrations, which is attributed to the shape anisotropy of the cylindrical worms and the difference in anisotropy of magnetic susceptibility ($\chi_a$) of the WLMs vs the solvent. In our previous study,[30] we constructed a dynamical phase diagram for the

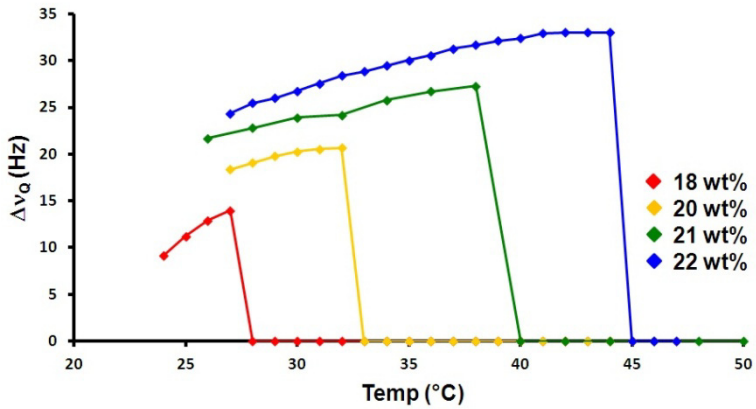


**Figure 5.1. Spontaneous $B_0$ field alignment of CTAB WLMs in $D_2O$.**

CTAB/$D_2O$ system, indicating regions of shear alignment and spontaneous field alignment. Here, we note that a gradual *increase* in quadrupolar splitting occurs with increasing temperature, until the WLM transitions to the isotropic phase, contrary to typical liquid crystal measurements and similar measurements of CTAB/$H_2O$/NaSal.[48] Figure 5.1 shows this effect for several different concentrations of CTAB. This effect may be due to increased thermal energy in the system causing the micelles to expand slightly (WLM volume fraction increases), which would cause the $D_2O$ probe molecules floating between individual micelles to be more rotationally biased, resulting in an increase in apparent order.

We shear align the WLM system by initiating shear flow in the Couette cell perpendicular to the magnetic field direction, as shown in fig. 5.2. Physically, prior to application of shear, WLMs are randomly oriented and thus $D_2O$ molecules sample all angles $\phi$ relative to $\mathbf{B_0}$, resulting in zero quadrupole splitting and thus a singlet in the $^2H$ spectrum. Upon shearing, the micelles experience a force which torques them into the flow direction perpendicular to $\mathbf{B_0}$. We note that even low shear rates (~ 0.06 $s^{-1}$ for 20 wt% CTAB in $D_2O$ at 28 ºC) are sufficient to overcome the force of the $\mathbf{B_0}$ field and exhibit alignment along the flow field, evidenced by quadrupole splitting in the $^2H$ spectrum. The data in fig. 5.2 show two different rates of director alignment, one at low shear rates (< 5 $s^{-1}$) characterized by rapid response in $\Delta\nu_Q$ values, and another at moderate shear rates (5 - 30 s-1) characterized by

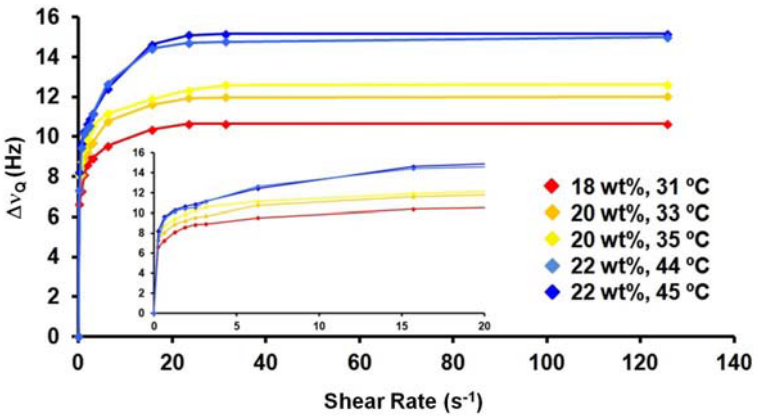


**Figure 5.2. WLM alignment under shear flow** as a function of shear rate. Inset details low shear rate behavior.

slower, but still gradually increasing values of $\Delta\nu_Q$ and thus WLM director alignment. At higher shear rates (> 30 s-1), we do not observe any additional increase in WLM alignment. We note that alignment becomes saturated along the shear flow direction at shear rates of ~ 30 $s^{-1}$, and that saturation at a given shear rate occurs in < 1 min., as observed by a maximum in the $^2H$ splitting in the NMR spectrum. Additionally, we observe a temperature dependence of the alignment ($^2H$ splitting), which can be seen in the 20 and 22 wt% traces in figs. 5.2 and 5.3. This dependence shows both a higher maximum $^2H$ splitting and faster response of the system with increased temperature.

Upon cessation of shear, we follow realignment dynamics with the magnetic field as a function of time (fig. 5.3), and fit this realignment behavior[30] near the I-N transition to continuum Leslie-Ericksen viscoelasticity theory based on nematic liquid crystalline polymer systems studied by Martins *et al.*[16] and Kothe *et al.*[49] Since $\chi_a$ has not yet been determined for CTAB/$D_2O$ or similar system, we use a fixed estimate of 1.0 x $10^{-7}$ cgs based on other lyotropic nematic measurements,[50,51] which provides excellent, sensitive fits.[30] Tables 5.1 – 5.3 show the resulting fit values at several concentrations and temperatures for the bend-to-splay ratio $k_{33}/k_{11}$,[52] $\gamma_1$, $\alpha_1$, $\alpha_2$, and $\eta_c$. Values for $\eta_b$, $\alpha_3$, and $\gamma_2$ are calculated using the Parodi relations[53] and equations which relate the Leslie coefficients[54,55] with the Miesowicz viscosities.[56]

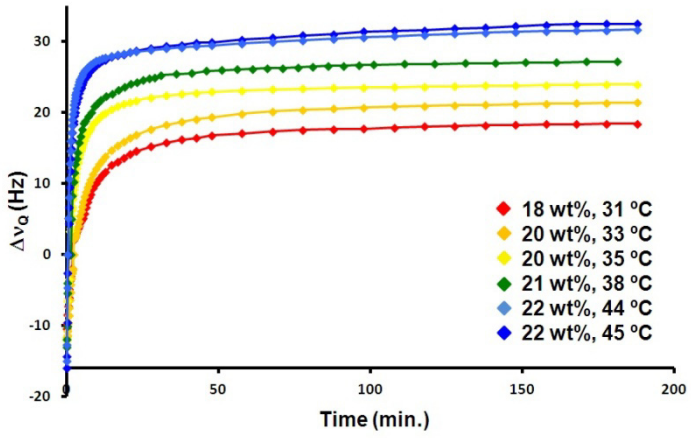


**Figure 5.3. Realignment of CTAB WLMs with $B_0$** as a function of time after cessation of shear. The temperatures shown are near or just below the I-N transition for their respective temperatures.

**Table 5.1. Leslie-Ericksen viscoelasticity fit results for 18 wt % CTAB in $D_2O$.**

| Parameter | 18 wt %, 27 °C | 18 wt %, 31 °C |
|---|---|---|
| $k_{33}/k_{11}$ | 1.61 ± 0.007 | 1.58 ± 0.008 |
| $\gamma_1$ (P) | 32,100 ± 2,800 | 31,100 ± 2,000 |
| $\alpha_1$ (P) | -47,500 ± 2,900 | -45,600 ± 7,000 |
| $\alpha_2$ (P) | -21,400 ± 2,100 | -19,200 ± 1,500 |
| $\eta_c$ (P) | 4,700 ± 260 | 4,500 ± 560 |
| * $\eta_b$ (P) | 6,000 ± 2,200 | 2,800 ± 940 |
| * $\alpha_3$ (P) | 11,900 ± 910 | 10,700 ± 1,100 |
| * $\gamma_2$ (P) | -9,500 ± 1,300 | -8,500 ± 1,000 |

**Table 5.2. Leslie-Ericksen viscoelasticity fit results for 20 wt % CTAB in $D_2O$.**

| Parameter | 20 wt %, 29 °C | 20 wt %, 31 °C | 20 wt %, 33 °C | 20 wt %, 35 °C |
|---|---|---|---|---|
| $k_{33}/k_{11}$ | 1.53 ± 0.006 | 1.51 ± 0.007 | 1.43 ± 0.009 | 1.37 ± 0.009 |
| $\gamma_1$ (P) | 51,000 ± 3,600 | 44,800 ± 2,100 | 38,900 ± 2,500 | 24,400 ± 1,100 |
| $\alpha_1$ (P) | -68,900 ± 9,400 | -60,000 ± 7,400 | -52,900 ± 5,300 | -46,300 ± 5,000 |
| $\alpha_2$ (P) | -31,400 ± 3,500 | -28,000 ± 1,700 | -24,900 ± 1,800 | -14,600 ± 800 |
| $\eta_c$ (P) | 8,200 ± 360 | 7,400 ± 850 | 5,400 ± 600 | 1,700 ± 100 |
| * $\eta_b$ (P) | 3,500 ± 1,500 | 3,900 ± 1,800 | 5,300 ± 1,200 | 3,100 ± 1,100 |
| * $\alpha_3$ (P) | 19,600 ± 3,100 | 16,700 ± 2,700 | 14,100 ± 1,600 | 9,800 ± 1,400 |
| * $\gamma_2$ (P) | -11,700 ± 3,000 | -11,300 ± 3,200 | -10,700 ± 1,300 | -4,700 ± 870 |

**Table 5.3. Leslie-Ericksen viscoelasticity fit results for 22 wt % CTAB in $D_2O$.**

| Parameter | 22 wt %, 44 ºC | 22 wt %, 45 ºC |
|---|---|---|
| $k_{33}/k_{11}$ | 1.57 ± 0.006 | 1.52 ± 0.008 |
| $\gamma_1$ (P) | 37,400 ± 2,900 | 31,100 ± 5,700 |
| $\alpha_1$ (P) | -29,000 ± 6000 | -22,900 ± 4,200 |
| $\alpha_2$ (P) | -24,600 ± 2,500 | -20,100 ± 960 |
| $\eta_c$ (P) | 5,800 ± 200 | 5,600 ± 570 |
| * $\eta_b$ (P) | 5,900 ± 2,000 | 3,400 ± 1,200 |
| * $\alpha_3$ (P) | 12,800 ± 1,700 | 11,100 ± 1,300 |
| * $\gamma_2$ (P) | -11,800 ± 1,200 | -9000 ± 880 |

The fits in these tables were deliberately chosen to provide both a broad range of temperatures and to allow for comparison of behavior above and below the I-N transition. Examination of the tables reveals several general trends in the viscoelasticity fits. First, we note that values for the viscosities ($\alpha_i$, $\gamma_i$, and $\eta_i$) decrease with increasing temperature and constant concentration, as expected. We also find that at varying concentration and constant temperature (*i.e.* 18 and 20 wt % at 31 ºC), these viscosity values increase as expected. Additionally, the values of $\eta_b$ and $\alpha_3$ are generally lower than the absolute values of $\gamma_1$, $\alpha_1$, $\alpha_2$, and $\eta_c$, as predicted.[16] In both the 20 and 22 wt % samples, we observe a significant increase of the ratio $\eta_b/\eta_c$ (flow parallel vs perpendicular to the nematic director) when the temperature exceeds the I-N transition (*i.e.* between 33 and 35 ºC in 20 wt %). However, the 18 wt % sample fits do not exhibit this correlation. Values of $\eta_b/\eta_c$ are in the range for conventional nematics.[16] Our fit values are 1 – 2 orders of magnitude greater than those of Martins et al.,[16] but we note that their

measurements were for a thermotropic nematic polymer system, and these types of measurements have not yet been published for CTAB or other WLM system.

### 5.4.2 Self-Diffusion of CTAB and Solvent

We obtain measurements of $D$ independently in three orthogonal directions for the $D_2O$ solvent molecules by measuring the PFG $^2H$ NMR echo signal decay. Figure 5.4 shows $D_{D2O}$ as a function of temperature for several concentrations of the CTAB/$D_2O$ system. The diffusion anisotropy can be clearly seen as the parallel ($z$) values are significantly greater than the perpendicular ($x$ and $y$) values, indicating increased translational motion of solvent molecules along the alignment direction of the WLM system. Additionally, in the WLM solution, $D_{D2O}$ values are approximately forty percent slower than free water in the perpendicular direction, and thirty percent slower in the parallel direction (for reference, $D_{H2O}$ for free water at room temperature is 2.3 x $10^{-9}$ m/s$^2$). This indicates that the local viscosity of the $D_2O$ solvent molecules rotating and translating between the WLMs must be quite high relative to the bulk solution viscosity. Because the PFG NMR experiment measures the average $D$ for all molecules in the sample, and we observe only single component fits to our diffusion data, we conclude that there is little free water in the system (*i.e.*,

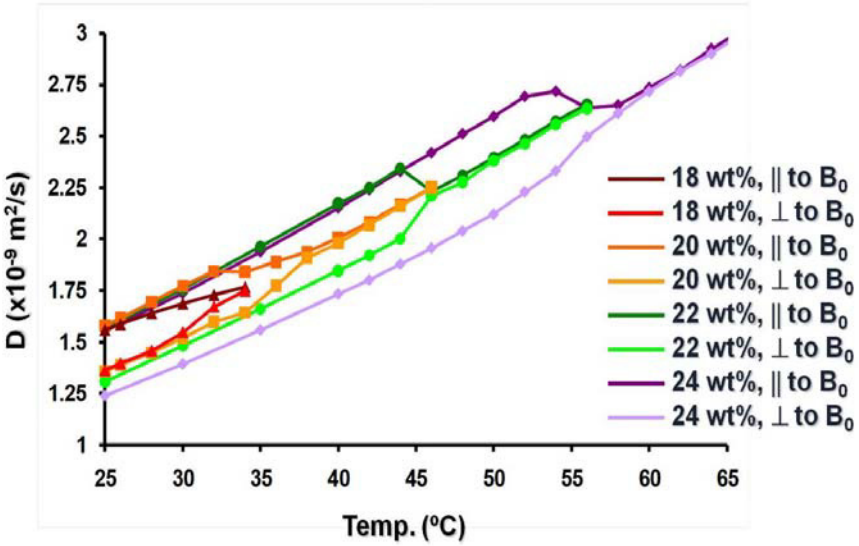


**Figure 5.4. $D_{D2O}$ measurements as a function of temperature** in two orthogonal directions for several concentrations of CTAB. Measurements parallel to $\mathbf{B_0}$ correspond to the director orientation of the aligned nematic.

there are no free water "channels" between the WLMs wherein the $D_2O$ solvent molecules can travel faster. This is consistent with our $^2H$ NMR alignment measurements, which also indicate that the $D_2O$ molecules must be constrained in order to "inherit" the order of the WLM matrix and exhibit a splitting in the $^2H$ spectrum. Further, the transition to the isotropic phase (disappearance of splitting in the $^2H$ alignment measurements) corresponds to the convergence of the parallel and perpendicular $D_{D2O}$ traces in fig. 5.4.

We also measure $D_{CTAB}$ for the CTAB molecules by observing the $^1H$ NMR PFG signal, which can be seen in fig. 5.5. Again, the PFG NMR experiment provides an average value of $D$ for all CTAB molecules in the sample, including both molecules which have assembled into WLMs and free molecules translating between individual WLMs. We note that WLM diffusion along the $\mathbf{B_0}$ field (alignment direction) is approximately twenty percent faster than in the transverse directions (perpendicular to the nematic director) when the system is in the aligned nematic phase. At low temperatures (below the I-N transition), we observe single component fits to the diffusion data. Based on calculations using the Stokes-Einstein equation, $D_{CTAB}$ for a single CTAB molecule in water is ~ 1.0 x $10^{-10}$ $m^2/s$, which indicates that these PFG experiments are measuring the diffusion of entire WLMs or WLM segments, and not individual CTAB molecules. We also

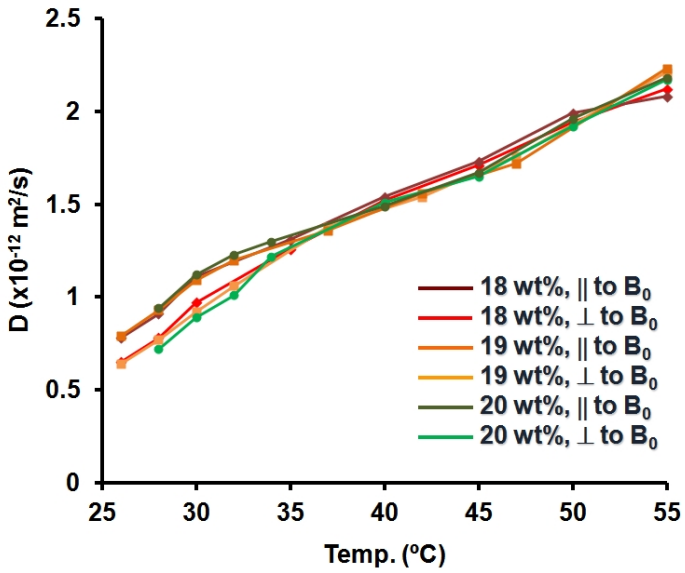


**Figure 5.5. $D_{CTAB}$ measurements as a function of temperature** in two orthogonal directions. Measurements parallel to $\mathbf{B_0}$ correspond to the director orientation of the aligned nematic.

observe a second $D_{CTAB}$ coefficient at higher temperatures (above the I-N transition) which could correspond to free molecules moving between worms or smaller WLM segments translating though the solution. This second diffusion coefficient is 1 - 2 orders of magnitude faster (*i.e.*, 1.2 x $10^{-10}$ $m^2/s$ for 18 wt % CTAB in D2O at 55 ºC), and is almost certainly present at lower temperatures, but occurs less frequently and is thus a smaller component of the diffusion measurement. Finally, we calculate the hydrodynamic radius $r_H$ for CTAB WLMs using the Stokes-Einstein equation and our measured $D_{CTAB}$ values, and determine an average WLM length of ~ 100 nm (though we note that WLM entanglement is likely contributing to the diffusion value, and thus the actual average length is almost certainly smaller).

Comparing fig. 5.4 and 5.5, we observe a stronger dependence of the coalescence temperature of the perpendicular and parallel diffusion rates on composition for the $D_2O$ solvent molecules. We are unsure why the coalescence temperatures appear to be closer in the $D_{CTAB}$ case, but WLM entanglements and faster breaking and recombination times with increasing temperature may play a role in this behavior. Additionally, we note that in both the $D_{CTAB}$ and $D_{D2O}$ case, there is a difference of approximately twenty percent in the parallel and perpendicular to $\mathbf{B_0}$ directions when the WLM director

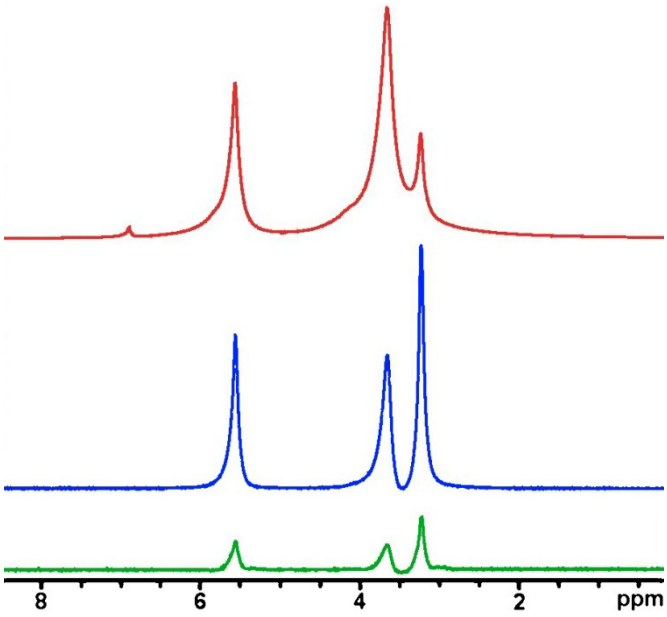


**Figure 5.6. $^1$H NMR spectra of 20 wt % CTAB in $D_2O$.** The red trace is a standard 1D spectrum, while the blue and green traces are the first and last slices of the PGSTE experiment, with gradient strength $g$ = 3 and 150 G/cm, respectively. Temperature is 45 ºC.

is aligned with $\mathbf{B_0}$. Further, these experiments were performed solely on CTAB solutions that were magnetically aligned in the NMR instrument, with no shear history. Application of shear to impart increased alignment, or observations on CTAB solutions which had previously been sheared in the manner described for fig. 5.3 would likely yield different $D_{CTAB}$ diffusion profiles. In fig. 5.6, we present representative $^1$H spectra of the CTAB/$D_2O$ system, including a standard 1D spectrum (red trace) and two spectra at different points during the PGSTE diffusion experiment. The small peak in the 1D spectrum at ~ 6.9 ppm corresponds to fast diffusing $H_2O$, and is weighted out at even the first step of the PGSTE experiment (blue trace, corresponding to $g$ = 3 G/cm). The broad linewidths in these experiments are intrinsic to these viscous samples, and are not due to shimming errors.

### 5.4.3 Solution Rheology and Disparity Between $H_2O$ and $D_2O$

Representative results of steady state solution rheology experiments measuring the shear stress of 20 wt% CTAB in $D_2O$ at varying temperatures are shown in fig. 5.7. In the isotropic region (40 and 45 ºC), we observe behavior consistent with nonlinear shear-thinning models characterized by a linear response at low shear rates, followed by a region of sub-linear shear thinning and an upturn at higher shear rates. Note that this upturn at high shear rates is predicted but not always observed due primarily to experimental limitations in applied shear rates and formation of foam or bubbles in surfactant

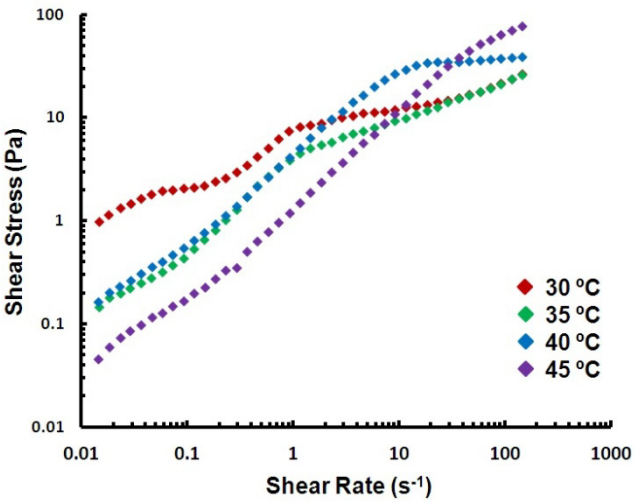


**Figure 5.7. Steady state shear stress measurements for 20 wt% CTAB in $D_2O$** for temperatures in the nematic and isotropic phases and near the I-N transition.

solutions. In the nematic phase (30 and 35 ºC), the system exhibits varying degrees of shear thinning behavior over nearly the entire range of shear rates, similar to the behavior of other micellar systems.[5]

Fig. 5.8 shows constant temperature results for various concentrations. We note that these observations are consistent with similar studies performed by Helgeson *et al*.[46] Comparing fig. 5.8 with fig. 5.2, we can correlate WLM behavior in both the solution rheology and rheo-NMR experiments. Looking specifically at the data for 18 wt % CTAB in $D_2O$, for example, we find that at low shear rates (< 3 $s^{-1}$), the linear slope of the shear stress measurements (red data in fig. 5.8) corresponds with the fast shear alignment region of fig. 5.2 (see inset, red data). This indicates that at low shear rates, there is a rapid response of the WLM system characterized by both micellar alignment and increasing shear stress. Here, we believe large segments of the nematic WLM system are rotating so that their directors align in the flow direction. In the next region of fig. 5.2 (encompassing shear rates 3 - 30 $s^{-1}$), a more gradual increase of alignment is observed. This region of fig. 5.8 exhibits a shear-thinning plateau, and may be indicative of WLM entanglements being broken up and slowly aligning with the laminar flow. Finally, at higher shear rates (30 - 130 $s^{-1}$), we observe a plateau in fig. 5.2 as the director of the system has reached maximum alignment along the shear direction. This region corresponds to

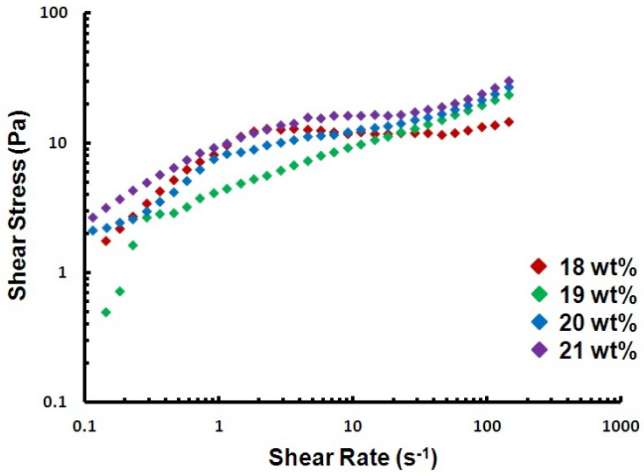


**Figure 5.8. Steady state shear stress measurements** at 30 ºC for 18 – 21 wt% CTAB in $D_2O$.

an upturn in the shear stress values in fig. 5.8. These general trends are also observed in other concentrations we have experimented with (18 - 22 wt % CTAB in $D_2O$).

We have also obtained steady state viscosity measurements as a function of applied shear rate for 0.76 M CTAB in both $D_2O$ and $H_2O$ (corresponding to 20 wt% in $D_2O$). Results of these experiments at 30 and 35 ºC are shown in fig. 5.9. These temperatures were chosen to be within the nematic phase and near the I-N transition, respectively. In the $D_2O$ samples, we observe a linear decrease in viscosity at low shear rates, followed by a small plateau before a return to linearly decreasing behavior. Samples in $H_2O$ showed nearly constant plateau behavior over the entire range of shear rates investigated. It is possible that this disparate behavior is attributable to differences in hydrogen bonding strength, but additional study is needed to clarify this behavior. While our CTAB-$D_2O$ findings are consistent with those of Helgeson *et al.*,[47] our CTAB-$H_2O$ data exhibit behavior different than that of Cappelaere et al.[39] However, concentrations used in the Cappelaere *et al.* study were significantly lower, and detailed rheological studies of the salt-free CTAB-$H_2O$ system at the higher concentrations shown here have not been published.

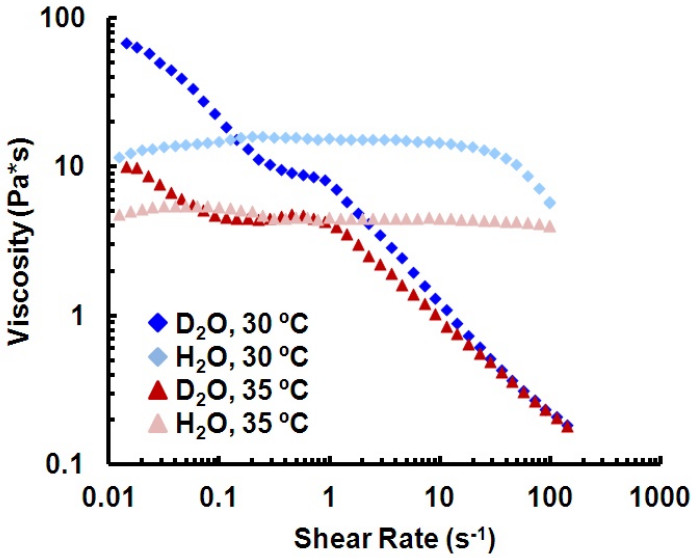


**Figure 5.9. Comparison of steady state shear viscosity measurements for 0.76 M CTAB in $D_2O$ and $H_2O$.**

## 5.5 Concluding Remarks

We quantitatively measure the phase behavior and dynamics of shear and magnetic field alignment in CTAB WLMs using $^2$H rheo-NMR of residually aligned $D_2O$ solvent probe molecules. Additionally, we use PFG NMR to measure the self-diffusion coefficient of both $D_2O$ and CTAB in the system with nuclear specificity, and correlate these diffusion measurements with our $^2$H magnetic alignment data. Further, we note a disparity between the rheological behavior of CTAB in $H_2O$ vs $D_2O$. Enhanced understanding of these materials could lead to improved micelle design and more precise control of alignment and viscoelastic behavior in applications.

**References**


(1) Dreiss, C. A. *Soft Matter* **2007**, *3*, 956-970.

(2) Tanaka, F. *Langmuir* **2010**, *26*, 5374-5381.

(3) Alam, T. M.; McIntyre, S. K. *Langmuir* **2008**, *24*, 13890-13896.

(4) Cates, M. E.; Candau, S. J. *J. Phys.: Condens. Matter* **1990**, *2*, 6869-6892.

(5) Lopez-Gonzalez, M. R.; Holmes, W. M.; Callaghan, P. T. *Soft Matter* **2006**, *2*, 855-869.

(6) Yang, J. *Curr. Opin. Colloid & Interface Sci.* **2002**, *7*, 276-281.

(7) Kim, Y.; Dalhaimer, P.; Christian, D. A.; Discher, D. E. *Nanotechnology* **2005**, *16*, S484-S491.

(8) McKee, M. G.; Layman, J. M.; Cashion, M. P.; Long, T. E. *Science* **2006**, *311*, 353-355.

(9) Rose, G. D.; Foster, K. L. *Journal of Non-Newtonian Fluid Mechanics* **1989**, *31*, 59-85.

(10) Vasudevan, M.; Buse, E.; Lu, D. L.; Krishna, H.; Kalyanaraman, R.; Shen, A. Q.; Khomami, B.; Sureshkumar, R. *Nature Mater.* **2010**, *9*, 436-441.

(11) Liu, S. Y.; Gonzalez, Y. I.; Danino, D.; Kaler, E. W. *Macromolecules* **2005**, *38*, 2482-2491.

(12) Nakamura, K.; Shikata, T. *Journal of Physical Chemistry B* **2006**, *110*, 24802-24805.

(13) Nakamura, K.; Shikata, T. *Langmuir* **2006**, *22*, 9853-9859.

(14) Walker, L. M.; Kuntz, D. M. *Curr. Opin. Colloid & Interface Sci.* **2007**, *12*, 101-105.

(15) Coppola, L.; Gianferri, R.; Nicotera, I.; Oliviero, C.; Ranieri, G. A. *Phys. Chem. Chem. Phys.* **2004**, *6*, 2364-2372.

(16) Martins, A. F.; Esnault, P.; Volino, F. *Phys. Rev. Lett.* **1986**, *57*, 1745-1748.

(17) Kilfoil, M. L.; Callaghan, P. T. *Macromolecules* **2000**, *33*, 6828-6833.

(18) Uludag, Y.; McCarthy, M. J.; Barrall, G. A.; Powell, R. L. *Macromolecules* **2001**, *34*, 5520-5524.

(19) Cormier, R. J.; Schmidt, C.; Callaghan, P. T. *Journal of Rheology* **2004**, *48*, 881-894.

(20) Hubbard, P. L.; McGrath, K. M.; Callaghan, P. T. *Langmuir* **2006**, *22*, 3999-4003.

(21) Lukaschek, M.; Grabowski, D. A.; Schmidt, C. *Langmuir* **1995**, *11*, 3590-3594.

(22) Douglass, B. S.; Colby, R. H.; Madsen, L. A.; Callaghan, P. T. *Macromolecules* **2008**, *41*, 804-814.

(23) Hollingsworth, K. G.; Johns, M. L. *Journal of Rheology* **2004**, *48*, 787-803.

(24) Cappelaere, E.; Berret, J. F.; Decruppe, J. P.; Cressely, R.; Lindner, P. *Phys. Rev. E* **1997**,

*56*, 1869-1878.

(25) Angelico, R.; Burgemeister, D.; Ceglie, A.; Olsson, U.; Palazzo, G.; Schmidt, C. *Journal of Physical Chemistry B* **2003**, *107*, 10325-10328.

(26) Fischer, E.; Callaghan, P. T. *Phys. Rev. E* **2001**, *6401*.

(27) Lu, C. Y. D.; Olmsted, P. D.; Ball, R. C. *Phys. Rev. Lett.* **2000**, *84*, 642-645.

(28) Clawson, J. S.; Holland, G. P.; Alam, T. M. *Phys. Chem. Chem. Phys.* **2006**, *8*, 2635-2641.

(29) Rapp, A.; Ermolaev, K.; Fung, B. M. *Journal of Physical Chemistry B* **1999**, *103*, 1705-1711.

(30) Wilmsmeyer, K. G.; Zhang, X.; Madsen, L. A. *Soft Matter* **2012**, *8*, 57-60.

(31) *NMR of Ordered Liquids*; Burnell, E. E.; de Lange, C. E., Eds.; Kluwer: Dordrecht, 2003.

(32) Deloche, B.; Samulski, E. T. *Macromolecules* **1981**, *14*, 575-581.

(33) Yu, L. J.; Saupe, A. *Journal of the American Chemical Society* **1980**, *102*, 4879-4883.

(34) Li, J.; Wilmsmeyer, K. G.; Madsen, L. A. *Macromolecules* **2009**, *42*, 255-262.

(35) Stejskal, E. O.; Tanner, J. E. *J. Chem. Phys.* **1965**, *42*, 288-292.

(36) Youssry, M.; Coppola, L.; Marques, E. F.; Nicotera, I. *Journal of Colloid and Interface Science* **2008**, *324*, 192-198.

(37) Shukla, A.; Fuchs, R.; Rehage, H. *Langmuir* **2006**, *22*, 3000-3006.

(38) Dokter, A. M.; Woutersen, S.; Bakker, H. J. *Journal of Chemical Physics* **2007**, *126*.

(39) Cappelaere, E.; Cressely, R.; Decruppe, J. P. *Colloids and Surfaces a-Physicochemical and Engineering Aspects* **1995**, *104*, 353-374.

(40) Cates, M. E. *Macromolecules* **1987**, *20*, 2289-2296.

(41) Kato, T.; Terao, T.; Seimiya, T. *Langmuir* **1994**, *10*, 4468-4474.

(42) Kato, T.; Terao, T.; Tsukada, M.; Seimiya, T. *Journal of Physical Chemistry* **1993**, *97*, 3910-3917.

(43) Veron, A.; Gomes, A. E.; Leal, C. R.; Van der Klink, J.; Martins, A. F. *Molecular Crystals and Liquid Crystals Science and Technology Section a-Molecular Crystals and Liquid Crystals* **1999**, *331*, 2359-2367.

(44) Magda, J. J.; Baek, S. G.; Devries, K. L.; Larson, R. G. *Macromolecules* **1991**, *24*, 4460-4468.

(45) Veron, A.; Gomes, A. E.; van der Klink, J.; Martins, A. F. *Ampere 2000 Proceedings*;

CD-ROM book: Lisbon, 2001.

(46) Helgeson, M. E.; Reichert, M. D.; Hu, Y. T.; Wagner, N. J. *Soft Matter* **2009**, *5*, 3858-3869.

(47) Helgeson, M. E.; Vasquez, P. A.; Kaler, E. W.; Wagner, N. J. *Journal of Rheology* **2009**, *53*, 727-756.

(48) Cheng, C. Y.; Hwang, L. P. *Journal of the Chinese Chemical Society* **2001**, *48*, 953-962.

(49) Lukaschek, M.; Kothe, G.; Schmidt, C.; Gomes, A. E.; Polimeno, A. *J. Chem. Phys.* **2002**, *117*, 4550-4556.

(50) Stefanov, M.; Saupe, A. *Mol. Cryst. Liq. Cryst.* **1984**, *108*, 309-316.

(51) Vijayaraghavan, D.; Suresh, K. A. *Mol. Cryst. Liq. Cryst.* **2005**, *434*, 609-618.

(52) Frank, F. C. *Discussions Faraday Soc.* **1958**, *25*, 19-28.

(53) Parodi, O. *J. Phys.-Paris* **1970**, *31*, 581-584.

(54) Ericksen, J. L. *Trans. Soc. Rheol.* **1961**, *5*, 23-34.

(55) Leslie, F. M. *Arch. Rat. Mech. Anal.* **1968**, *28*, 265-283.

(56) Miesowicz, M. *Nature* **1935**, *136*, 261.

# Chapter 6

# Concluding Remarks

## 6.1 General Comments

I have shown that the combination of the fields of rheology and nuclear magnetic resonance spectroscopy to form rheo-NMR is extremely valuable and promising in terms of both the current abilities it has, as well as the potential for future development and discovery. This exciting and relatively new technique has found substantial use in many areas, including polymer melts, liquid crystals, wormlike micelles, and even food chemistry. Rheo-NMR has found wide use in the examination of microscopic polymer properties and velocimetry, as well as correlating those properties to their macroscopic counterparts. As more groups begin to delve into the realm of rheo-NMR, numerous additional uses and techniques can be expected to emerge in the years to come. Because the field is still virtually in its infancy, the true scope and magnitude of rheo-NMR has yet to be seen.

## 6.2 Perfluorosulfonate Ionomers

Initial work with Nafion membranes in our lab showed the first comparisons of diffusion and transport with quantitative orientational order measurements in ionomer materials. Additionally, we compared dispersion-cast membranes with uniaxially aligned ionic channels perpendicular to the membrane plane against extruded membranes with biaxially aligned channels oriented in the membrane plane. Our measurements also allow us to calculate the biaxiality parameter of these hydrophilic channels in a straightforward manner, contrary to more cumbersome methods such as XRD or polarizing microscopy. Diffusion measurements reveal anisotropic transport which correlates with orientational order of the ionic channels.

## 6.3 CTAB Wormlike Micelles

My work with CTAB WLMs investigated phase behavior and dynamics of shear and field alignment as a function of composition, temperature, and aligning field strength. We also revealed the first observations of a bistable, shear-induced phase wherein micelles will not align with the magnetic field until after they have been aligned in a shear field. Additionally, we made the first reports of calculated anisotropic viscoelastic parameters for a WLM system by monitoring the dynamics of realignment and fitting the data to Leslie-Ericksen viscoelasticity theory. Solution rheology studies further expanded on this work, and showed a disparity in rheological behavior of the CTAB system between $H_2O$ and $D_2O$ solvents at a given concentration. Finally, use of PFG NMR techniques allows for measurement of the self-diffusion coefficients of both the $D_2O$ solvent and the CTAB WLMs with nuclear specificity, showing that the WLMs diffuse three orders of magnitude slower than the solvent molecules. These data correlate well with our $^2H$ magnetic alignment data for this system.

## 6.4 Future Research Directions

We remain confident that control of the direction and extent of order present in the hydrophilic channels of ionomer membranes such as Nafion will allow increased material design freedom and enhanced device performance. Methods of processing (*e.g.* stretching or solvent casting membranes under applied magnetic or electric fields) could potentially improve these materials. This work has been continued and expanded in our lab, branching out to additional membrane chemistries and morphologies, as well as investigations of ionic liquids as the diluents in these materials.

Additional lines of investigation of CTAB WLMs include further study of the link between solution rheology and rheo-NMR behavior. Deeper understanding of the fundamental

behaviors of these systems can promote further design of micellar materials and allow tailoring of viscoelastic and alignment behavior for applications in tissue engineering, drug delivery, oil extraction, coatings, and lubricants. Also, the potential for use of WLMs as variable alignment media in NMR structure determination has begun with inclusion of small molecules which reside in the core of or between micelles (depending on hydrophilic or hydrophobic functionality).